Understanding and Controlling the Growth of Metals and Molecules on an Insulating Surface

Jeffrey M. Mativetsky
Department of Physics
McGill University
Montreal, Quebec, Canada
June 2006

A thesis submitted to McGill University in partial fulfilment of the requirements of the degree of Doctor of Philosophy

Your file Votre référence
ISBN: 978-0-494-27819-2
Our file Notre référence
ISBN: 978-0-494-27819-2

Table of Contents

Abstract

Noncontact atomic force microscopy (NC-AFM) was applied to investigating the creation of monatomic depth rectangular pits, the growth of metals, and the templated growth of molecules on the KBr (001) surface under ultrahigh vacuum conditions. The pits were produced by a new method where the sample is exposed to a controlled dose of charge from an electron beam evaporator. The structure and size distribution of the pits was characterized by NC-AFM. For the metal growth studies, gold, tantalum, and palladium were deposited onto KBr by electron beam deposition. The gold produced tall multiply twinned and epitaxial nanoparticles, while the tantalum formed flatter fractal islands. The palladium growth resulted in the creation of rectangular KBr islands in addition to palladium nanoparticles. Despite the use of a charge deviating grid, charge played an important role during the metal growth. In particular, the number density of gold nanoparticles followed nearly the same temperature dependence as the pits, suggesting that the metal nanoparticles nucleate predominantly at defect sites created by incident charge. The effect of charge was also seen in the tantalum system where pits surrounded the nanoparticles prepared at elevated temperatures. By creating pits before depositing gold, it was shown that the pits edges can be used to template the growth of metals. It was also shown that the pits can be used to trap PTCDA molecules and to align C_{60} molecules with the <100> direction of the substrate. Molecular resolution NC-AFM measurements were used to determine the structures and lattice constants of the molecular nanostructures. Experiments involving the sequential growth of metals and molecules showed that the order of deposition and the strength of the molecule-metal interaction are key factors in determining the nature of the growth. Furthermore, it was shown that metal structures can be used to nucleate the growth of sufficiently strongly interacting molecules.

Résumé

La microscopie à force atomique non contact (NC-AFM) a été utilisée pour étudier la formation de cavités de profondeur monoatomique, la croissance de métaux, et la croissance guidée de molécules sur la surface du KBr (001), sous des conditions de vide ultra poussé. En mettant au point une nouvelle méthode, des cavités ont été créées sur l'échantillon en imposant une dose contrôlée de charge provenant d'un évaporateur à faisceau d'électrons. La structure et la distribution de tailles des cavités ont été caractérisées par NC-AFM. Afin d'étudier la croissance des métaux, l'or, le tantale, et le palladium ont été déposés sur le KBr par évaporation à faisceau d'électrons. L'or a produit de hautes nanoparticules maclées et épitaxiales, tandis que le tantale a formé des îles fractales et relativement plates. La croissance de palladium a produit des îles rectangulaires de KBr en plus des nanoparticules de palladium. Malgré l'usage d'une grille à déviation de charge, la charge a joué un rôle important pendant la croissance des métaux. En particulier, le nombre de nanoparticules d'or à la surface a suivi presque la même dépendance en température que les cavités, suggérant une nucléation des nanoparticules principalement aux l'endroits où se trouvent les défauts induits par la charge provenant de l'évaporateur. On a observé aussi l'influence de la charge dans le cas du tantale, où des cavités renferment les nanoparticules préparées à température élevée. En créant les cavités avant la déposition de l'or, il est démontré que les bords des cavités peuvent être utilisés pour orienter la croissance du métal. Il a aussi été établi que les cavités peuvent être utilisées pour piéger des molécules PTCDA et pour aligner des molécules de C_{60} dans la direction <100> du substrat. Des mesures à résolution moléculaire ont été utilisées pour déterminer les structures et les constantes du réseau cristallin des nanostructures moléculaires. Des expériences de croissance séquentielle du métal et de molécules ont démontré que l'ordre de la déposition et la force de l'interaction entre les molécules et les métaux sont des facteurs clés dans la détermination de la nature de la croissance. De plus, il a été

démontré que des structures en métal peuvent être utilisées pour nucléér la croissance des molécules présentant des interactions assez fortes.

Acknowledgements

Firstly, I am grateful to my supervisor, Peter Grutter, for giving me the opportunity to work on this exciting project and for giving me the freedom to explore. I thank my lab mates Sarah Burke and Shawn Fostner for many helpful discussions and for making the lab an enjoyable place to work. I am also indebted to Yoichi Miyahara, Regina Hoffmann, and Roland Bennewitz for being valuable resources.

I am thankful to Robert Gagnon and Leo Nikkinen for their assistance with the setup of the new lab, Sabine Maier and Roland Bennewitz for helping with the noise spectra measurements, and Dr. H. Vali for his TEM work. I would also like to thank Patricia Davidson and Shawn Fostner for proof reading the thesis, and thank Helene Bourque and Mehdi El Ouali for proof reading the Résumé.

For financial support, I would like to acknowledge NSERC, FQRNT, Walter C. Sumner, Carl Reinhardt, the Physics Department, and my supervisor Peter Grutter.

Statement of Originality

The author claims the following aspects of the thesis to be original contributions of knowledge:

- The commissioning and testing of the JEOL JSPM 4500A ultrahigh vacuum system, including a characterization of the resolution, noise, and drift during noncontact atomic force microscopy (NC-AFM) measurement.

  J. M. Mativetsky, S. A. Burke, R. Hoffmann, Y. Sun, P. Grutter, Nanotechnology **15**, S40 (2004).

- The demonstration of a new method for creating monatomic-depth rectangular pits of controlled size in an alkali halide surface by using an electron beam evaporator as a source of charge. The measurement of the pit size distributions. Atomic resolution NC-AFM imaging of the pits prepared at different temperatures.

  J. M. Mativetsky, Y. Miyahara, S. Fostner, S. A. Burke, P. Grutter, Applied Physics Letters **88**, 233121 (2006).

- The NC-AFM characterization of the growth of gold, tantalum, and palladium on KBr. The influence of defect creation during growth was examined and shown to play an important role.

- The use of pits to template the growth of gold, PTCDA molecules, and C_{60} molecules. High resolution NC-AFM showed the molecular arrangement of the resulting PTCDA and C_{60} crystallites. The specificity of the

PTCDA-substrate interaction was used to identify the ionic species of the imaged substrate lattice. In addition, signatures of molecular diffusion were used to estimate the diffusion energy of PTCDA on a PTCDA island. It was determined that the observed height differences between some C_{60} molecules are of geometric origin and most likely caused by a phase transition.

J. M. Mativetsky, S. A. Burke, S. Fostner, P. Grutter, submitted.

- The sequential growth of molecules and metals on KBr showed that the order of deposition and the strength of the molecule-metal interaction are key factors in determining the resultant structures.

1 Introduction

Insulating materials are ubiquitous in the world around us. In fact, most of the objects that we encounter are non-conducting. In terms of properties, the surfaces are especially important since this is where the materials interface and interact with their surroundings. Nevertheless, despite the prevalence of insulating surfaces in electronics, catalysis, materials science, and even biology, this domain of research remains largely unexplored. The lack of data is primarily due to a shortage of tools. The problem is that most surface science techniques involve either electron or ion bombardment [1]. On insulators, this leads to difficulties related to trapped charge and surface damage. Furthermore, scanning tunnelling microscopy (STM), which has been tremendously successful in elucidating the atomistic processes which occur on conducting and semiconducting surfaces, cannot be applied to insulators.

Conventional atomic force microscopy (AFM) has been developed and applied over the last 20 years with some success [2]. However, the so-called contact and tapping modes are typically limited to resolutions of a few nanometers, an order of magnitude too low to observe atomic scale processes. Noncontact atomic force microscopy (NC-AFM) was first applied in 1991 to the study of magnetic interactions at surfaces [3]. The technique was later adapted and improved, and in 1995 provided atomic resolution measurements of the silicon (111) surface [4, 5]. Since then, NC-AFM has been applied to insulating [6, 7], conducting [8, 9], and more recently, molecular systems [10, 11]. Because of the high resolution capability of NC-AFM, it is expected that the technique will broadly expand our understanding of insulating surfaces, much as STM has for metals and semiconductors.

To date, most NC-AFM studies have focused on the instrumentation, resolution capabilities, and imaging mechanisms of the technique [12]. In the present work, NC-AFM is applied to the investigation of the growth of metals and molecules on potassium bromide (KBr), an insulating salt. In addition, the creation of surface defects, and the influence of the defects on growth are examined. In order to have well-defined, clean surfaces, the experiments are performed under ultrahigh vacuum (UHV) conditions. Because the above topics represent relatively uncharted areas of surface science, some interesting and unanticipated behaviour was observed. Moreover, it will be shown that with an improved understanding of the processes involved in growth, it is possible to exercise an increased level of control, and ultimately create surface structures by design.

A large part of the motivation for this work is the ongoing effort in our lab to investigate the electrical properties of single molecules. The prospect of using single molecules as components in electronic circuits was proposed more than 30 years ago when Aviram and Ratner performed calculations predicting diode-like behaviour in certain classes of molecules [13]. By choosing appropriate structures, it is expected that a wide range of electrical properties can be engineered into individual molecules [14, 15]. Nevertheless, as interfacing with single molecules remains a great experimental challenge, the field of molecular electronics is still in its very early stages. To date, a handful of electrical measurements have been performed on single molecules [16-18], but only under conditions where it has not been possible to determine the detailed structure of the system. According to theoretical studies, the atomic structure of the electrodes near the molecule and the nature of the chemical bond between the molecule and electrodes play dominant roles in determining the conductivity [19, 20]. Our group is aiming towards investigating the relationship between structure and function by constructing a planar device on an atomically flat insulating surface in UHV. In this configuration, it should be possible to characterize the structure of the device by using NC-AFM.

An outline of the thesis is as follows: Chapter 2 presents a description of the instruments and the methodologies used, in addition to a characterization of the recently commissioned NC-AFM system. In Chapter 3, a new method for creating rectangular monatomic depth pits in a KBr surface is introduced. This is followed by a comparative study, presented in Chapter 4, of the growth of three metals on KBr: gold, tantalum, and palladium. The role of defect creation during growth will also be addressed. In Chapter 5, the defects and metal nanostructures are used to modify and template the growth of two types of molecules. Finally, a conclusion and outlook will be presented in Chapter 6. Throughout the thesis, the relevance of certain results to molecular device fabrication will be pointed out.

2 Instrumentation and Experimental Methods

With the exception of a few transmission electron microscope (TEM) measurements, all of the experiments, including the sample preparation and characterization, were performed under ultrahigh vacuum (UHV) conditions in a JEOL JSPM 4500A UHV AFM/STM/SEM system. The system consists of a unique combination of surface science tools and is the main element of the recently commissioned *Atomic Manipulation Facility*, part of the *NanoTools Facilities* at McGill. The author played a principal role in installing and testing all of the components. Only those instruments and methods which are relevant to the measurements presented in later chapters will be described in detail.

2.1 Ultrahigh Vacuum System

UHV is used to ensure that the sample surfaces remain clean throughout the experiments. A schematic of the UHV system is shown in Figure 2.1. It consists of two main chambers: a sample preparation chamber and a sample characterization chamber. Each chamber is pumped by an ion pump and a titanium sublimation pump. The base pressure is measured with an ion gauge, and is typically 1 - 4 x 10^{-8} Pa. A fast loadlock chamber, pumped by a turbomolecular pump, is used for introducing the samples and scanning probe tips into the system. The entire system is mounted on an air table for vibration isolation.

The preparation chamber has two evaporators, a quartz crystal monitor for measuring deposition rates, and a cleaving station for preparing cleaved samples *in situ*. These components will be described further in Section 2.3. The author designed a custom built UHV port in order to accommodate the two evaporators (see Appendix A). The preparation chamber is also equipped with a low energy electron diffractometer for measuring surface structure, an Auger spectrometer for measuring surface composition,

and an ion gun for sputtering surfaces. These latter three instruments were not used in the present study and are not commonly used with insulating substrates because of problems with surface charging.

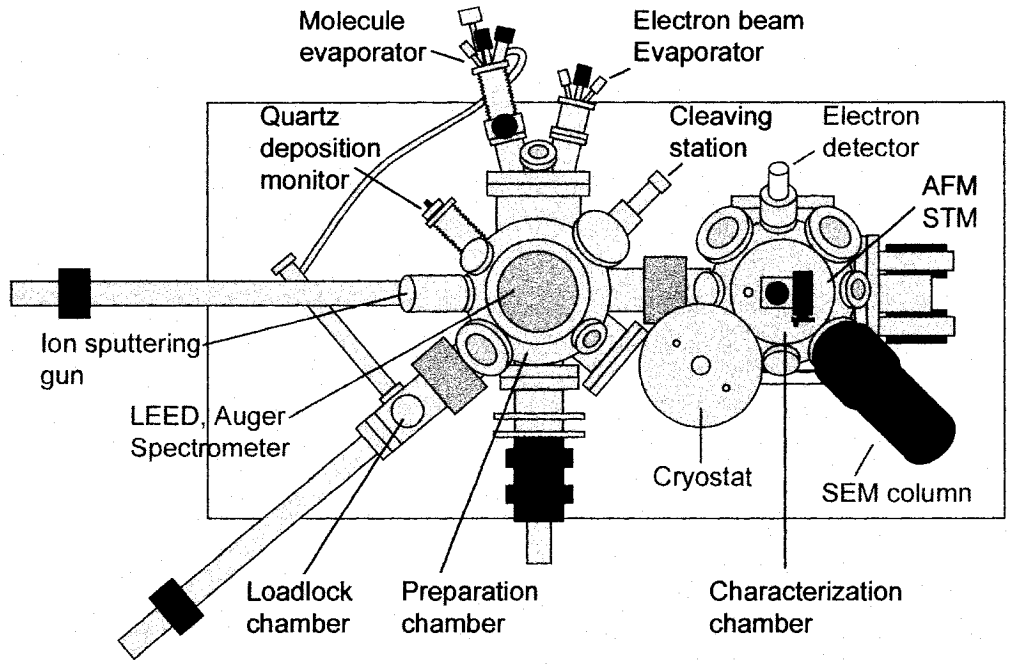

Figure 2.1: Schematic diagram showing a top view of the UHV system. The components labelled in grey were not used in the present study.

The atomic force microscope (AFM) and scanning tunnelling microscope (STM) stage is housed in the main chamber. The chamber also includes a field emission scanning electron microscope (SEM) which is useful for characterizing scanning probe tips, conducting samples, and for positioning the scanning probe tip above specific areas of a sample. The SEM resolution was determined to be better than 10 nm by measuring the minimum observable gap between gold beads on a graphite surface.[1] The main chamber also has a cryostat which contacts the sample position and can cool the sample down to temperatures as low as 30 K.

[1] The SEM resolution testing was performed with T. Laudate and C. Spencer.

2.2 Noncontact Atomic Force Microscope

Noncontact atomic force microscopy (NC-AFM) is a mode of atomic force microscopy (AFM) which has been developed over the last 15 years [12]. NC-AFM is unique in its ability to non-destructively measure surface structure with atomic resolution on all types of surfaces, including insulators [6, 7], semiconductors [4, 5], and metals [8, 9].

2.2.1 Principle of Operation

In AFM, a sharp tip located at the end of a cantilever is scanned over a surface. The forces acting between the tip and sample cause the cantilever to deflect. In dynamic modes, the cantilever is oscillated and the measured response is a change in oscillation amplitude or frequency. A feedback circuit is typically used to adjust the tip-sample distance such that a constant force (contact mode), oscillation amplitude (tapping mode), or oscillation frequency (noncontact mode) is maintained. A topographic image is reconstructed from the height adjustments of the scanner.

The noncontact mode is a dynamic AFM mode where the cantilever oscillates, usually with a fixed amplitude, and the oscillation frequency is used to regulate the tip-sample separation [3]. A block diagram of the experimental setup used for NC-AFM imaging is shown in Figure 2.2. A piezoactuator is used to oscillate the cantilever at its natural resonance frequency. When the tip is in close proximity to the sample, the tip-sample interactions cause a shift in the frequency. The cantilever's movement is measured by reflecting a laser beam off the back side of the cantilever, onto a position sensitive photodetector. The oscillation frequency is measured by a Nanosurf digital phase locked loop (PLL) and sent to a feedback circuit which maintains the frequency at a user-defined setpoint, by adjusting the tip height. During measurement, the cantilever oscillation amplitude is maintained at a constant value by a Nanosurf controller. Cantilevers (Nanosensors) with a typical resonance frequency of 170 kHz and a spring constant of 40-50 N/m were used with an oscillation amplitude of 5 nm. Prior to use, all cantilevers

are baked to about 150 °C in the preparation chamber for 7 hours, in order to remove surface contamination. The NC-AFM measurements were all performed at room temperature.

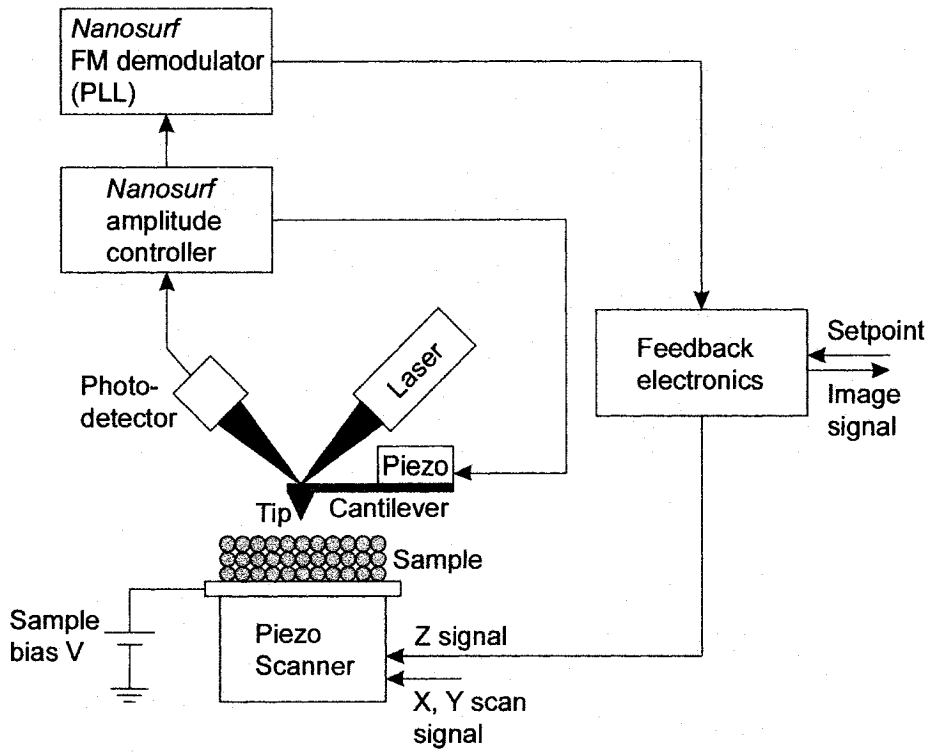

Figure 2.2: Block diagram of the experimental setup used for NC-AFM imaging.

2.2.2 Tip-Sample Forces

Treating the cantilever as a damped harmonic oscillator, the shift in frequency Δf can be expressed in terms of the force F as [2]

$$\Delta f = \frac{f_0}{\pi k A} \int_0^{2\pi/\omega} F(\bar{z} + A\sin\omega t)\sin\omega t dt\,, \qquad (2.1)$$

where f_0 is the unperturbed frequency of the cantilever, A is the oscillation amplitude, k is the spring constant of the cantilever, $\bar{z}$ is the time-average position of the tip, and $\omega = 2\pi f_0$. There are three main contributions to the total tip-sample force: electrostatic forces, van der Waals forces, and chemical forces: [2]

$$F = F_{ES} + F_{vdW} + F_{chem}. \tag{2.2}$$

The electrostatic and van der Waals forces are long range interactions, while the chemical forces act over a short range, and are largely responsible for the high resolution contrast seen in NC-AFM.

Assuming a spherical tip apex of radius R, the electrostatic forces between the tip and sample can be expressed as [21]

$$F_{ES} = -\frac{\pi\varepsilon_0 R(V_S - V_{CPD})^2}{z}, \tag{2.3}$$

where ε_0 is the permittivity of free space, z is the tip-sample separation at closest approach, and V_S is the bias voltage applied between tip and sample.[3] The quantity

$$V_{CPD} = \frac{\phi_{tip} - \phi_{sample}}{e} \tag{2.4}$$

is the contact potential difference (CPD) between the tip and sample, where ϕ_{tip} and ϕ_{sample} are the tip and sample work functions, and e is the charge of an electron. In terms

[2] Although they will not be considered here, dissipative, magnetic, and other forces can also contribute.
[3] In the case of insulating surfaces, the voltage is applied between the tip and the sample holder. This results in a polarization of the sample, and a similar dependence of force on applied voltage.

of frequency shift, assuming an oscillation amplitude $A >> z$,[4] the electrostatic contribution can be written as [21]

$$\Delta f_{ES} = -\frac{\pi\varepsilon_0 f_0 R(V_S - V_{CPD})^2}{kA\sqrt{2zA}}. \tag{2.5}$$

The CPD between the tip and sample can be determined by measuring the frequency shift as a function of applied voltage and determining the maximum value of Δf from the parabolic dependence. During NC-AFM imaging the electrostatic forces are typically minimized by applying a sample voltage equal to the CPD. This is especially true for high resolution imaging where it is desirable to have a relatively large contribution from short range forces.

The Van der Waals forces are weak long range attractive forces which are caused by dipole-dipole interactions. These may either be interactions between permanent dipoles, between dipoles and induced dipoles, or between temporary dipoles arising from fluctuations in the electronic distributions [22]. For a spherical tip apex, the van der Waals forces are [21]

$$F_{vdW} = -\frac{HR}{6z^2}, \tag{2.6}$$

where H is a material and geometry dependent constant known as the Hamaker constant. In terms of frequency shift, for $A >> z$, the van der Waals contribution is

$$\Delta f_{vdW} = -\frac{f_0 HR}{6zkA\sqrt{2zA}}. \tag{2.7}$$

[4] This approximation holds for typical imaging conditions.

The short range chemical interactions are more difficult to treat. One convenient empirical model is the Morse potential, which leads to a force [21]

$$F_{chem} = \frac{2U_0}{\lambda}\left[\exp\left(-2\frac{z-z_0}{\lambda}\right) - 2\exp\left(-\frac{z-z_0}{\lambda}\right)\right], \tag{2.8}$$

where U_0 is the bonding energy, λ is the interaction length and z_0 is the position of the interaction minimum. Since NC-AFM measurements are generally performed only in the attractive force regime, the chemical interaction can be approximated by the attractive term, yielding [21]

$$\Delta f_{chem} = -\frac{f_0 U_0}{kA}\sqrt{\frac{2}{\pi A\lambda}}\exp\left(-\frac{z-z_0}{\lambda}\right) \tag{2.9}$$

for $A >> z$.

A schematic of the dependence of the force and frequency shift on tip-sample separation is shown in Figure 2.3. At large distances, the cantilever experiences weak electrostatic and van der Waals attraction to the sample. As the cantilever is brought closer to the sample, the attractive forces increase until the electron clouds of the tip and sample atoms start to overlap and repulsive forces set in. Because the distance dependence of the frequency shift is non-monotonic, the feedback cannot operate over the full range of forces. Typically, the measurements are restricted to the attractive force regime, thus avoiding the steeply varying repulsive forces which are more likely to cause damage to the tip and sample. The non-destructive nature of this mode of imaging is what gave rise to the use of the term *noncontact* [12].

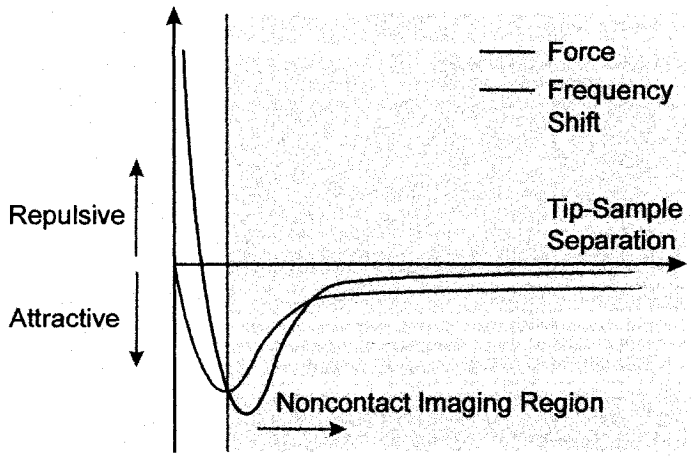

Figure 2.3: Schematic of the dependence of force and frequency shift on the tip-sample separation. In NC-AFM imaging, the measurements are restricted to the attractive force regime.

2.2.3 Resolution Testing

During the commissioning of the instrument, the resolution was tested by measuring the silicon (111) 7x7 surface reconstruction with atomic resolution[5], and C_{60} molecules on a gold (111) surface with molecular resolution (Figure 2.4). The silicon 7x7 reconstruction is a standard sample for resolution testing. It was first measured with atomic resolution by scanning tunnelling microscopy (STM) in 1982 [23], and later, in 1995, by NC-AFM [4, 5]. The sample was prepared by heating a (111) oriented silicon crystal up to about 1250 °C several times, for a few seconds each time. The heating was accomplished by running a current through the sample. This set of measurements was performed with the JEOL PLL rather than the later purchased Nanosurf PLL. The performance of the two units will be compared in Section 2.2.4. The C_{60} on gold (111) sample was prepared by depositing gold (100 nm) onto mica in a separate vacuum system,[6] and then depositing 2-3 ML of C_{60} in UHV. Further information about the C_{60} on gold (111) measurements can

[5] The room temperature Si (111) 7x7 measurements were performed with S. Kitamura, F. Mauric, and R. Hoffmann. The sample was also measured at 30 K with T. Sato and R. Hoffmann.
[6] The gold sample was prepared with Y. Sun.

be found in Ref. [24]. Similar testing on silicon and C_{60} on gold samples was performed with the scanning tunnelling microscope.

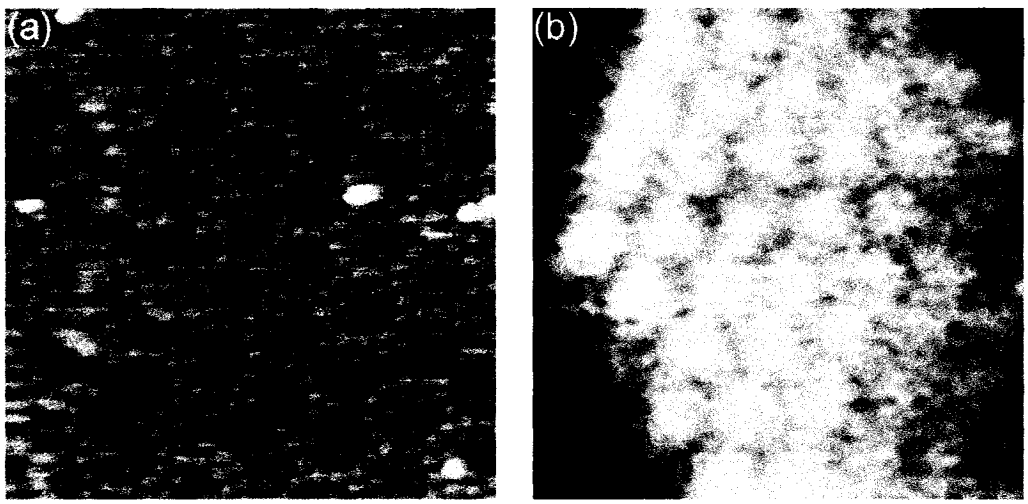

Figure 2.4: NC-AFM images of two samples used for resolution testing: (a) a silicon (111) 7x7 reconstructed surface (20 nm x 20 nm, Δf = -230 Hz), and (b) C_{60} molecules on a gold (111) surface (6 nm x 6 nm, Δf = -37 Hz).

2.2.4 Noise and Sensitivity

Figure 2.5 shows the noise spectrum of the photodetector signal while the cantilever is being driven at an amplitude of 5 nm.[7] Clearly, the cantilever resonance signal, at 175840.39 ± 0.06 Hz, is substantially larger than the background noise. As expected, the background noise level increases at low frequencies because of $1/f$ noise [12]. Furthermore, there is a reduction in noise at frequencies above about 500000 Hz. This frequency corresponds to the cutoff frequency of the photodetector's preamplifier. During NC-AFM measurement, the most important frequency range is in a small span near the cantilever resonance frequency. For the Nanosurf PLL used in the experiments, the measurement bandwidth is 1200 Hz. Figure 2.5 (b) shows a thermal noise spectrum, while Figure 2.5 (c) shows the noise for the excited cantilever system near the resonance frequency. The cantilever's quality factor [8] (Q-factor) was determined to be 6500 from the thermal resonance peak. However, when the cantilever is excited, the resonance peak is narrowed and the apparent Q-factor increases to 570000. This effective increase occurs because the cantilever is driven by means of self excitation. The positive feedback increases the relative weight of the most prominent frequencies and leads to an increased sharpness of the peak [25]. The high Q-factor plays an important role in the frequency resolution during NC-AFM measurement since the sharpness of the resonance peak affects the precision with which the center frequency can be determined.

[7] The noise spectra were measured with S. Maier and R. Bennewitz using Labview.
[8] The quality factor is defined as the resonance frequency divided by the full width half maximum of the resonance curve.

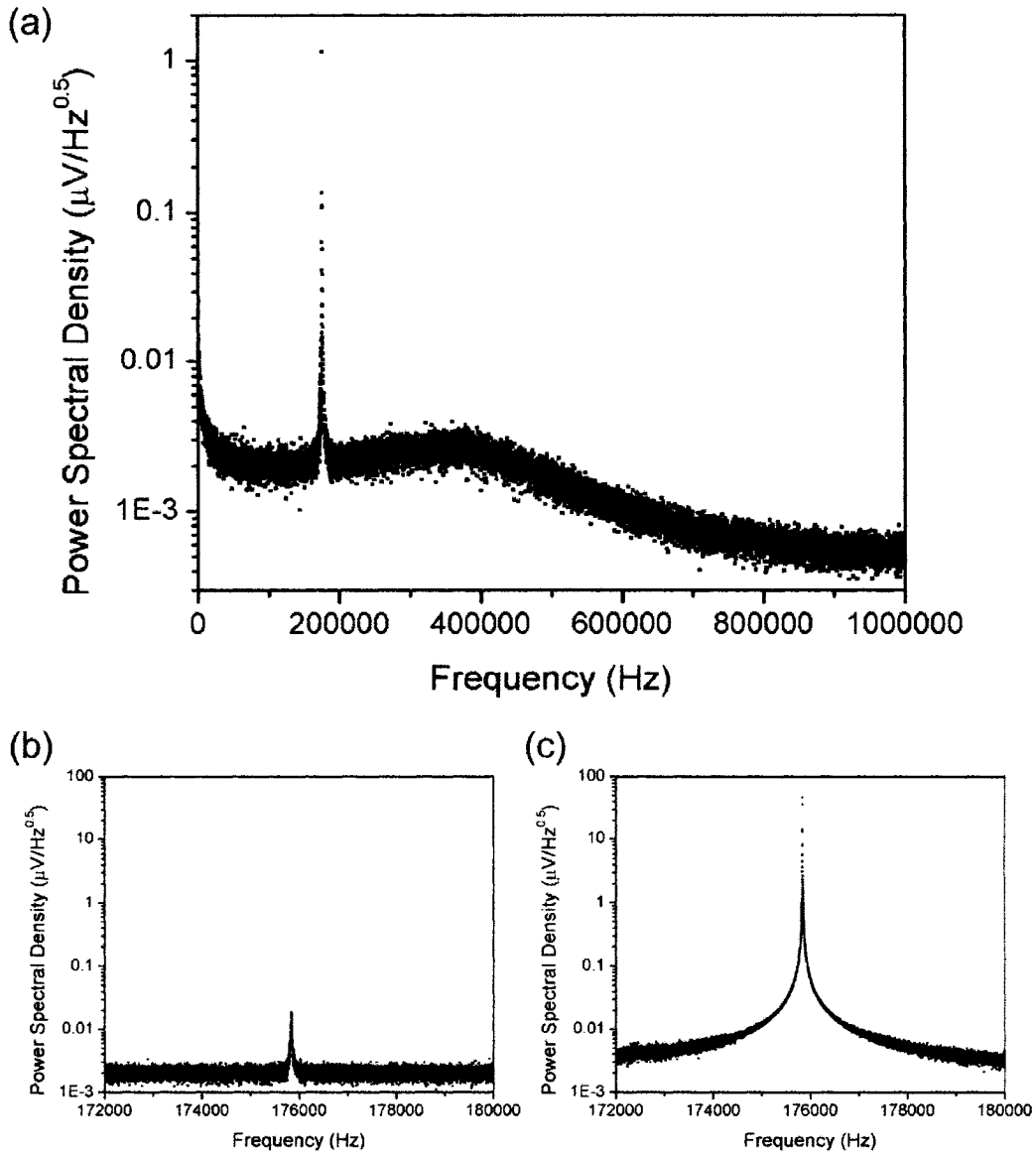

Figure 2.5: The noise spectrum of the photodetector signal: (a) for an excited cantilever, measured up to 1 MHz; (b) for a thermally vibrating cantilever near the resonance frequency, (c) for a self excited cantilever near the resonance frequency.

To characterize the frequency resolution of the instrument, the root mean squared (RMS) noise in the measured frequency was measured as a function of cantilever amplitude. Figure 2.6 shows a comparison between the JEOL and the Nanosurf frequency demodulators. Clearly, the Nanosurf PLL has a significantly better frequency resolution,

by about a factor of 10. The Nanosurf PLL also has an optional 300 Hz low pass filter on the output signal which improves the frequency resolution by nearly an additional factor of 10. All three curves have a slope of approximately -1, signifying that the noise is inversely related to the cantilever oscillation amplitude[9]. Typically, the detection electronics is the largest contributor to noise; however, in a few cases, there have been reports of systems which are thermally limited [26]. Both noise contributions have an inverse relationship with amplitude. The noise induced by thermal fluctuations in the cantilever oscillations is [12]

$$\delta f = \frac{1}{A}\sqrt{\frac{2k_B TBf_0}{\pi^3 kQ}}, \tag{2.10}$$

where A is the oscillation amplitude, k is the spring constant, Q is the Q-factor, f_0 is the resonance frequency, B is the bandwidth of the measurement, k_B is the Boltzmann constant, and T is the temperature. The noise associated with the detection electronics is [27]

$$\delta f = \frac{n_{in}}{A}\sqrt{\frac{\pi B^3}{\sqrt{2}B_{PA}}}, \tag{2.11}$$

where n_{in} is the noise in the deflection signal sent to the PLL, and B_{PA} is the bandwidth of the photodetector's preamplifier. Based on the above equations, for an amplitude of 5 nm, the thermal noise was estimated to be 0.09 Hz, while the noise from the electronics was about 3 Hz. The former value is an order of magnitude smaller than the measured value of 2.3 Hz, while the second value is comparable. Moreover, with the bandwidth modified by the 300 Hz low pass filter, the calculated electrical noise is 0.4 Hz, which is similar to the measured value of 0.34 Hz.

[9] The measured values of the slopes are -0.96 ± 0.02, -0.91 ± 0.02, and -0.95 ± 0.01 for the JEOL PLL, Nanosurf PLL, and Nanosurf PLL with the low pass filter, respectively.

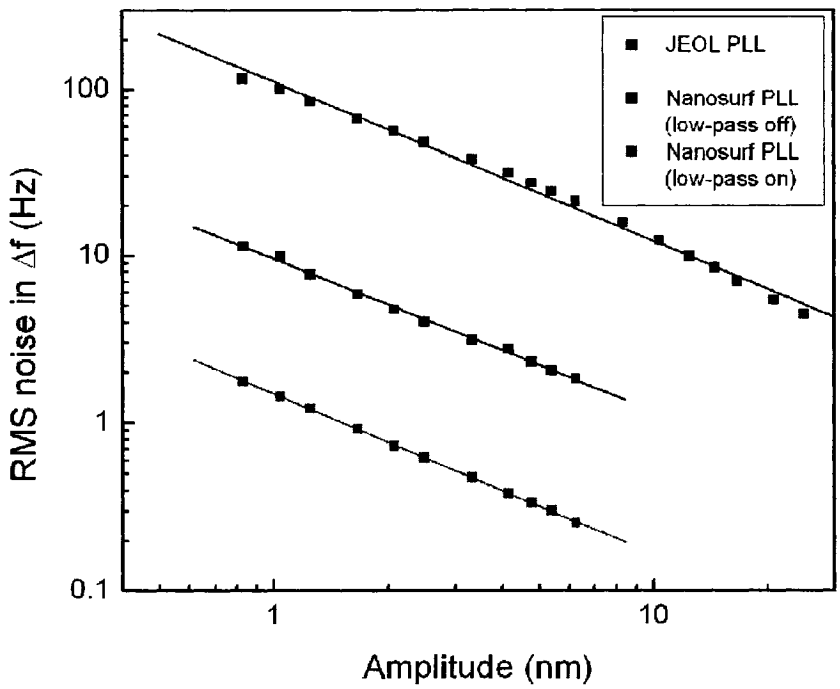

Figure 2.6: The dependence of the noise in the frequency shift as a function of the cantilever oscillation amplitude for the JEOL PLL, the Nanosurf PLL, and the Nanosurf PLL with a 300 Hz low pass filter.

The dependence of the frequency noise, given by equation 2.11, points to several means of improving the frequency resolution of the measurements. Firstly, it is evident that the noise is smaller at larger amplitudes. However, the oscillation amplitude affects the amount of time that the cantilever spends in close proximity to the sample. For large amplitudes, less time is spent near the sample, and as a result, the cantilever is less sensitive to short range forces, which are important for high spatial resolution. Consequently, during NC-AFM imaging, the amplitude must be optimized by the user such that the amplitude is small enough to be sensitive to short range forces, but large enough to have a low noise level. Another way to improve the frequency resolution is to reduce n_{in}, the noise in the deflection signal. This can be accomplished by increasing the optical power of the laser diode, or by improving the sensitivity of the photodetector. Finally, as shown by the application of the 300 Hz low pass filter, the measurement can

be improved by reducing the bandwidth of the measurement. Nevertheless, one must be careful not to use a data acquisition rate which exceeds the low pass cutoff frequency. As shown in Figure 2.7, when the data acquisition rate is too fast, the value at each pixel is correlated with that of adjacent pixels in the fast scan direction. For the 300 Hz filter, and 256 x 256 data points, this means scanning slower than about one image per 3.5 minutes. This is slower than typical rates in AFM imaging of about one image per minute or less. Nevertheless, as it will be shown in Section 2.2.5, the instrument is very stable, and can scan very slowly without thermal drift problems. For most of the measurements presented in this thesis, the 300 Hz filter was used, along with a scan speed of about 8 minutes per image.

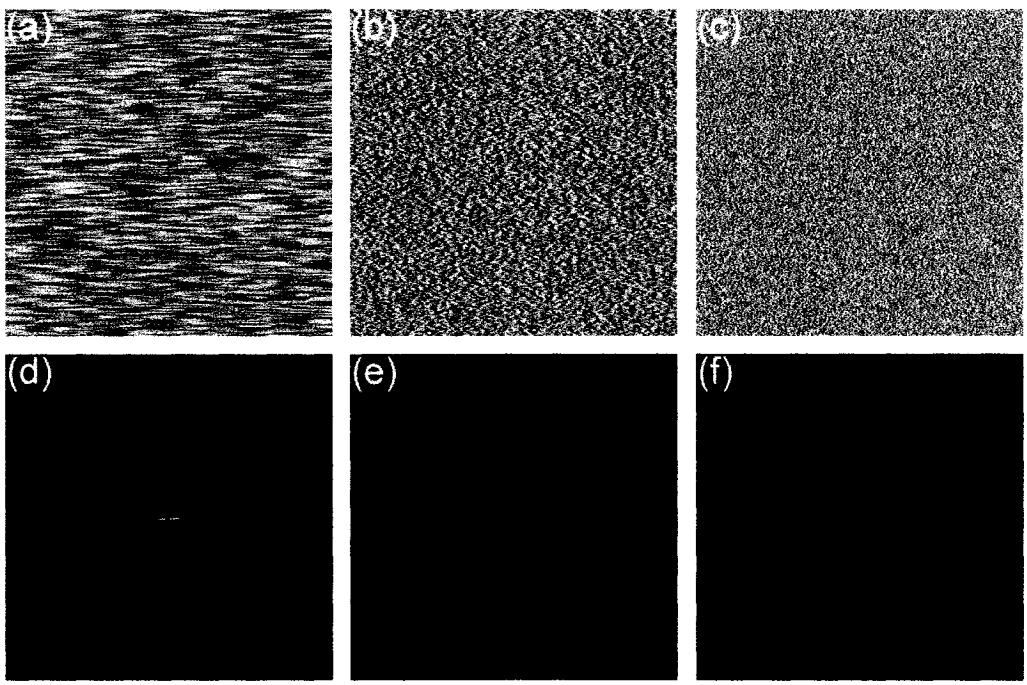

Figure 2.7: Images showing the noise in the frequency shift while scanning in the absence of a sample, and using the 300 Hz low pass filter. The scan rates are (a) 4.6 seconds per image, (b) 46 seconds per image, (c) 460 seconds per image. The corresponding spatial correlations between pixels are shown in (d), (e), and (f).

2.2.5 Drift and Stability

Thermal drift is characterized by shifts in the position of the AFM tip relative to the sample over time. This can stretch or compress the appearance of imaged features and lead to inaccurate distance measurements. Moreover, in cases of large thermal drifts, it may not be possible to perform high resolution measurements, since the objects of interest may move out of the way between scan lines. Drift can sometimes be avoided by scanning faster; however, this is at the cost of losing signal to noise. The drift can also be reduced by waiting for the sample to reach thermal equilibrium after sample preparation, and by waiting for the cantilever to reach thermal equilibrium after laser alignment.

The room temperature drift velocity was determined by repeatedly measuring the same area of a sample for 2 hours. The sample used for this set of experiments was a C_{60}-covered KBr surface. This system will be discussed in detail in Section 5.2.2. As shown in Figure 2.8, the shift from image to image was measured and plotted as a function of time. The thermal drift velocity, provided by the slope of the linear relationship, was determined to be 2.40 ± 0.02 nm/hr. This drift is very small for room temperature operation, and is only about 10 times larger than typical drifts at low temperatures [2]. The excellent stability of the instrument makes it possible to image areas as small as a few nanometers without significant distortion. In addition, very slow scan speeds can be employed in order to improve the signal to noise during measurement. Finally, although such measurements have not been considered in this thesis, with the observed stability, it should be possible to perform frequency shift versus distance measurements over specific atomic sites. Previously, this type of measurement has only been possible at low temperatures [28, 29].

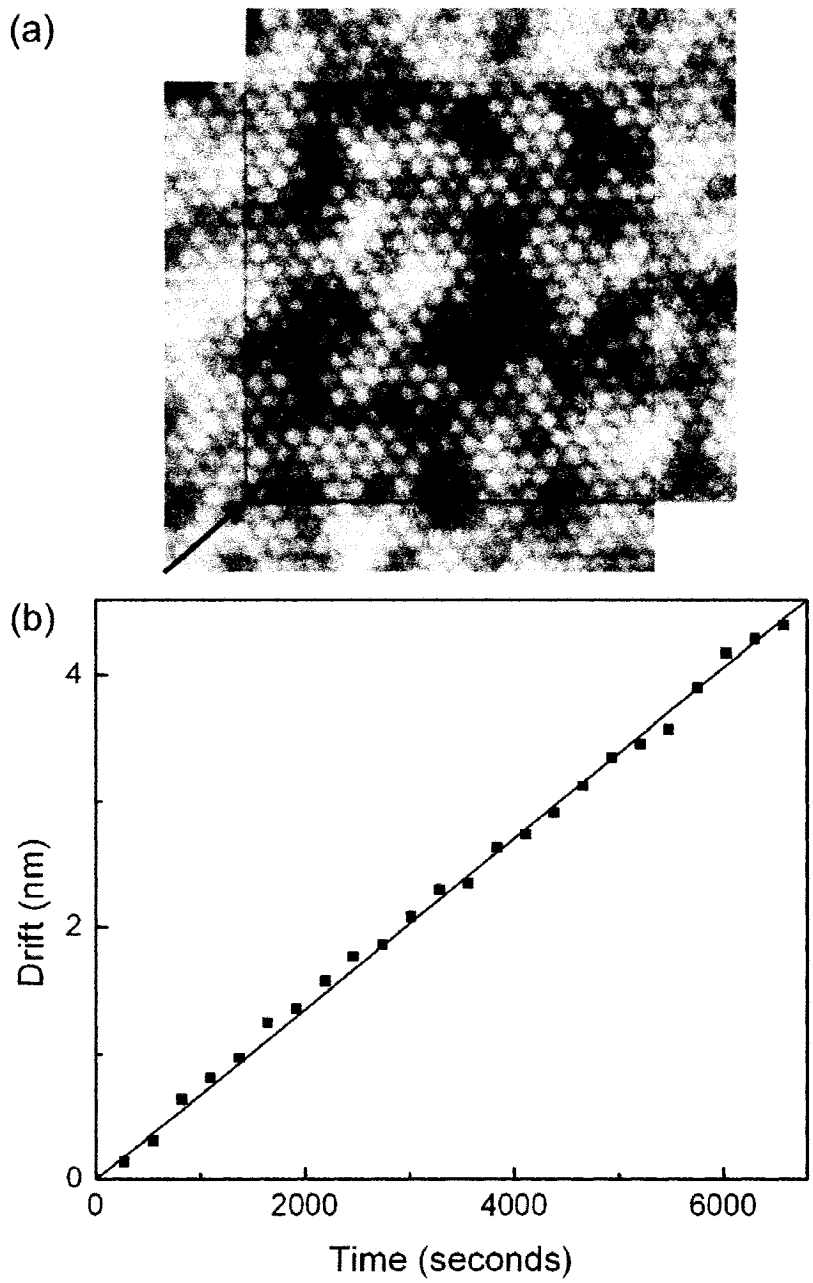

Figure 2.8: (a) Two overlaid NC-AFM images of C_{60} molecules on a KBr (001) surface showing a displacement due to thermal drift (20 nm x 20 nm, Δf = -9.8 Hz, images taken 2 hours apart). (b) A plot of the thermal drift as a function of time. The slope of the linear fit yields a drift velocity of 2.40 ± 0.02 nm/hr.

2.3 Sample Preparation

All of the sample preparation was done in UHV in order to have well-defined, clean surfaces. The only exception is the preparation for transmission electron microscopy, which was performed *ex situ*. The following sections describe the instruments and procedures used.

2.3.1 Sample Heater

The sample heater for cleaved samples[10] has a resistively heated tungsten filament which sits behind the sample holder. Calibration was done with a Chino IR-CAPP2CS pyrometer. The pyrometer measures emitted light, in this case, 2.0 μm infrared light, and converts the measurement to a temperature. A KBr crystal was coated with a 5 nm titanium adhesion layer and a 40 nm gold film in a separate vacuum system. The crystal was then mounted on the sample holder, introduced into the UHV system and heated with the sample heater. The temperature of the sample was measured as a function of the filament current. Figure 2.9 shows the calibration plot over the full pyrometer measurement range. It was necessary to wait about 1 - 1.5 hours between data points to allow the system to reach thermal equilibrium.

[10] The heater for cleaved samples was designed by R. Hoffmann.

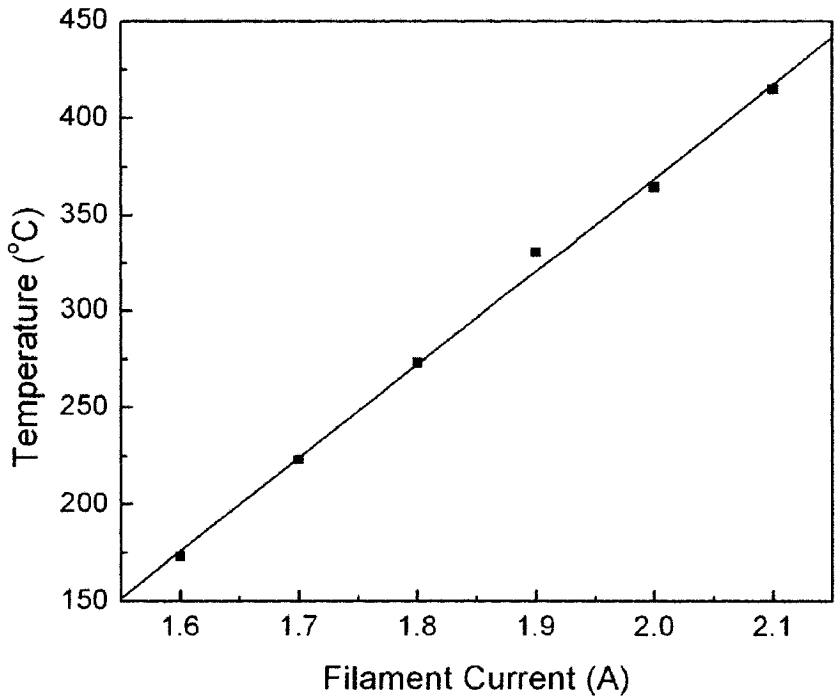

Figure 2.9: A plot showing the measured sample heater calibration, with a linear fit.

The greatest source of error is the uncertainty in the emissivity. The emissivity is the fraction of the incident radiation energy which is absorbed by an object [30]. In order to convert the temperatures properly, the emissivity value must be entered into the pyrometer. A gold film was chosen for the calibration because its emissivity is tabulated. However, the exact value depends on the surface roughness. The emissivity of gold at the measurement wavelength of 2.0 μm can range from 0.01 - 0.1 [31][32]. A value of 0.05 was used. By testing different emissivity compensation values, it was determined that the uncertainty in the measurements is about 10 %. It should be noted that the gold film was also used so that the pyrometer would not have a direct view of the filament, as it would through the optically transparent KBr. This ensures that the measured temperature is that of the sample and not the filament. Furthermore, a KBr crystal was used as the substrate for the gold film so that the conditions approximate those used during the experiments with KBr samples.

2.3.2 Electron Beam Evaporator

Metal deposition was carried out with an Oxford Applied Research EGN4 electron beam evaporator. The evaporator is also capable of evaporating other materials such as molecules or ionic crystals. It has four sources, each of which can either be mounted as a rod or contained in a crucible. A schematic of a single source is shown in Figure 2.10. During evaporation, the target material or crucible is held at a potential of +2 kV. Electrons are emitted by a grounded filament and are accelerated towards the target. The electron bombardment causes the target to heat up and evaporate material. In order to maintain the rest of the evaporator at an ambient temperature, the instrument is water cooled. This prevents unwanted outgassing or evaporation from nearby surfaces during evaporation. The evaporator is also equipped with an ion current detector which measures a fraction of the ionized target atoms created during evaporation. This can be used as an indicator of the evaporation rate (see Appendix B). In addition, the power unit has a feedback circuit for keeping the rate constant. To minimize the amount of charge reaching the sample during deposition, the evaporator is fitted with a grid which is held at a potential of +2 kV. This potential deviates positive ions and collects electrons; nonetheless, some charge still reaches the sample. A thorough characterization of the charge emitted from the evaporator and measurements showing the effect of the charge on the KBr (001) surface are presented in Chapter 3. The effect of the charge on metal growth is discussed in Chapter 4.

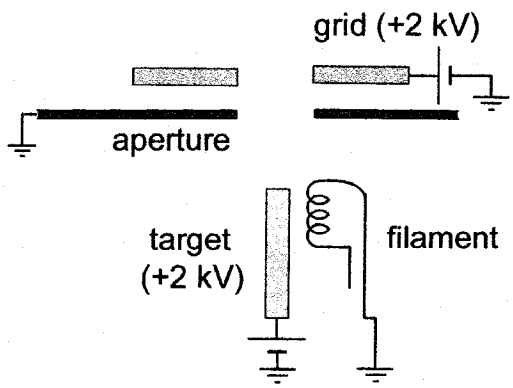

Figure 2.10: A schematic of an electron beam evaporator source (not to scale).

Three metals were used in the growth experiments: gold, tantalum, and palladium. Because of problems with melting during evaporation from rods, the gold (Alfa Aesar, 99.999% purity) was evaporated from a molybdenum crucible. The tantalum (Alfa Aesar, 99.95% purity) and the palladium (Alfa Aesar, 99.95% purity) were both evaporated from rods. Prior to evaporation, the sources were outgassed for 1 - 2 days.

The rate during deposition was measured with a water cooled Inficon quartz crystal monitor. The monitor is mounted on a bellows so that it can be advanced in front of either the electron beam evaporator or the molecule evaporator for rate calibration, and then retracted for deposition on the substrate. The thickness of a deposited film Δt is determined by measuring the change in resonance frequency Δf as the crystal's mass is slightly increased by Δm:

$$\Delta f = \frac{C}{A}\Delta m = C\rho\Delta t, \tag{2.12}$$

where A is the exposed area of the quartz crystal, C is a constant related to the properties of the quartz crystal, and ρ is the density of the deposited material [1]. The time dependence of the coverage is used to calculate the deposition rate and to ascertain that it is constant. It was necessary to use a very low rate for the metal growth experiments (0.008 nm/min), in order to accurately deposit low coverages. The use of low rates also reduces kinetic effects during growth. To measure these rates, it was necessary to supply the instrument with a density value of one tenth the true value. This provided an extra factor of 10 in the sensitivity of the measured coverage [33].[11]

Although the coverage is measured as a thickness, in nanometers, when dealing with coverages of less than a few nanometers, it is common to express the coverage in terms of *monolayers* (ML). There are two accepted definitions of a monolayer [34]. One convention describes a monolayer as a complete single layer of overlayer material. This

[11] The sensitivity of the frequency measurement remained the same; however, the conversion to units of thickness by the quartz monitor gained one digit of accuracy.

is a natural definition when the film structure is known and the thickness of a single layer can be identified in terms of a lattice spacing. In many cases, the overlayer structure is not known, or there are several coexisting structures; for example, some islands may grow with the (111) plane parallel to the substrate, while others grows with the (001) plane parallel to the substrate. In these situations, either a specific film structure must be assumed, or a monolayer must be defined in terms of the substrate's structure. More specifically, the second definition refers to a number density of deposited atoms/molecules which is equal to the number density of lattice sites on an ideal non-reconstructed substrate surface. This definition is not well suited for molecular systems where the molecules are much larger than the surface atoms, since the number densities involved in the two systems are considerably different. The molecular structures considered in Chapter 5 have known orientations and lattice spacings. Therefore, the first definition of a monolayer can be applied. The structure of the deposited metals is less well known. However, to avoid confusion, instead of using the second definition of a monolayer, the metal coverages will simply be expressed in nanometers.[12]

2.3.3 Molecule Evaporator

The molecule evaporator (Kentax TCE-BSC) has three sources, each of which is contained in a quartz crucible and is heated via surrounding heating wire. The unit has a feedback circuit for maintaining a constant temperature during evaporation. The evaporator also has water cooling, so that the adjacent sources are not heated during evaporation. Because the evaporator is mounted on a retractable bellows with a gate valve in front, it is possible to change the sources without breaking vacuum in the preparation chamber. In addition, by advancing or retracting the evaporator, it is possible to vary the deposition rate without changing the evaporation temperature. The deposition rate and coverage are measured with the quartz microbalance. Because the sources are

[12] For reference, taking the K + Br basis as a substrate lattice site, 1 nm = 3.2 ML for gold, 1 nm = 3.0 ML for tantalum, and 1 nm = 3.7 ML for palladium.

thermally heated to relatively low temperatures ($\leq$ 330 °C), there is no measurable charge emitted during the molecule evaporation.

Two molecules were used: PTCDA and C_{60}. The PTCDA (Alfa Aesar, 98% purity) was outgassed prior to evaporation at 230 °C for 12 hours. The PTCDA was deposited by heating the source to 300 °C. C_{60} (Alfa Aesar, 99.95 % purity) was outgassed at 220 °C for 12 hours and evaporated at 330 °C. The unit of a monolayer (ML) will be used to describe the coverage of the molecules. A ML is taken to represent a single layer of molecules. For PTCDA, 1 ML = 0.32 nm, while for C_{60}, 1 ML = 0.82 nm.

2.3.4 The Substrate: KBr (001)

Potassium bromide (KBr) was selected as a substrate for three main reasons: (1) it is electrically insulating; (2) it is possible to prepare UHV-clean surfaces with atomically flat terraces extending over several hundred nanometers (Figure 2.11 (a)); and (3) the surface can be imaged with atomic resolution by NC-AFM (Figure 2.11 (b) and [7, 35]). KBr has the same crystal structure as sodium chloride, which is akin to a three-dimensional chess board, with alternating positive alkali and negative halogen ions. It has a lattice constant of 0.66 nm. Figure 2.11 (c) shows a schematic of the (001) plane. It should be noted that during NC-AFM imaging, one of the ionic species appears as corrugation maxima, while the other appears as corrugation minima, depending on the charge of the AFM tip apex [36]. A positively terminated probe tip measures positive ions as protrusions. Conversely, a negatively charged tip measures negative ions as protrusions. A means of identifying the imaged surface ions will be discussed in Section 5.2.1.

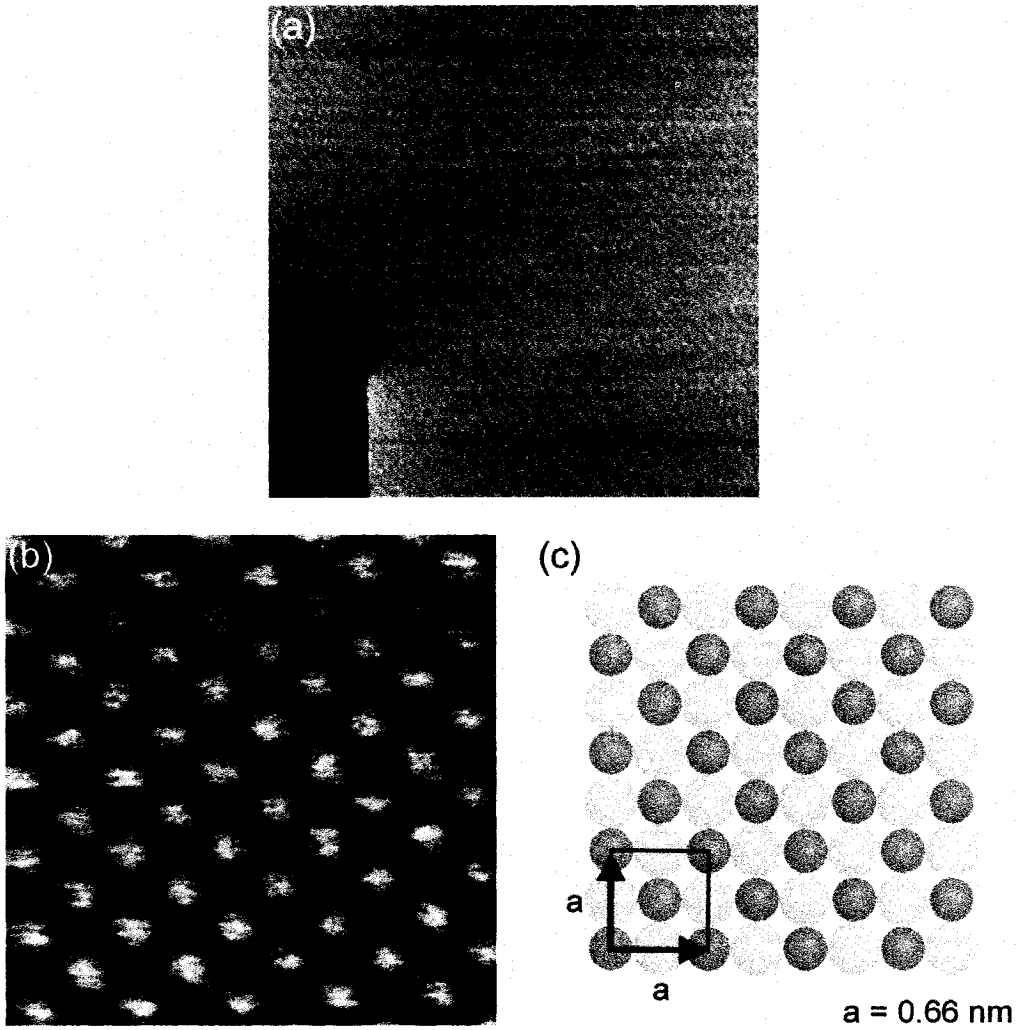

Figure 2.11: NC-AFM images of the KBr (001) surface: (a) An 800 nm x 800 nm overview showing a large atomically flat terrace with a single screw dislocation (Δf = -1.6 Hz); (b) a 3 nm x 3 nm atomic resolution image (Δf = -29.5 Hz). (c) A schematic of the KBr (001) surface, with the surface unit cell outlined (blue = K^+, yellow = Br^-).

The KBr samples were prepared by cleaving a single crystal (supplied by Korth Krystalle) *in situ*. Before introducing the crystal into the UHV system, the crystal is cleaved with a razor blade along {100} planes into a rectangular block with dimensions of about 1.5 mm x 6 mm x 10 mm. The sample is then clamped into the sample holder with a spacer plate and two set screws, such that a (001) face is parallel to the holder and

the sample protrudes normal to the holder surface (see Figure 2.12). After the sample is introduced into UHV, the sample is cleaved along the (001) plane by pressing a metal block into the protruding part of the sample (Figure 2.12 (b)). It has been empirically observed that moving the block gradually produces better results; i.e., this produces samples with minimal surface charge and large atomically flat terraces. It is thought that a slower movement allows the stress in the crystal to build up little by little until there is just enough energy to break along the (001) plane. If too much energy is supplied to the system, the crystal may break along less favoured planes and form many facets. Following exposure of the clean (001) face, the sample is heated for 1 hour at 150 °C to remove any residual surface charge. Next, the quality of the surface is verified by NC-AFM. The sample is then returned to the preparation chamber for creating nanostructured pits in the surface (Chapter 3), depositing metals (Chapter 4), or depositing molecules (Chapter 5). It is very important that the ion gauges are kept off for the duration of the experiment since the charge given off by the gauges can damage the KBr surface.

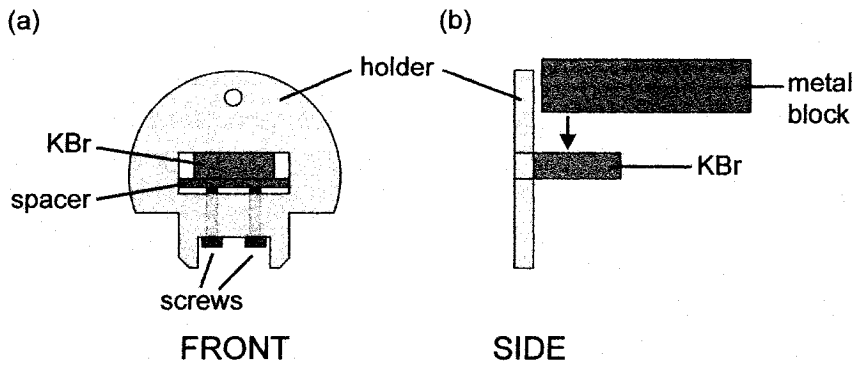

Figure 2.12: Schematic diagrams showing the sample holder used for cleaving: (a) a front view, (b) a side view, also showing the geometry during cleaving.

2.3.5 Preparation for *Ex Situ* Transmission Electron Microscopy

Transmission electron microscopy (TEM) was used to measure some of the nanostructures resulting from metal growth on KBr. The following procedure, adapted from Bassett [37], was used to prepare the samples for TEM observation. First, the KBr samples were removed from the UHV system and promptly introduced into another vacuum chamber for carbon coating. The samples were exposed to air for less than one minute prior to coating. After depositing 8 - 10 nm of carbon, the carbon film and the embedded metal nanostructures were separated from the KBr substrate by gradually immersing the sample, with the film side up, at a 45° angle into a container of water. Finally, a wire formed into a 2 mm diameter loop was used to lift a portion of the film off the water surface and place the film onto a copper TEM grid.

The TEM was operated by Prof. H. Vali at the Electron Microscopy Center of McGill. The high resolution measurements of gold nanostructures shown in Section 4.2 were measured with a JEOL JEM-2010, using an acceleration voltage of 200 kV. The measurements of tantalum nanostructures, presented in Section 4.3, were performed using a JEOL 2000FX TEM, with an acceleration voltage of 80 kV.

3 Nanostructured Pits

3.1 Introduction to Charge-induced Desorption

While surface modifications created by charge-induced desorption have been of fundamental interest for several decades [38, 39], there is renewed interest in the field because of its relevance to nanofabrication [11]. Moreover, the recent development of NC-AFM has opened up the possibility of measuring the topography of modified insulators with atomic resolution [7, 40]. This is of great importance since the influence of surface topography on the desorption process leading to surface modification remains largely unknown [38].

Through excitation by electrons [38], photons [41], or ions [42], the desorption of atoms from ionic crystal surfaces is induced by the creation, diffusion and relaxation of electron-hole pairs and excitons (lattice ions in excited states) in the bulk. A single incident particle can generate many excitations in a lattice, leaving a trail of electron-hole pairs and excitons along the particle trajectory [43].[13] These excitations lead to atom desorption via one of two mechanisms: non-thermal and thermal desorption.

The non-thermal process involves the diffusion of the initial excitations (electrons, holes and excitons) to the surface. In alkali halides, such as KBr, this process favours the emission of halogen atoms, leaving the surface alkali enriched [44]. The halogen emission is induced by the localization of a hole on a surface halogen ion, which causes the Coulomb interactions with its alkali neighbours to disappear [45].

The thermal desorption of surface atoms is caused by the thermalization of the initial excitations. This results in the creation of pairs of Frenkel defects, most commonly F-

[13] For example, a 1 keV electron has a penetration depth of about 100 lattice constants and creates about 100 electron-hole pairs [43].

centers and H-centers. An F-center is an electron trapped in a halogen vacancy and an H-center is an interstitial halogen atom which forms a singly ionized dihalide [46] (see Figure 3.1). The diffusion of these defects and their recombination with the surface result in surface atom desorption. F-centers are only mobile when they are in an excited state. Recombination with the surface causes thermal alkali atom emission. This occurs mainly at step edges, kinks, and corner sites [43], although it is thought that groups of F-centers, so-called X-centers, can also produce alkali emission from terraces [47]. H-center recombination with the surface yields halogen atom emission. However, this process does not produce a modified surface, as the emission of an interstitial halogen restores a perfect surface. Thermal emission dominates under conditions of low beam intensities and high sample temperatures [38].

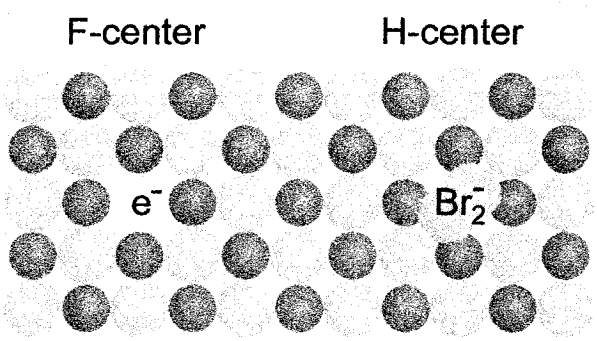

Figure 3.1: Schematic of an F-center and an H-center in a KBr crystal (blue = K^+, yellow = Br^-).

To date, few studies have investigated the effect of charge-induced desorption on surface topography. At the first stages of the typically layer-by-layer surface removal, monatomic-depth rectangular pits, which are several nanometers in size, are formed. At higher doses of charge, the pits expand and coalesce with other pits. Surface removal from the next layer usually begins prior to complete removal of the previous layer. The characteristic pits were first observed by transmission electron microscopy, by decorating the step edges with metal clusters [41]. Later AFM studies in air [48], and NC-AFM

studies in UHV [7, 38] provided direct evidence that the pits are one atomic layer deep, and are aligned with the <100> directions of the alkali halide crystal. Furthermore, the desorption rate has been correlated with the density of the steps on the surface, supporting the theoretical work which suggests that the desorption occurs mainly from low-coordinated sites [38]. Based on the scarcity of observed kink sites (one or less per pit), it has been suggested that pit expansion proceeds mainly through a series of desorption events from kinks, sequentially "unzipping" the atoms from the pit's perimeter [7, 43].

Recently, rectangular pits in an alkali halide surface have been used to trap small numbers of subphthalocyanine molecules [11]. These well-defined surface features may also serve to control the nucleation of metal nanostructures at surfaces [41, 49]. The use of nanostructured pits for modifying the growth of metals and molecules will be addressed in later chapters.

In this chapter, a new method of pit creation is demonstrated. This technique involves the use of an electron beam evaporator as a source of charged particles. It was realized that the evaporator could be used for surface modification after characterizing the charge emitted by the evaporator, initially as part of a study of the role of defects in the nucleation of metals (discussed in Chapter 4).

3.2 Characterization of the Charge Emitted by the Electron Beam Evaporator

During operation, an electron beam evaporator emits charged particles as a result of the ionization of residual gas in the vacuum chamber, the ionization of target material, and the production of low energy secondary electrons. The ions created from the residual gas are expected to be predominantly H_2^+, dissociated H^+, and CO^+, since H_2 and CO are the most abundant residual gases in a UHV system [1]. To reduce the amount of charge impinging on the sample during evaporation, the evaporator is fitted with a grid held at 2 kV. With this setup, extremely small current densities are emitted (<500 pA/cm^2), making it possible to finely tune the irradiation dose to the sample. These current

densities are about 1000 times smaller than those typically used in desorption experiments [38]. The pits were created by operating the evaporator at a low power, such that the sample is irradiated with a well-defined dose of charge without depositing any material. At higher powers, both charge and evaporated material are emitted.[14]

In order to expose the samples to a well-defined dose of charge, the current emitted by the evaporator was characterized. The current to the sample position was measured by replacing the KBr sample with an electrically conducting sample (a copper-beryllium plate) and using a Stanford Research Systems SR560 low-noise current preamplifier. The results shown below are for a tantalum target in the evaporator. Similar measurements of gold and palladium sources were also carried out and are shown in Appendix B.

As shown in Figure 3.2 (a), as the power applied between the evaporator filament and the tantalum target is increased, the net current density I_{net} at the sample position increases linearly as a result of the increased ionization of the background gas by the electron-beam of the evaporator. At about 80 W, a deviation from linearity is observed due to the onset of evaporation and thus tantalum ions. Electrons also contribute to this measured current density. To determine the proportion of positive I_+ and negative I_- current density, the current density was measured as a function of sample voltage (Figure 3.2 (b)). At negative voltages, nearly all of the incoming electrons are deviated, resulting in a saturation of the current density. This saturated current density is the current due to positive ions, I_+. As the sample voltage is increased to positive values, electrons from the evaporator and greater numbers of stray scattered electrons are collected from the chamber, resulting in an increasingly negative current density. The electron current during pit creation is determined by calculating the difference between the net current at 0 V and the positive current:[15]

$$I_{net} = I_+ + I_- \rightarrow I_- = I_{net} - I_+. \qquad (3.1)$$

[14] The applied evaporator power is defined as the electron beam current times the target potential of 2 kV.
[15] The net current at 0 V is of relevance since 0 V is the condition used during pit creation.

The total current density I_{tot} incident on the sample is given by:

$$I_{tot} = I_{+} + |I_{-}| \tag{3.2}$$

Because of the nearly linear relationship between the current density and power, a universal relationship between current density and voltage is obtained by dividing the current density by the power (see Figure 3.2 (b) inset). This makes it possible to interpolate the current density for any applied power.

The energies of the incident charged particles can be deduced from the experimental setup (Figure 3.2 (a)-inset). The incident electrons are produced by thermionic emission from the tungsten filament and by secondary electron generation at the tantalum target. The electrons which leave the filament are those which have sufficient energy to overcome the work function, and therefore have energies of about 4.5 eV [50]. These electrons are accelerated towards the tantalum target and may produce electrons with energies ranging from 0 - 2 keV. However, the electrons which reach the sample are decelerated by the 2 kV potential between the grid and sample, and are left only with their initial energy of about 4.5 eV. Conversely, the positive ions, created by the ionization of the background gas, are accelerated by the potential between the grid and sample, and have an energy of 2 keV.

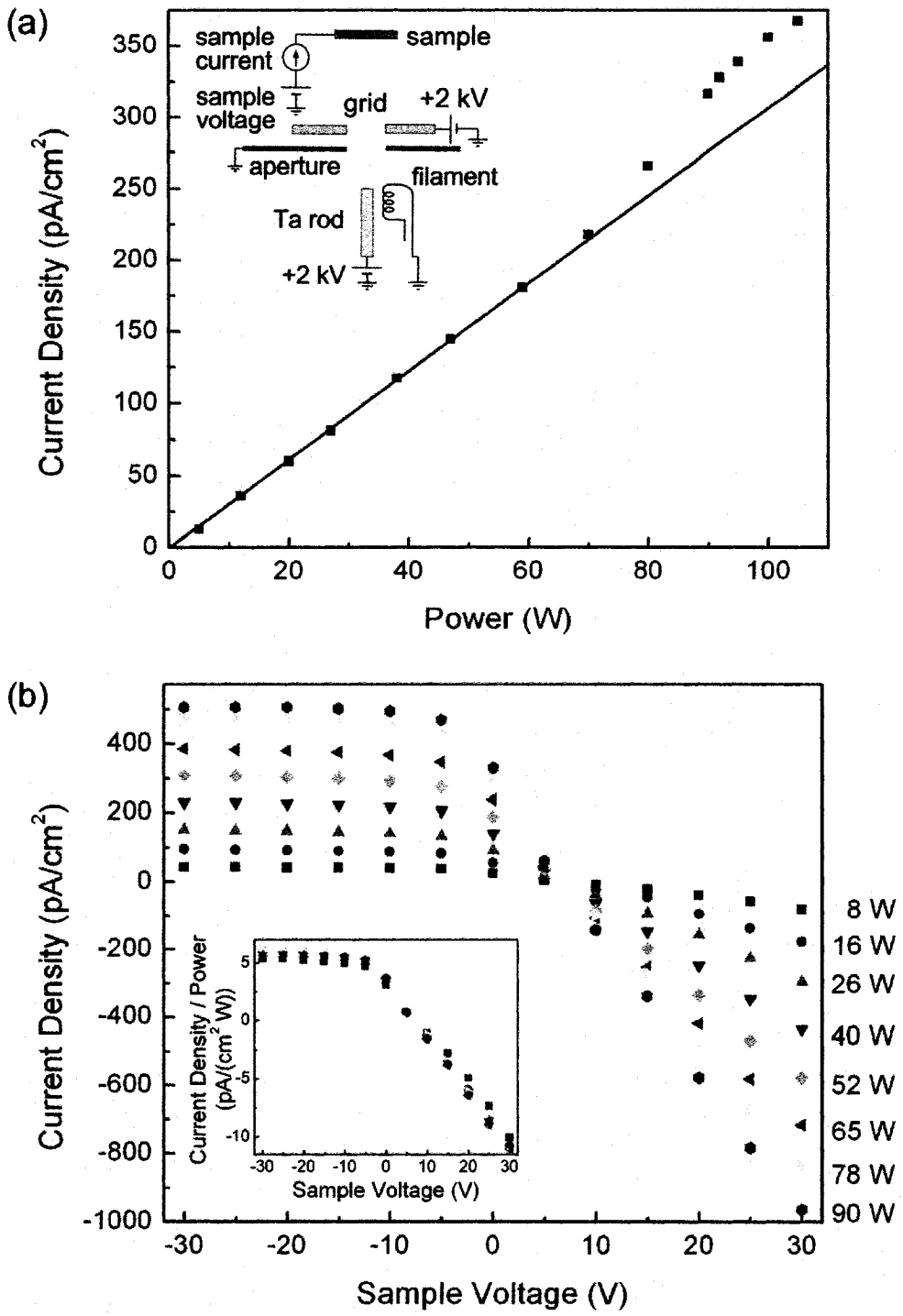

Figure 3.2: Current density at the sample position as a function of (a) applied evaporator power (inset shows a schematic of the experimental setup), and (b) sample voltage. A universal relationship between current density and voltage is obtained by dividing the current density by the power (inset).

Further analysis of the current density-voltage characteristics support this physical picture. At voltages just above the ion current saturation region, the electrons have just enough energy to overcome the applied potential; i.e., the electrons are not significantly retarded or accelerated, and have approximately random motion. Assuming a Maxwellian velocity distribution, the Boltzmann relation gives [51, 52]:

$$|I_-| \propto \exp(eV/k_BT), \tag{3.3}$$

or,

$$\frac{d\ln|I_-|}{dV} = \frac{e}{k_BT}, \tag{3.4}$$

where e is the magnitude of the electron charge, V is the applied voltage, k_B is the Boltzmann constant, and T is the temperature. Since the positive ions are too energetic (2 keV) to be deviated by the applied voltage (< ± 30 V), the positive current density I_+ is constant and can be subtracted from the measured characteristic curve, leaving I_-. A plot of $\ln|I_-|$ as a function of applied voltage is shown in Figure 3.3. As per equation 3.4, the slope in the region just above ion saturation provides an estimated electron energy of 5 ± 1 eV. This is in close correspondence with the expected value of 4.5eV from thermionic emission.

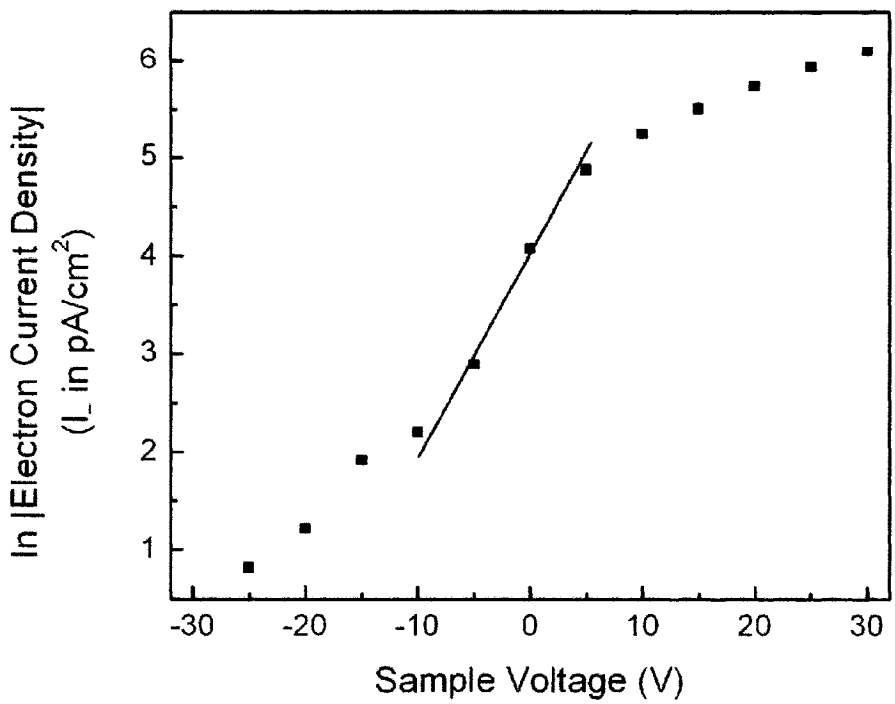

Figure 3.3: A plot of the natural logarithm of the electron current density as a function of applied sample voltage. The slope at voltages just above ion saturation provides an estimate of the incoming electron energy (evaporator power P = 26 W).

The largest contributions to the uncertainty in the current measurements are from the generation of secondary electrons during the ion bombardment and from the reflection of incident electrons. The ions are detected as positive charge at the sample position because of ion neutralization. When a low energy (0.5 – 3.0 keV) positive ion approaches a metal surface, charge is transferred from the valence electrons of the sample to the ion, leaving a hole in the valence band. A typical efficiency for this process at the energies under consideration is 99.99% or higher [34]. During ion neutralization, a secondary electron is potentially emitted as a result of a two electron Auger process. After the first electron tunnels into the ion, and relaxes to the ground state, the energy given up by the electron is available to excite a second electron, which may be released from the metal. This can occur provided

$$(I-\phi)e > \phi e \text{ or } I > 2\phi, \tag{3.5}$$

where I is the ionization energy of the gas atom, and ϕ is the work function of the metal [1] (see Figure 3.4). In the case under consideration here, the ionization energy of H_2, dissociated H, and CO are in the 13 - 16 eV range [53]. The work function of copper-beryllium is about 4 eV [54]; thus, the condition for electron emission is satisfied. The yield of electrons for the bombardment of copper by 2 keV H_2^+ and H^+ ions is about 0.2-0.3 electrons/ion [54].[16] The ejected electrons are registered in the current measurement as positive current to the sample; therefore, the positive current density I_+ is in fact 20 – 30 % smaller than the measured value.

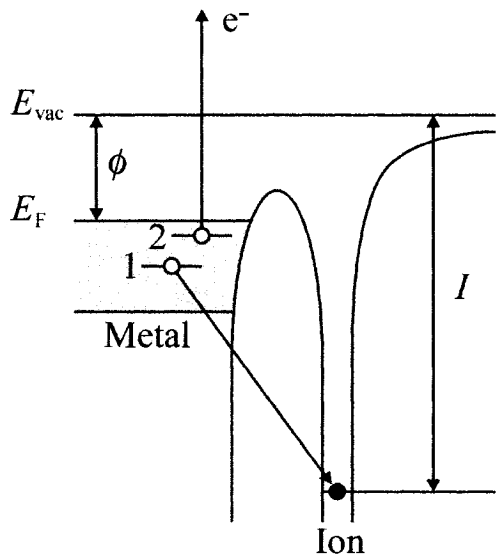

Figure 3.4: Potential energy diagram for the process leading to electron emission during positive ion bombardment.

The reflection of the incident thermal electrons must also be considered. At very low energies (<5 eV), the only electrons leaving a surface are those which are elastically reflected [55]; other electrons have insufficient energy to overcome the work function.

[16] Since data for copper-beryllium is unavailable, it is assumed that copper has similar characteristics.

The reflection coefficient for 4.5 eV electrons on copper is about 0.2 - 0.4 [55]. The exact value depends on the surface roughness and structure. Thus, in the experiments under consideration, about 20 - 40 % of the incident electrons did not register in the current measurement, implying a 20 - 40 % underestimate of the electron current density, I_-.

Corrected total current densities I_{tot} were calculated by taking into account the 20 - 30 % overestimate in the positive ion current density, I_+, and the 20 - 40 % underestimate in the electron current density, I_-. Furthermore, based on the above considerations, the beam of charge was determined to be made up of 60 ± 4 % positive ions and 40 ± 4 % electrons, with a slightly higher proportion of positive charge during tantalum evaporation.[17]

3.3 Dependence on Dose

For these experiments, the sample was held at 250 °C during charge irradiation. A tantalum source was employed, with a power of 26 W, corresponding to a total current density of 190 ± 10 pA/cm^2.

As shown in Figure 3.5, arrays of rectangular pits were produced in atomically flat terraces, sometimes extending over areas larger than 1 μm^2. The pit edges are along the <100> directions. At atomic steps, a restructuring takes place, which also favours <100> directions (Figure 3.5 (b)). In accordance with earlier observations of electron irradiated surfaces [7], high resolution images show that the structure and stoichiometry of the KBr (001) surface are preserved in the pit creation process (Figure 3.5 (d)).

[17] The uncertainties in the total current density and the charge proportions represent the ranges of values provided by the overestimate in I_+ and the underestimate in I-.

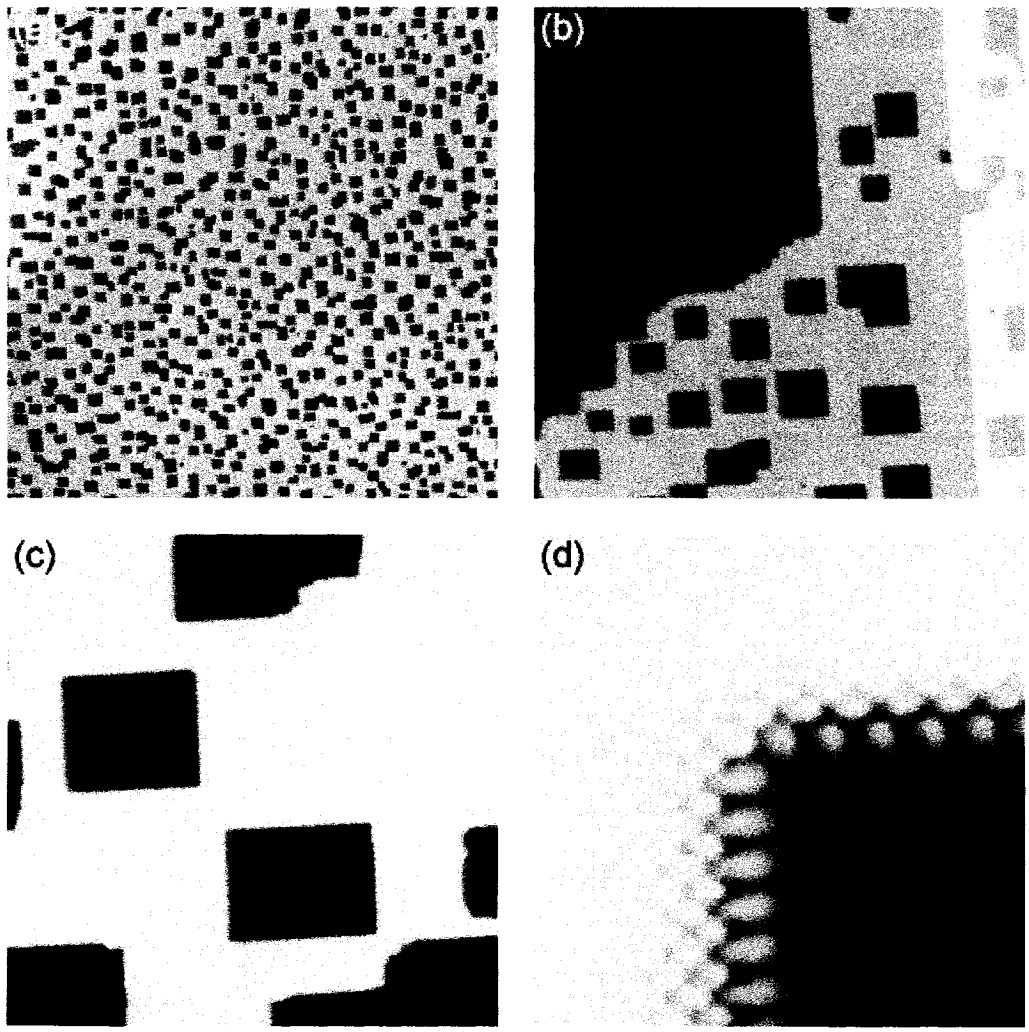

Figure 3.5: NC-AFM topography measurements of rectangular pits in a KBr (001) surface (irradiation dose = 1.2 ± 0.1 μC/cm^2): (a) 1 μm x 1 μm overview of pits created in a large atomically flat terrace (Δf = -3.6 Hz), (b) 300 nm x 300 nm image of pits and modified KBr steps (Δf = -4.4 Hz), (c) 100 nm x 100 nm pit close-up (Δf = -5.1 Hz), and (d) a high resolution 6 nm x 6 nm image showing the atomic structure in a pit (Δf = -6.5 Hz).

Small and large rectangular pits were created in a KBr surface by using doses of 0.12 ± 0.01 μC/cm^2 and 1.2 ± 0.1 μC/cm^2 (see Table 3.1 and Figure 3.6). As expected, a tenfold increase in dose leads to a nearly tenfold increase in the total amount of desorbed

surface area. The presence of extended terraces made it possible to measure the size distributions of the pits. Histograms based on the analysis of more than 10 images are shown in Figure 3.6 (c). The mean area of the small and large pits is 42 ± 2 nm^2 and 390 ± 10 nm^2, corresponding to a mean side-length of 6.5 ± 0.2 nm and 19.8 ± 0.3 nm, respectively. Although there is currently no theoretical framework for describing the pit size distribution, the similarities between the distributions suggest a scaling behaviour, analogous to that for island growth [56, 57]. The deviation between the distributions at high values is due to the coalescence of nearby large pits. Both samples have pit densities of 510 ± 20 / μm^2. In the language of growth studies (see Section 4.1), these samples are in the "pure growth" regime; i.e., the pit density is saturated [57]. Pits created with a current density of 390 ± 30 pA/cm^2 showed the same characteristics as the 190 ± 10 pA/cm^2 samples, showing that the pit size and density do not depend on the current density.

Table 3.1: Measured sample characteristic for small and large pit samples.

Sample	Current density (pA/cm^2)	Dose ($\mu C/cm^2$)	Pit density ($/\mu m^2$)	Mean pit area (nm^2)	Percent area desorbed (%)	Atoms desorbed per charge (/|e|)
Small pits	190 ± 10	0.12 ± 0.01	510 ± 20	42 ± 2	2.15 ± 0.05	26 ± 2
Large pits	190 ± 10	1.2 ± 0.1	510 ± 20	390 ± 10	26.8 ± 0.4	33 ± 3

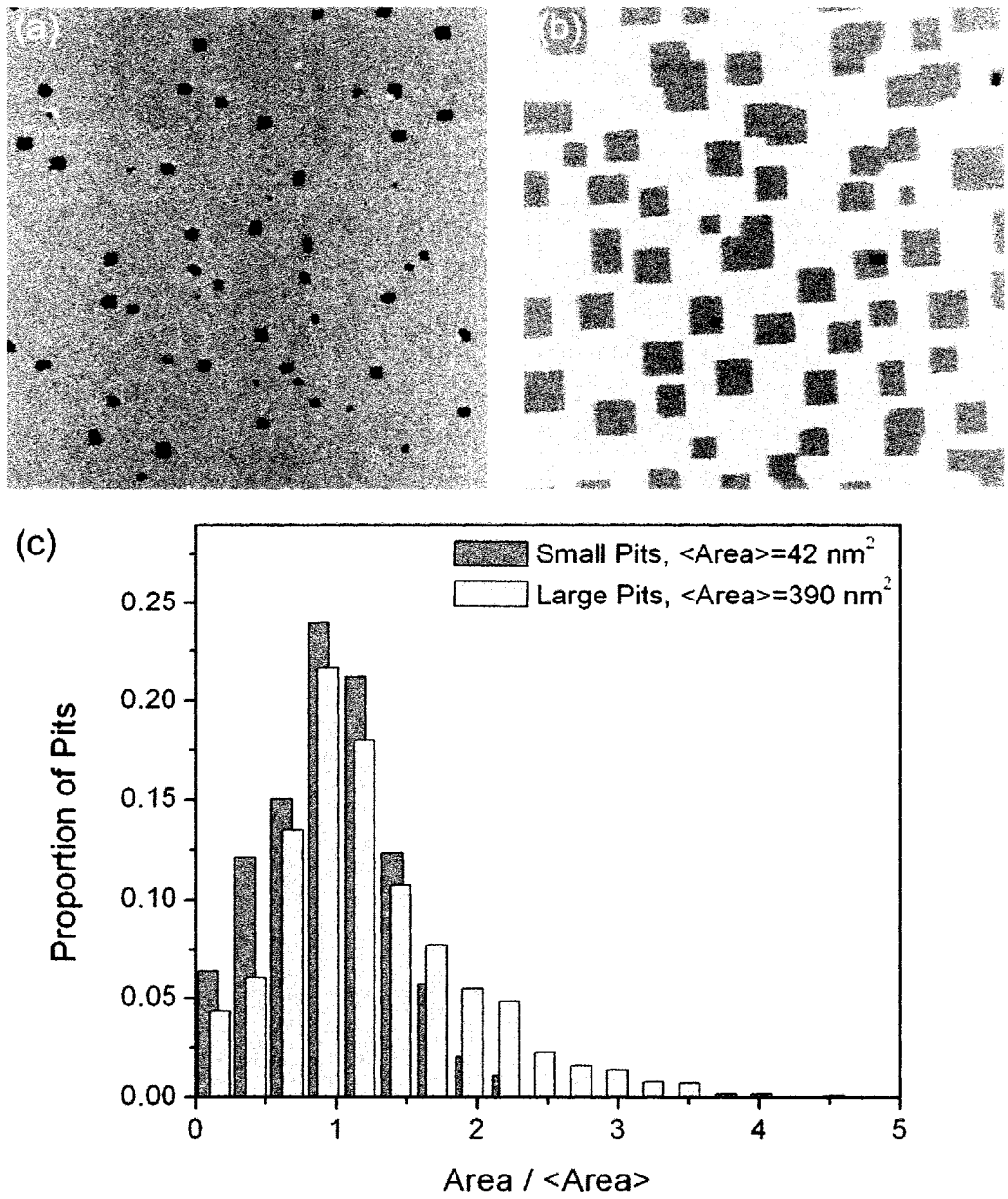

Figure 3.6: Small and large rectangular pits in a KBr (001) surface (300 nm x 300 nm): (a) small pits (dose = 0.12 ± 0.01 μC/cm^2, Δf = -3.7 Hz), and (b) large pits (dose = 1.2 ± 0.1 μC/cm^2, Δf = -4.5 Hz). (c) The pit size distributions.

Interestingly, a minimum pit size was observed to exist (see Figure 3.7). It is hypothesized that these smallest pits are due to the impingement of single charged particles. To test this idea, the number of atoms missing in the smallest pits was compared with the average number of desorbed atoms per incident charged particle. The average area, based on the measurement of 6 minimum area pits, is 3.0 nm^2, with a standard deviation of 0.6 nm^2. This corresponds to the desorption of 28 ± 5 atoms. Based on the measurements of the total charge incident on the sample and the total surface area missing, on average, 33 ± 3 atoms were ejected per charged particle for the large pits and 26 ± 2 atoms per charged particle for the small pits. Both of these values correspond well with the number of atoms missing in the smallest pits. The reduced desorption rate for the sample with the smaller dose is consistent with the experiments of B. Such *et al.*, which show a modulation in the desorption rate depending on the stage in the layer-by-layer desorption process [44]. At the earliest stages of desorption, the desorption rate is somewhat suppressed, because of the relative scarcity of low-coordinated sites such as steps and kinks, where desorption is initiated. It should be noted that these smallest pits are sufficiently small to potentially immobilize and isolate individual large molecules. The trapping of molecules in pits will be discussed in Section 5.2.

Figure 3.7: The smallest observed pits for samples prepared at 250 °C are 3.0 ± 0.6 nm^2 in size: (a) 100 nm x 100 nm (Δf = -3.6 Hz), (b) 10 nm x 10 n m (Δf = -10.2 Hz).

The observed desorption efficiencies are high compared to other studies, where rates below 12.3 atoms per electron are seen [38]. There are several possible reasons for the increased efficiency, all of which may contribute to varying degrees. Firstly, during evaporator operation, the electron-emitting evaporator filament and the target glow bright white. Assuming blackbody behaviour, some of the emitted photons are in the ultraviolet range [30]. Ultraviolet light is known to produce pits in alkali halides [48]. Furthermore, visible wavelength light can potentially enhance desorption by further exciting excitons after they are created by other means. X-rays produced by bremsstrahlung radiation and core level transitions in the evaporator target may also cause desorption in the sample [58]. Finally, the temperature during pit creation is also a factor [38]. The temperature used in these experiments, 250 °C, is higher than that used in other studies.

3.4 Dependence on Substrate Temperature

A gold evaporator target was used for this set of experiments so that the results would serve as a reference for studying the role of defects during gold growth (Section 4.2). It should be noted that the desorption efficiency with the gold target was low in comparison with the tantalum target, about half the rate. There are several possible reasons for this. Firstly, for the gold source, there is a smaller proportion of 2 keV positive ions, 44 ± 4 % versus 60 ± 4 % for tantalum. Secondly, the gold evaporates at a lower power, 14 W versus 26 W, which results in the production of less visible, ultraviolet, and x-ray light.

The samples were prepared at three temperatures: 293 K, 423 K, and 523 K. Some sample characteristics are tabulated in Table 3.2. Representative images are shown in Figure 3.8. The most prominent trend is the sharp decrease in the number density as a function of temperature. This reflects a longer diffusion length for the excited F-center at higher temperatures. The diffusion length roughly corresponds to the average separation between the pits, measured to be 15 ± 1 nm, 27 ± 1 nm, and 28.5 ± 0.5 nm at 293 K, 423 K, and 523 K, respectively (see Figure 3.8 (d)). These pit separations are somewhat larger than those found by Kolodziej *et al.*, who measured distances of about 10 nm at

410 K and 20 nm at 470 K [47]. The pit size and the desorption efficiency also increased with temperature; however, the differences between the 423 K and 523 K samples are small (see Table 3.2). Qualitative inspection of Figure 3.8 shows that the pit size and desorption efficiency at 293 K are significantly smaller than at the higher temperatures. However, it was not possible to measure these quantities for the 293 K sample, owing to the different character of this sample, that is, the presence of protrusions in addition to pits.

Table 3.2: Temperature dependence of several measured sample characteristics.

Sample temperature during prep. (K)	Current density (pA/cm^2)	Dose ($\mu C/cm^2$)	Pit density ($/\mu m^2$)	Mean pit area (nm^2)	Percent area desorbed (%)	Atoms desorbed per charge ($/|e|$)
293	114 ± 8	0.36 ± 0.03	1760 ± 60	*	*	*
423	114 ± 8	0.36 ± 0.03	610 ± 20	63 ± 3	3.8 ± 0.1	15 ± 2
523	114 ± 8	0.36 ± 0.03	510 ± 20	86 ± 4	4.3 ± 0.1	18 ± 2

* It was not possible to measure the pit areas for the 293 K sample.

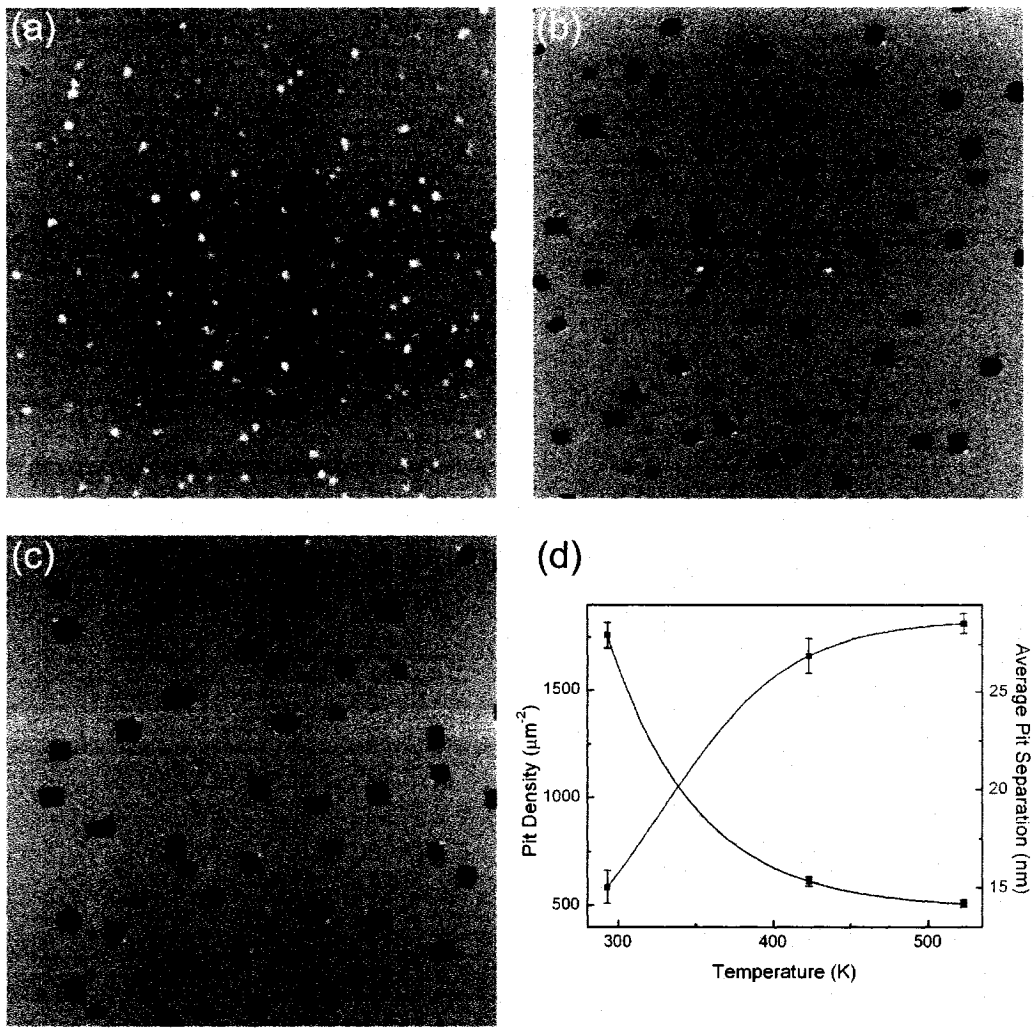

Figure 3.8: NC-AFM measurements of charge-irradiated samples (300 nm x 300 nm, dose = 0.36 ± 0.03 μC/cm^2), prepared at different temperatures: (a) 293 K (Δf = -6.6 Hz), (b) 423K (Δf = -4.3 Hz), (c) 523 K (Δf = -5.6 Hz). (d) The dependence of the pit density and average pit separation on the sample preparation temperature (the connecting lines included as a visual aid).

The protrusions on the 293 K sample were characterized by high resolution NC-AFM (see Figure 3.9). There are several notable features. First of all, it is evident that some atoms have desorbed, leaving pits in the surface. However, the pits have irregular shapes,

with only small segments of the walls aligned with the <100> directions. Inside the pits there are some small protruding atomic clusters. It is most likely that these clusters are made up of potassium atoms, remaining after the preferential desorption of bromine. Alkali enrichment is known to occur because of the non-stoichiometric character of the non-thermal desorption process [44]. At low sample temperatures, relatively few F-centers resulting from the relaxation of the primary excitations have sufficient energy to diffuse, recombine with the surface, and release thermal alkali atoms. Such *et al.* have interpreted similar protrusions at step edges and around large pits as alkali clusters, based on large-scale NC-AFM images [44]. The smallest observed pits are missing only a few atoms (Figure 3.9 (b)). It was proposed in the previous section that the smallest pits result from a single incident charge. According to this interpretation, the desorption efficiency at 293 K is significantly smaller than at higher temperatures, about 5 atoms per incident charge.

The hazy appearance of the pits/alkali clusters is indicative of the presence of additional electrostatic forces, either due to trapped charge in the region or to differences in work function between the pit area and its surroundings. A difference in the electrostatic forces over the pit and the adjacent substrate terrace was confirmed by measuring the dependence of the frequency shift on the sample voltage V_{sample} (Figure 3.9 (c)-(d)). As per equations 2.3 and 2.5, a parabolic curve is expected with the minimum electrostatic force (maximum frequency shift) at $V_{sample} = V_{CPD}$, where V_{CPD} is the contact potential difference between the sample and the AFM tip. Moreover, the contact potential difference (CPD) between two positions on the surface is given by the difference between the tip-sample CPDs at the two positions. According to the frequency shift versus voltage measurements, the frequency shift was at a maximum at -0.74 ± 0.02 V over the terrace site and -0.10 ± 0.02 V over the pit site, giving a CPD of 0.64 ± 0.04 V between the two sites. However, electrostatic forces have strong long-range components. Hence, the CPD measurements are sensitive to interactions between a mesoscopic portion of the AFM tip and the surrounding regions of the sample. This averaging effect reduces the contrast between the measurements over the nanoscopic pits and the terrace; thus, the true CPD may be larger than measured. In addition, the measurement may be affected by the

presence of charged defects near the pit. Repeated measurements over the same sites gave reproducible results. However, the CPD measured at different pit sites varied from pit to pit, ranging from -0.38 ± 0.02 V to 0.08 ± 0.02 V. This may reflect the structural differences between the pits (composition, size, geometry) or differing amounts of localized charge around the pits.

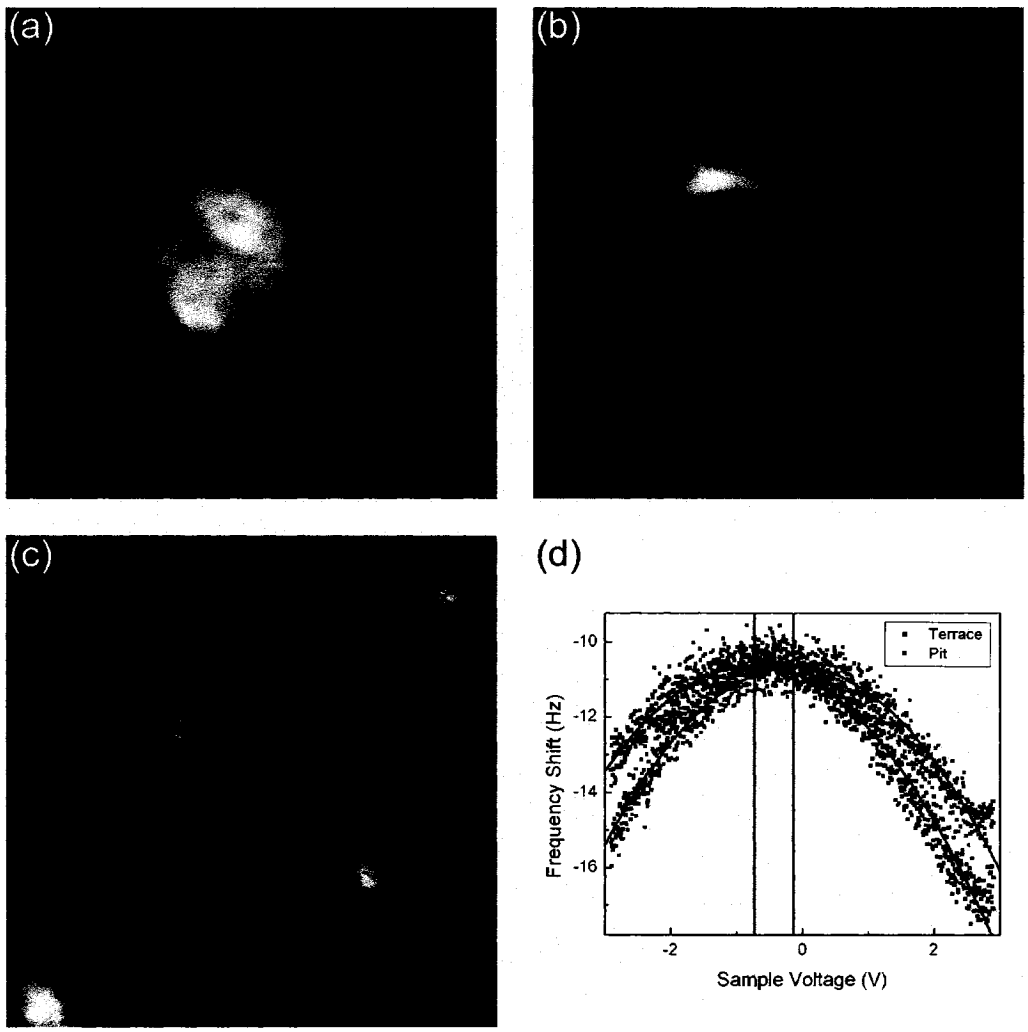

Figure 3.9: High resolution NC-AFM images of the pits created at 293 K (10 nm x 10 nm): (a) Δf = -11.0 Hz (b) Δf = -18.0 Hz; (c) 50 nm x 50 nm, Δf = -11.8 Hz; (d) Site-specific Δf versus voltage measurements showing differences in the electrostatic forces over terrace and pit sites.

3.5 Conclusions

It was demonstrated that the charge emitted from an electron beam evaporator can be used for creating pits in an alkali halide surface. One of the main advantages of this approach is the small current densities which are available, making it possible to expose the sample to a well-controlled dose of charge. The emitted charge was carefully characterized, taking into account small corrections due to secondary electron emission and electron reflection during measurement.

Using the electron-beam evaporator, arrays of nanostructured pits were created on KBr (001) surfaces, sometimes with atomic terraces extending over 1 μm. It was shown that the pit size can be controlled by varying the dose of charge and the pit density can be controlled by varying the temperature of the sample during preparation. Furthermore, a scaling behaviour of the pit size distribution, and a minimum pit size attributed to single impinging charged particles were observed. High resolution NC-AFM showed that the pits created at high temperature preserve the structure and stoichiometry of the KBr lattice and have <100> edges. Pits prepared at room temperature are less ordered, contain protrusions which are believed to be alkali atoms, and have additional electrostatic forces associated with them.

It should be noted that while this approach to pit creation is practical and well controlled, due to the complex composition of the charged beam, it is not ideally suited for studying the mechanisms of pit creation. Therefore, the above findings should be studied further with uniform sources of charge. The main utility of the e-beam technique is as a tool for surface modification.

4 Metal Growth

4.1 Introduction to Nucleation and Growth

The growth of a crystalline material on a crystalline substrate can lead to a rich variety of morphologies, including thin films [59], faceted islands [60], and fractal islands [61]. An improved understanding of the processes leading to the formation of these structures makes it possible to tune the growth parameters and create structures by design. Recent examples of this are the growth of quasi-one-dimensional structures [62], and ordered arrays of islands [63].

It is well established that on the atomic scale, a substrate is not just a passive object upon which a deposited material is placed. The substrate plays an important role in determining the nature of the growth and may impose order on the deposited material. When there is a well-defined orientation of a crystalline overlayer with the underlying crystalline substrate, the growth is referred to as *epitaxial*. The growth of a crystalline material on a crystalline substrate of the same material is called *homoepitaxy*; growth involving two different materials is *heteroepitaxy*. This chapter is concerned with the latter case.

Heteroepitaxial growth is mediated by a complex interplay between adatom-adatom[18] interactions and adatom-substrate interactions. For growth under conditions close to thermodynamic equilibrium, there are three main growth modes (Figure 4.1). *Layer-by-layer*, or *Frank-van-der-Merwe*, growth occurs when the adatoms interact more strongly with the substrate than with each other. As a result, the adatoms form a nearly complete layer before the next layer begins. *Island*, or *Vollmer-Weber*, growth takes place when the adatoms interact more strongly with each other than with the substrate. This leads to the formation of three-dimensional islands. An intermediate case, *layer-plus island*, or *Stranki-Krastanov*, growth occurs when the adatom-substrate interaction is relatively

[18] An atom adsorbed on a surface is commonly referred to as an *adatom*.

strong but the deposited layers are strained. After a certain number of layers, although some strain persists, the chemical influence of the substrate is reduced and three-dimensional islands form. It should be noted that far from equilibrium (e.g. at high deposition rates), kinetic effects become increasingly important and may cause deviations from the three near-equilibrium growth modes [64].

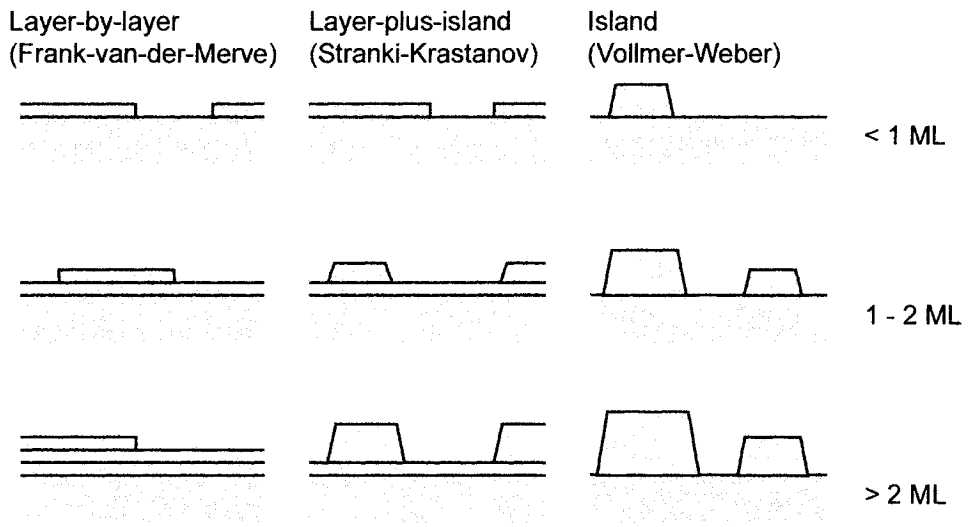

Figure 4.1: Schematic of the three near-equilibrium growth modes (after Oura *et al.* [1]).

Figure 4.2 summarizes some of the basic processes which occur following atom impingement on a surface. When an atom arrives at a surface, it may be adsorbed or reflected. The probability for adsorbtion is defined as the *sticking coefficient.* Following adsorption, the adatom typically has sufficient energy[19] to diffuse across the surface. On a periodic substrate, the surface potential seen by the adatom is corrugated, much like an egg carton. Motion along the surface occurs via random hopping between minimum energy positions. The probability of finding the diffusing species at the same position after a time t is given by [65]

[19] typically about a few tenths of an eV.

$$P = \exp(-\nu t), \tag{4.1}$$

where ν is the hopping frequency. Because hopping is a thermally activated process, ν is related to the diffusion energy barrier E_D by [1]

$$\nu = \nu_0 \exp(-E_D / k_B T), \tag{4.2}$$

where ν_0 is the attempt frequency to overcome the barrier, k_B is the Boltzmann constant, and T is the temperature.

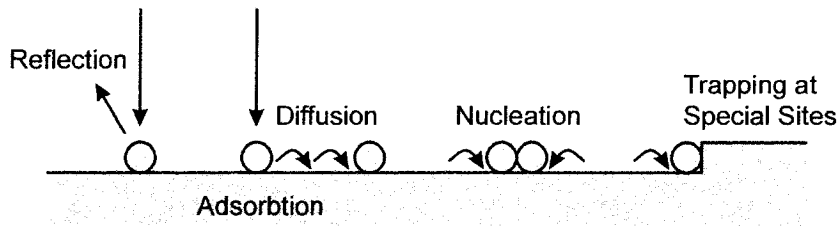

Figure 4.2: Schematic of some basic atomic processes during growth.

Atomic clusters form on the substrate via adatom trapping at special sites such as step edges or defects, or by aggregation. Small atomic clusters are often metastable and may revert back into individual atoms. The central concept in atomistic nucleation theory is that of the *critical island size*. This island size represents the minimum size where the addition of one atom creates a stable island [1, 64]. Through the balancing of rate equations, nucleation theory predicts that the number density of islands n on a surface is related to the critical cluster size i and the binding energy of the critical cluster E_i by [66]

$$n \sim \left(\frac{F}{D}\right)^{\frac{i}{i+p}} \exp\left(\frac{E_i}{(i+p)k_B T}\right), \tag{4.3}$$

where F is the deposition rate and D is the diffusion coefficient.[20] The parameter p is 2 for 2-dimensional islands and 2.5 for 3-dimensional islands [66]. For the case where dimers are stable ($i = 1$), $E_1 = 0$ [57] and the expression simplifies to

$$n \sim \left(\frac{F}{D}\right)^{\frac{1}{1+p}} = \left(\frac{4F}{\ell^2 \nu_0}\right)^{\frac{1}{1+p}} \exp\left(\frac{E_D}{(1+p)k_B T}\right). \tag{4.4}$$

Thus, for the case of $i = 1$, the diffusion energy E_D can easily be obtained by measuring the density of islands as a function of temperature.

During growth, there are four main stages [57]. In the *nucleation regime*, the islands are widely spaced and deposition mainly results in the creation of new islands. Further deposition leads to both the creation of new islands and the growth of existing islands. This is referred to as the *transition from nucleation to growth regime*. Once the island density saturates, subsequent growth leads exclusively to island expansion. In other words, the islands are sufficiently close that an adatom joins an existing island before it has time to meet with other adatoms and nucleate a new island. This is the *pure growth regime*. Finally, the *coalescence regime* is reached when adjacent islands come into contact and merge. Depending on the edge atom mobility, the merged islands may reshape to minimize energy.

Although the atomistic processes involved in growth on metals and semiconductors have been studied extensively over the last 20 years by variable temperature STM, relatively little is known about growth on insulating substrates. The first microscopic growth experiments on insulators were performed in the late 1950's by Bassett [37] using TEM.

[20] For diffusion on a square lattice, the diffusion coefficient D is related to the hopping frequency ν by $D = \ell^2 \nu / 4$, where ℓ^2 is the mean square distance of a single jump.

These studies showed that noble metals follow the island growth mode and nucleate predominantly at the step edges of alkali halides. The main interest at the time was in using the decoration effect to learn about the structure of the underlying substrate. Later TEM studies of the same system measured the nanoparticle densities, and using equation 4.4 determined the diffusion energy [67]. The critical cluster size of $i = 1$ has been confirmed recently by theoretical models [68]. Nevertheless, many discrepancies in the island densities and diffusion energies were seen between different experiments [67]. It was determined by the late 1980's that the variability was largely due to the creation of preferred nucleation sites caused by charge irradiation during deposition. A few experiments have shown greater consistency when high voltages are used to deviate charged particles. However, as demonstrated in the previous chapter, despite such precautions, there is still a sufficient amount of charge to create defects at the substrate surface. The effects of charge on growth will be addressed in Section 4.2.2.

Only a handful of UHV AFM experiments of metals on insulators have been performed to date. Measurements of gold [69] and palladium [70] on MgO have shown similar results to the TEM measurements. These experiments have also been subject to variations caused by differing sample preparation conditions, and presumably differing concentrations of defects at the surface [69]. High resolution NC-AFM has only been applied to the gold on KBr (001) system [71]. However, these measurements were primarily concerned with imaging issues. It was found that atomic resolution could not be obtained on the gold islands. This was attributed to the presence of long range electrostatic forces between the tip and island.

This chapter surveys the growth of three metals on KBr (001): gold, tantalum and palladium. The main interest is in the suitability of the growth for producing patterned structures such as electrodes on the KBr surface. Our group is currently developing the infrastructure for creating macroscopic and nanoscopic electrodes *in situ* by shadow mask deposition [72]. Because this is in essence a growth process, albeit through a patterned aperture, the fidelity of the process relies on the nature of the growth. Therefore, if the deposited material has a long diffusion length, broadened structures will be produced

[72]. Furthermore, if tall islands are produced during growth, the electrodes are likely to be discontinuous, and incapable of passing electrical currents.

4.2 Gold on KBr (001)

Gold was deposited onto a KBr (001) surface at a rate of 0.008 nm/min. Some general characteristics of the growth can be seen in Figure 4.3. Firstly, the island growth mode is followed, with some islands forming on terraces and others decorating the steps. NC-AFM provides direct evidence that the gold nanoparticles form on the top side of the steps. The same result has been inferred from TEM experiments by double-decorating the steps with two different metals [73]. Nevertheless, the reasons for nucleation at the top rather than the bottom of the steps are still not well understood. Calculations based on the repulsive, dipole-dipole, dipole-quadrupole and electrostatic potentials provide the wrong result. Therefore, it is thought that some chemical component of the interaction may be responsible for the behaviour at steps [74].

TEM measurements on the same samples showed similar structures to those seen by NC-AFM, though there are some differences. The NC-AFM measurements have the advantage that they are performed *in situ*, provide direct topographic information, and allow for accurate height determination. Nevertheless, because the particles have a smaller radius of curvature than the AFM tip radius, about 10 nm, there are significant tip convolution effects which broaden the measured lateral dimensions of the nanoparticles [2]. Furthermore, the measured shape of the nanoparticles may be distorted since the AFM tip apex is often asymmetrical. TEM provides accurate lateral dimensions, but no height information, unless difficult cross section [75] or shadowing techniques [76] are used. Moreover, there are concerns about sample integrity for the TEM measurements because the measurements are performed *ex situ* on carbon coated replicas. Clearly, the two imaging techniques are complementary, with each having its own set of advantages and limitations.

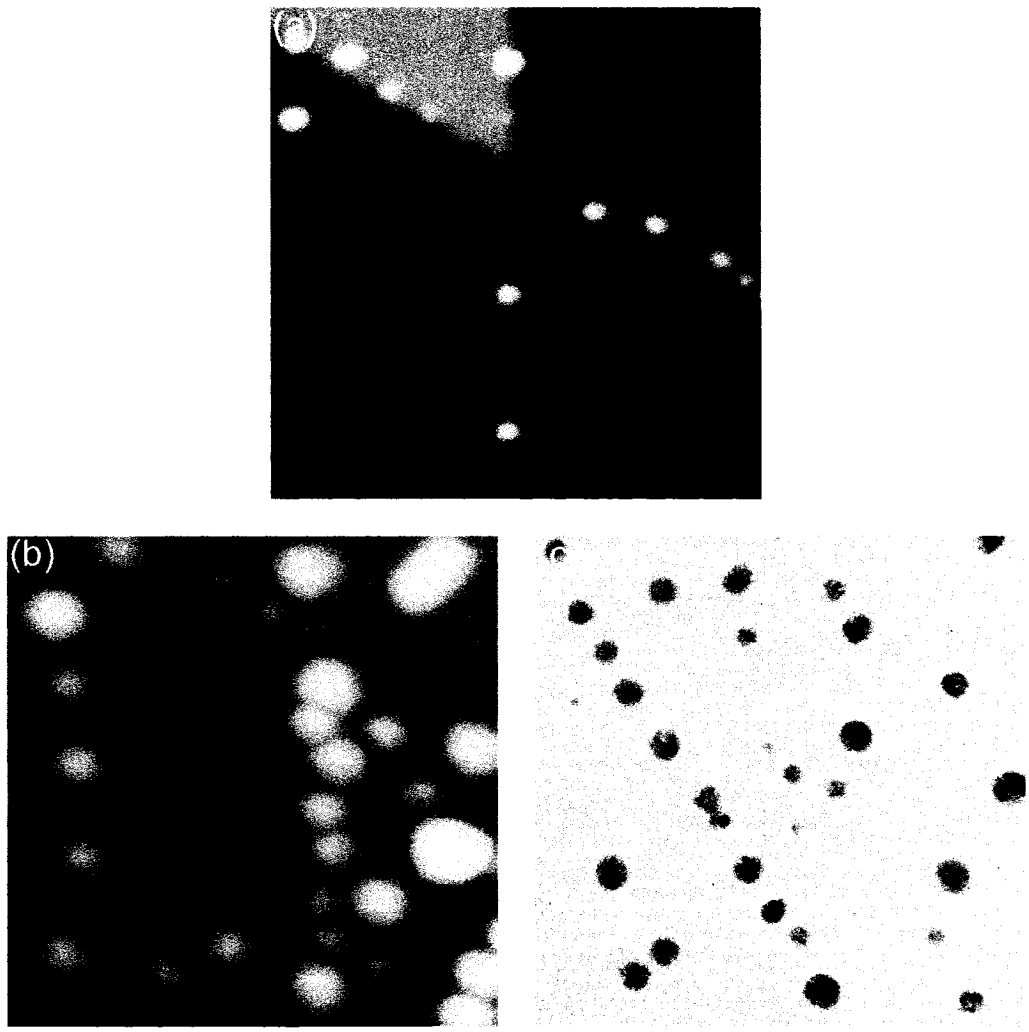

Figure 4.3: Gold on KBr (001), all images 100 nm x 100 nm: (a) 0.001 nm gold (Δf = -8.6 Hz), (b) 0.2 nm gold (Δf = -2.9 Hz), (c) 0.2 nm gold, measured by TEM.

High resolution NC-AFM measurements did not show atomic scale features. There are several reasons why this system is particularly challenging to image. First of all, there are only two reports of atomic resolution NC-AFM measurements on atomically flat metal surfaces, both showing a small atomic corrugation of 0.01 - 0.02 nm [8, 9]. In the nanoparticle system, it is not only difficult to distinguish whether there is any atomic scale corrugation (0.01 - 0.02 nm) on top of the nanometer scale (1-10 nm) nanoparticle height variations, but it is also difficult to optimize the measurement feedback so that it is

stable and responsive to both length scales. Instabilities have also been observed due to sudden tip changes, which have sometimes been associated with the disappearance of a nanoparticle from the surface. In the latter case, it is most likely that the particle is transferred to the AFM tip. In some instances, the tip changes seen during NC-AFM imaging of metal nanoparticles have caused significant changes in the tip-sample interaction, making subsequent imaging highly unstable. Tip convolution also plays a role in preventing atomic resolution. When the tip is over the side portion of a nanoparticle, the geometry is such that some parts of the tip interact with the nanoparticle, while other parts interact with the substrate, leading to a mixture of the two signals. Finally, as shown by Barth *et al.* [71], there is a contact potential difference between the gold and the KBr. Therefore, there is a significant electrostatic component in the measurements which may drown out the short range interactions. Kelvin probe microscopy [2] can potentially be used to dynamically minimize the electrostatic interactions; however, it is not clear whether the technique can be effectively applied with an insulating substrate or with sufficiently high spatial resolution.

High resolution measurements showing the crystal structure of the gold nanoparticles were obtained by TEM (Figure 4.4). Previous measurements have shown that the nanoparticles come in two main forms: multiply twinned particles (MTPs) and epitaxial particles (EPs) [74, 77]. MTPs are particles which are composed of slightly distorted tetrahedral twins. Several types are known to occur on alkali halides, including a pentagonal decahedron composed of five distorted twins, and an icosahedron composed of 20 distorted twins [78]. Figure 4.4 shows an example of a five-fold symmetric MTP. The EPs are single crystals which are oriented along the <110> directions in the case of growth on KBr (001). The presence of MTPs and EPs will be discussed further in the context of the temperature dependence of the growth (Section 4.2.2).

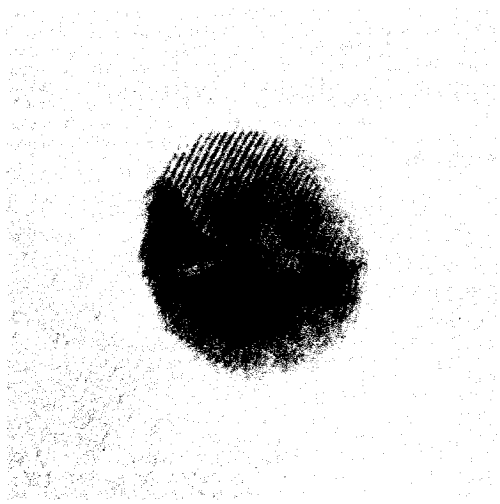

Figure 4.4: A high resolution TEM measurement showing the crystal structure of a 5-fold symmetric MTP (frame size = 15 nm x 15 nm).

4.2.1 Dependence on Coverage

Five different gold coverages were considered: 0.001 nm, 0.005 nm, 0.02 nm, 0.04 nm, and 0.2 nm. As seen in Figure 4.5, the nanoparticle number density conforms to the expected trend. At low coverages, the particle density increases with coverage as increasing numbers of particles are nucleated. At about 0.04 nm, the nanoparticle density saturates and the system enters the pure growth regime. Finally, at a coverage of 0.2 nm, there is a small decrease in density as the nanoparticles start to coalesce. It should be noted that even at the lowest measured coverage of 0.001 nm, the system is already in the transition from nucleation to growth regime. This is evidenced by the fact that, based on the particle density and coverage, the average nanoparticle consists of about 100 atoms. In the pure nucleation regime, the nanoparticles should all have the minimum stable size. For the Au/KBr system, this is a 2 atom cluster [68],i.e., a dimer. Therefore, the pure nucleation regime only exists at extremely low coverages.

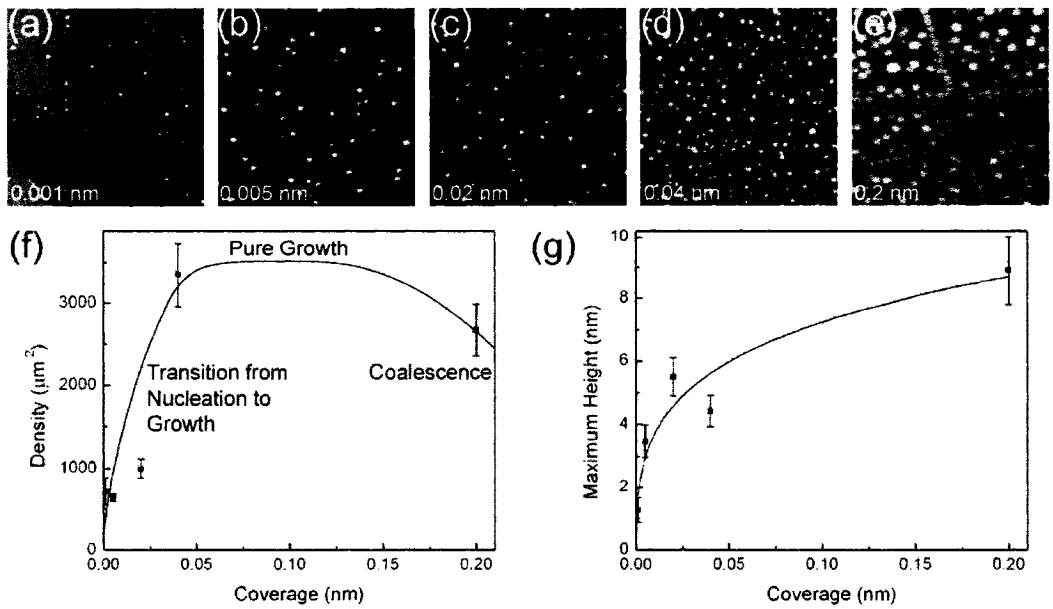

Figure 4.5: The dependence of gold growth on coverage. All NC-AFM images are 300 nm x 300 nm: (a) 0.001 nm (Δf = -6.0 Hz), (b) 0.005 nm (Δf = -4.8 Hz), (c) 0.02 nm (Δf = -4.4 Hz), (d) 0.04 nm (Δf = -26.0 Hz), (e) 0.2 nm (Δf = -2.5 Hz). The dependence of (f) nanoparticle density and (g) maximum nanoparticle height on gold coverage. The lines are included to point out the basic trends.

The maximum height of the nanoparticles was also measured and plotted as a function of coverage. As seen in Figure 4.5 (g), the maximum particle height increases steadily with coverage. The maximum height measured at a coverage of 0.2 nm is 8.9 ± 1.1 nm, which corresponds to about 38 gold layers.[21] This indicates that the gold-substrate interaction is very weak. Furthermore, it is clear that the growth of these tall discontinuous islands is not well suited for producing electrodes on a KBr surface.

[21] This estimate is based on the spacing between gold (111) planes, 0.2354 nm.

4.2.2 Dependence on Substrate Temperature

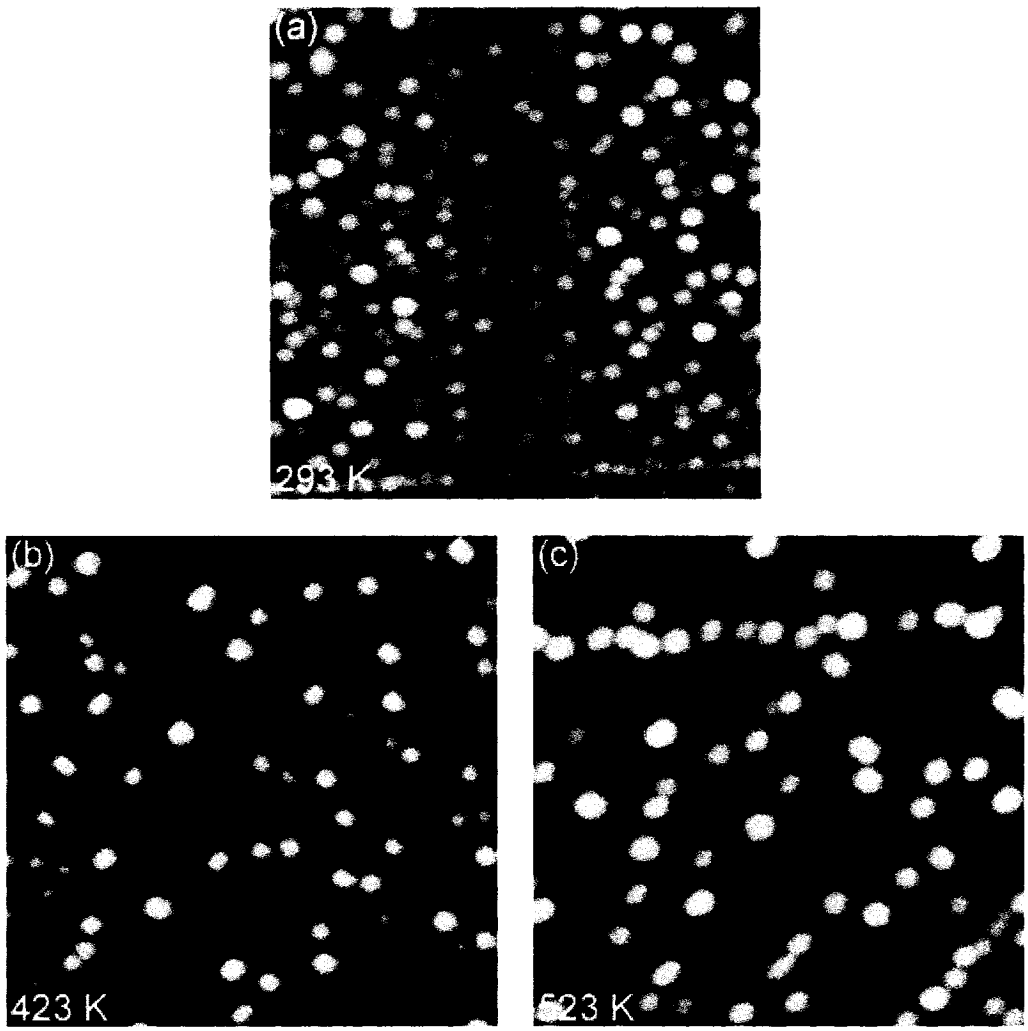

Figure 4.6: The dependence of the gold growth on sample preparation temperature. All images are 300 nm x 300 nm, 0.2 nm coverage: (a) 293 K (Δf = -3.6 Hz), (b) 423 K (Δf = -1.5 Hz), (c) 523 K (Δf = -3.9 Hz).

As the temperature is increased, the number of particles decreases and the size of the particles increases. Figure 4.6 shows samples prepared at three substrate temperatures: 293 K, 423 K, and 523 K. At higher temperatures, some rectangular particles with facets

along the <110> directions are present. The shape of the nanoparticles was confirmed by high resolution NC-AFM and *ex situ* TEM (Figure 4.7). It has been previously shown by TEM that the round particles are MTPs and the rectangular particles are EPs [74]. Moreover, the current measurements confirm the results of Yamamoto *et al.* [74] which showed that the number of EPs for gold on KBr (001) increases with temperature. The presence of some MTPs implies a very weak interaction with the substrate, since particles with similar structures can be formed in inert atmospheres, such as argon gas [79]. The height of the nanoparticles showed no dependence on temperature, with a maximum height of about 10 nm for all three temperatures.

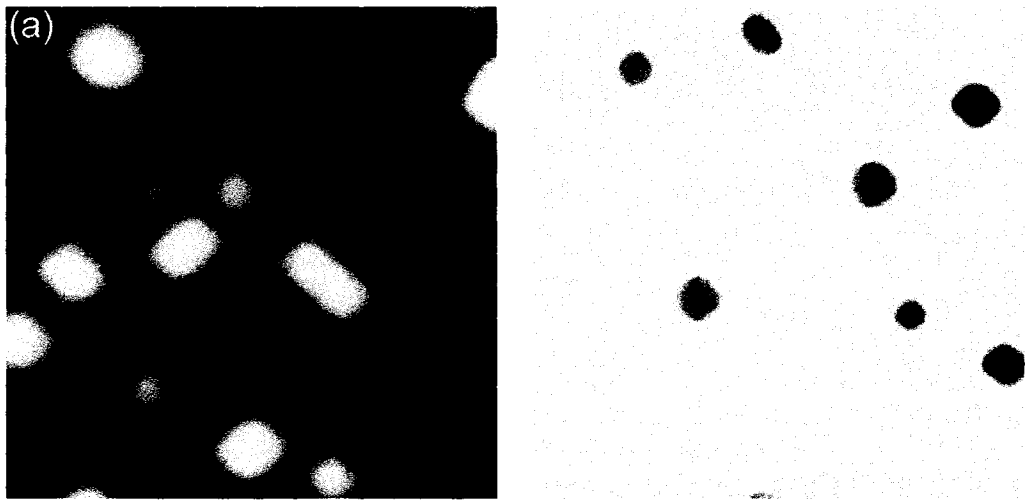

Figure 4.7: Close-up of some MTPs (round particles) and EPs (rectangular particles) seen at higher temperatures. Both images are 100 nm x 100 nm. (a) NC-AFM, sample prepared at 423 K (Δf = -2.0 Hz) (b) TEM, sample prepared at 523 K.

According to equation 4.4, for a critical cluster size i = 1, the temperature dependence of the number density can be used to determine the diffusion barrier for gold on KBr. A critical cluster size of i = 1 for gold on alkali halides is well established [66, 67]. This can be understood in terms of the large binding energy between pairs of gold atoms which is in the range of 2 - 5 times larger than the gold-substrate interaction [66]. The

relatively strong gold-gold interaction ensures the stability of two atom clusters. Figure 4.8 shows an Arrhenius plot of the nanoparticle island density. Using equation 4.4 for 3-dimensional islands, the diffusion energy for gold on KBr, E_D, was evaluated to be 0.26 ± 0.06 eV. This value for E_D corresponds well with the experimental work of Robinson and Robins [80], and the theoretical work of Chan *et al.* [81], who found E_D = 0.35 ± 0.05 eV and 0.22 eV, respectively. Other experiments produced higher results, with values of E_D ranging up to 0.78 ± 0.1 eV [82]. The small value for E_D found here is also in line with the more recent experiments, mainly performed on the gold/NaCl system, where precautions for reducing the charge impinging on the sample were used [83].

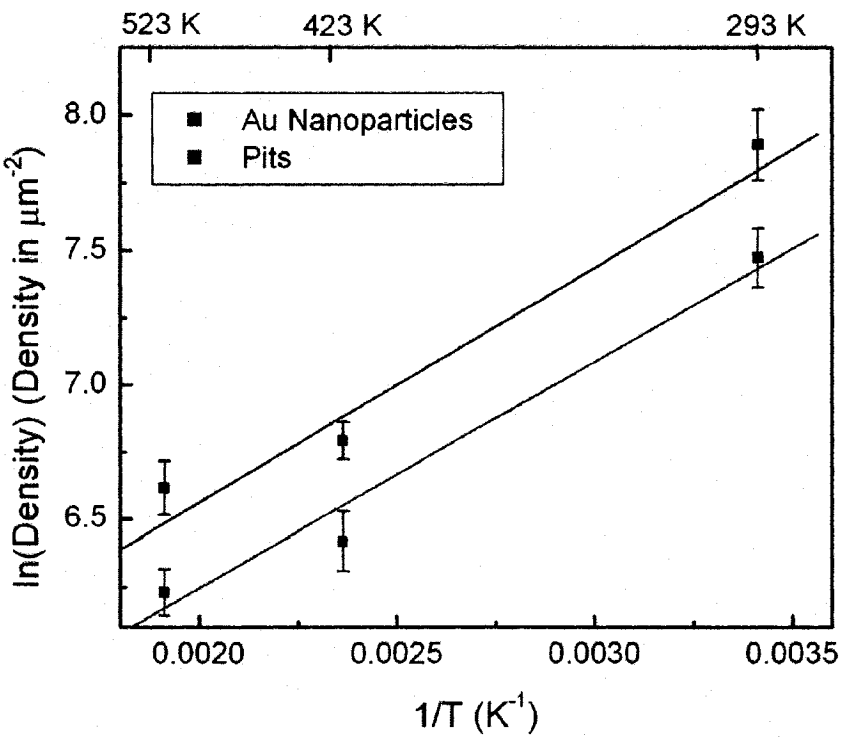

Figure 4.8: An Arrhenius plot of gold nanoparticle density (0.2 nm coverage), and pit density (dose = 0.36 ± 0.03 μ C/cm^2; the same as the dose of charge during the nanoparticle growth).

Despite the consistency with other experiments and the reasonable value obtained for E_D, it is still possible that the results are affected by the emission of charge during deposition. It was shown in Chapter 3 that even with the grid for deviating charged particles, the evaporator emits enough charge to create a large number of defects in the KBr surface. To investigate the role of defects during growth, the temperature dependence of the pit density was plotted as well. The dose of charge used to create the pits was the same as the dose of charge during the gold deposition. As seen in Figure 4.8, although the pit density is slightly smaller than the nanoparticle density, the temperature dependence is highly similar. Since there is presently no model for pit number densities, it will be assumed that the pit creation process is thermally activated.[22] The activation energy for pit creation was determined to be 0.072 ± 0.012 eV. For comparison, the activation energy for the nanoparticle system[23] is 0.075 ± 0.018 eV. These values correspond very closely and indicate that the pit creation process directs the nanoparticle growth. This also implies that the calculated diffusion energy for gold on KBr may be an upper limit, and that the obtained energy is more related to the charge-induced desorption than the metal growth. Moreover, the pit density follows characteristics which mimic those expected during island growth. This is interesting in two regards: Firstly, the creation of defects during growth plays an important role and must either be taken into account in future theoretical treatments, or avoided in future experiments by using even more stringent conditions. Secondly, the similarity between the pit creation and island growth behaviour may point to similar underlying mechanisms, for example, an important dependence on defect/atom diffusion.

The similar number density of pits and nanoparticles suggests that most of the nanoparticles are nucleated at the pits. It is natural to ask why no pits are visible in the NC-AFM images of the nanoparticles. It will be shown in Section 4.3.2 that for tantalum prepared at high temperature, the pits are visible. Furthermore, it will be shown that the nanoparticles inhibit the expansion of the pits. In the case of gold, the pits are expected to

---

[22] In other words, a temperature dependence of $n \sim \exp\left(-E/k_B T\right)$ is assumed.

[23] The activation energy associated with the nanoparticle density was calculated in the same way as the activation energy for the pits. This differs from the diffusion energy determined from equation 4.4 by a factor of 3.5.

be even smaller because gold requires a much lower evaporator power than tantalum for deposition. As a result, the dose of charge during gold evaporation is less than three times smaller than during tantalum evaporation. It was also noted in Section 3.4 that the desorption efficiency associated with the gold source is about half of that with the tantalum source. Therefore, the pits created during gold growth are expected to be more than six times smaller than those seen in Section 4.3.2, with a side length of less than 3 nm. Pits of this size are likely to be entirely covered by the gold nanoparticles. Moreover, the pits may not be visible because the gold particles are quite tall. The resulting tip convolution prevents imaging of the pits if the pit edges are near the perimeter of the particle.

4.2.3 Templated Growth on Nanostructured KBr (001)

The rectangular pits presented in Chapter 3 can also be used to intentionally template the growth of metals. Because metals are preferentially nucleated at steps, the nanoparticle nucleation occurs primarily around the pit edges. In the case of gold, this occurs on the top side of the steps. Figure 4.9 shows an example where the gold coverage was chosen such that there are only a few nanoparticles per pit. The majority of the particles are at the pit corners. Because the pit size can be controlled by varying the dose of charge, it should be possible to tune the distances between the nanoparticles. The nearest neighbour spacing between the nanoparticles shown in Figure 4.9 is about 10 nm. It will be shown in Section 5.4 that the pits can also be used to trap molecules inside the pits, between the nanoparticles. The potential use of the nanoparticles as contact pads to molecules will be discussed.

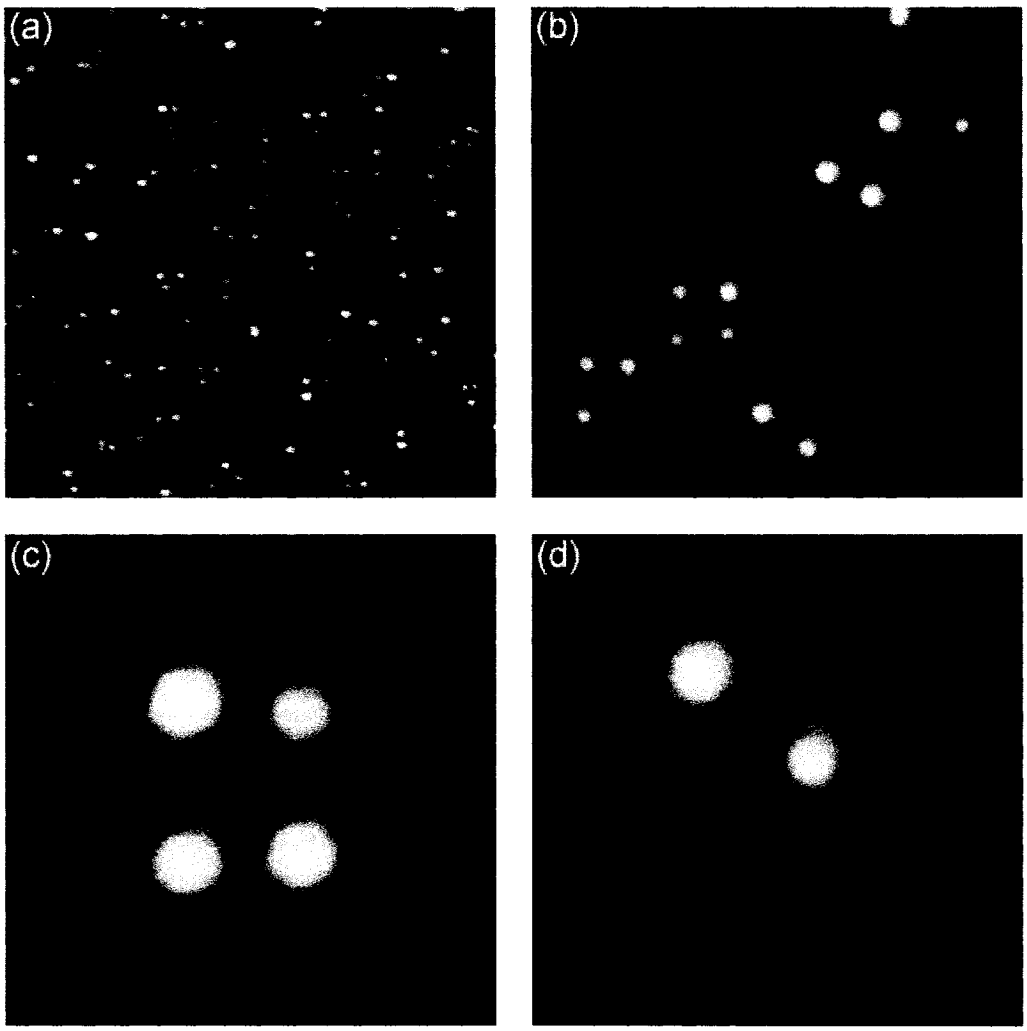

Figure 4.9: Gold nanoparticles nucleated around rectangular monatomic depth pits: (a) 300 nm x 300 nm (Δf = -3.0 Hz), (b) 100 nm x 100 nm (Δf = -4.2 Hz), (c) 40 nm x 40 nm (Δf = -5.9 Hz), (d) 40 nm x 40 nm (Δf = -5.4 Hz).

4.3 Tantalum on KBr (001)

Although tantalum is less commonly studied than gold, the growth of thin tantalum films has been studied extensively, especially for microelectronics applications [84]. Tantalum was also selected because its bulk lattice constant is 0.33 nm, which is precisely half of the KBr lattice constant. It was thought that the close lattice matching may allow for epitaxial growth; however as shown in the following sections, this is not the case.[24]

4.3.1 Dependence on Coverage

Two tantalum coverages were considered, 0.2 nm and 0.6 nm. A deposition rate of 0.008 nm/min was used, the same rate used in the gold experiments. As seen in Figure 4.10, this system follows the island growth mode. However, the island shapes show branching. These types of structures are referred to as *dendritic* if the branches are symmetrically arranged, and *fractal* if the structures are randomly ramified [61]. Based on these definitions, the tantalum islands are fractal. This type of growth is common under conditions where the substrate temperature is less than about 15 % of the melting temperature of the metal [64]. For the case of tantalum, the substrate temperature of 293 K represents 8.9 % of the melting temperature. Under these conditions, the diffusion of the tantalum atoms along the island edges is slow. As a result, an atom joining the island only samples a short length of the island perimeter before settling at a local energy minimum. The branching occurs because any protruding parts of the island block other parts, making them less accessible. Atoms arriving at random are then more likely to attach to the protruding structures than to find their way into the interstices. Moreover, the atom cannot diffuse far enough to move into and fill the interstices. The idealized case, where there is no edge diffusion at all, is referred to as the *diffusion limited aggregation model*. The atom sticks to the island wherever it lands, resulting in one atom

---

[24] A metal with a lattice constant matching the sublattice unit cell of the substrate, $0.66/\sqrt{2}$, would be a better candidate for epitaxy, since this would allow each metal atom to sit atop the same ionic species of the substrate. Unfortunately, there are no metals which match this condition. This type of epitaxy may be possible with an alloy or a different ionic crystal substrate.

wide branching structures. In real growth, the branch width can be considerably wider, depending on the amount of edge diffusion [1].

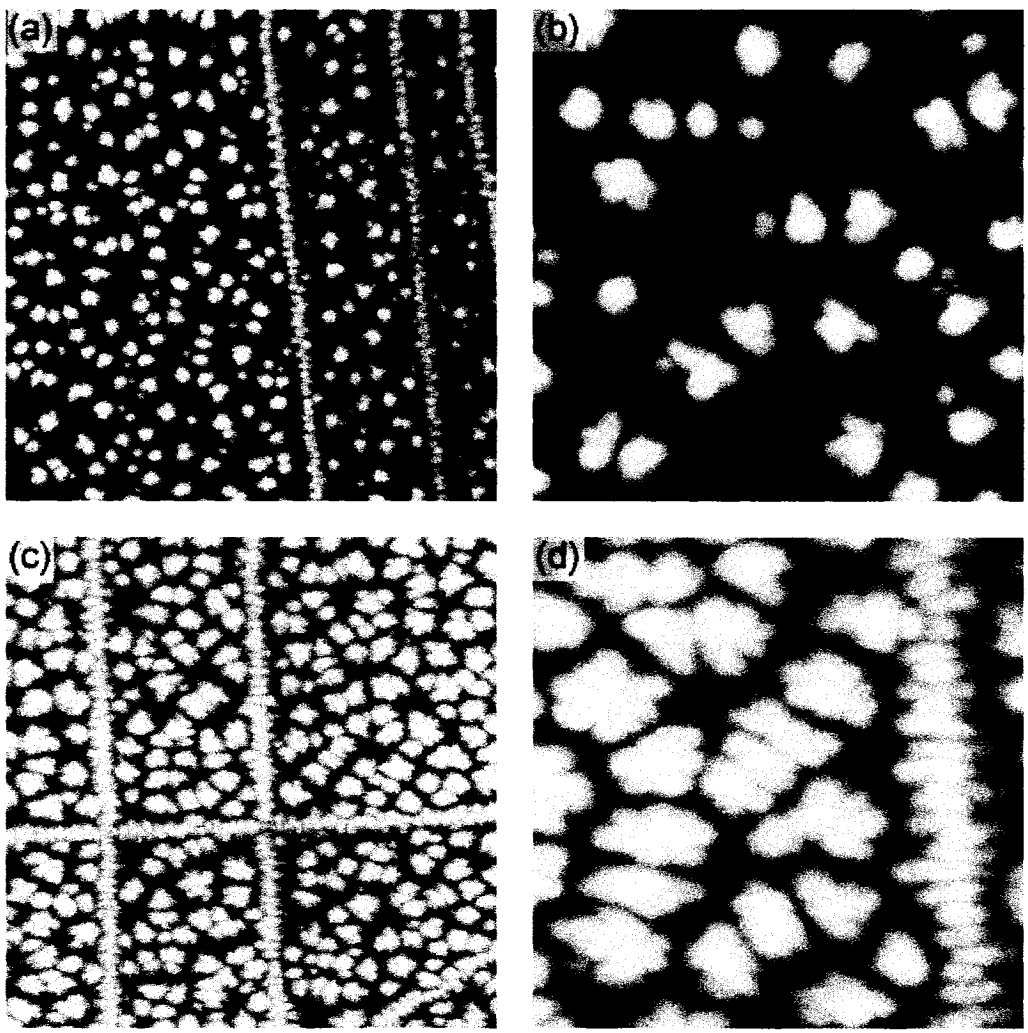

Figure 4.10: Tantalum on KBr (001) at a coverage of 0.2 nm (a) 300 nm x 300 nm (Δf = -4.0 Hz), (b) 100 nm x 100 nm (Δf = -4.5 Hz); and a coverage of 0.6 nm (c) 300 nm x 300 nm (Δf = -4.7 Hz), (d) 100 nm x 100 nm (Δf = -3.9 Hz).

The maximum height of the tantalum nanoparticles for a coverage of 0.2 nm is 3.1 ± 0.3 nm, which is considerably smaller than the maximum height of 8.9 ± 1.1 nm for gold nanoparticles at the same coverage. This shows that tantalum interacts more strongly with KBr than gold. In a theoretical study of the adsorption of three noble metals on NaCl, it was shown by *ab initio* methods that the interaction is mainly electrostatic and weak [85]. This is largely because of the full valence *d* orbitals present in the noble metals. It was suggested that metals which do not have completely filled valence *d* orbitals would be able to bond with the substrate via mixing between the surface *p* band and the metal *d* orbitals. Furthermore, the absence of a closed valence orbital would lead to a reduction in the Pauli repulsion between the metal atom and the surface ions, and allow for greater orbital overlap. Since tantalum has only 3 electrons in its 5*d* orbital, it is likely that there is a chemical component to its bonding with the substrate. At a higher tantalum coverage of 0.6 nm, the height increases by only a small amount to 3.5 ± 0.4 nm. These measurements show that it should be possible to grow a thin tantalum film on KBr with a thickness of only a few nanometers.

In addition, as seen in Figure 4.10, the tantalum interacts strongly with the KBr steps, leading to extensive step decoration. The nanoparticles spread out across the steps. Moreover, the structures sometimes have a staggered positioning, providing evidence for nucleation at both the top and bottom side. The resulting linear arrays of nanoparticles appear to form nanowires; however, careful inspection of TEM measurements (Figure 4.11) shows that there are small gaps between some of the nanoparticles. The apparent connectivity seen in the NC-AFM measurements is due to tip convolution.

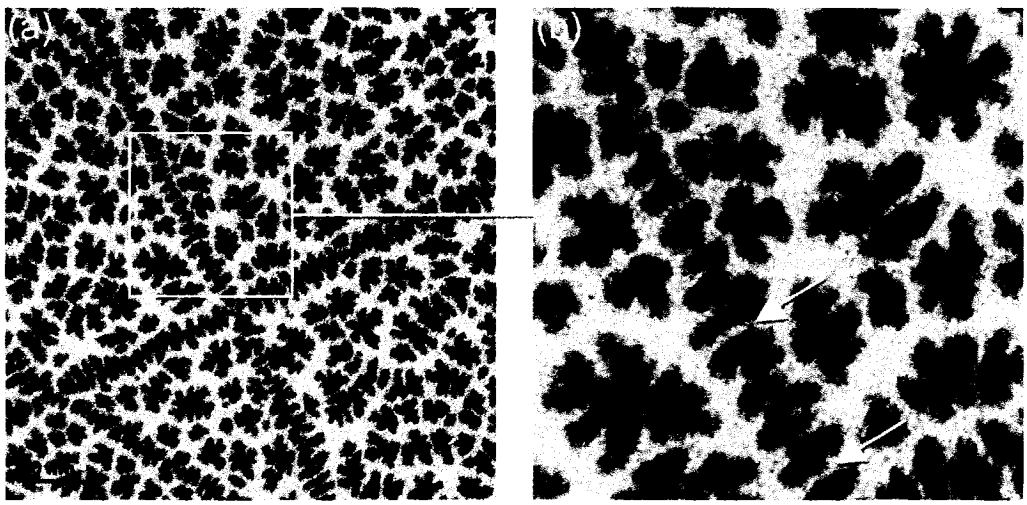

Figure 4.11: Tantallum on KBr (001), at a coverage of 0.6 nm, measured by TEM: (a) 300 nm x 300 nm, (b) 100 nm x 100 nm. The arrows point to gaps between nanoparticles nucleated at a step.

4.3.2 Dependence on Substrate Temperature

Samples prepared at an elevated temperature, 523K, produced tantalum nanoparticles which sit inside rectangular pits. An exception to this is found near atomic steps, where some tantalum particles are not in pits. Instead the steps recede away from the particles. This provides some information about the kinetics: the tantalum nucleates at the KBr steps before most of the surface desorption takes place. This is visible in Figure 4.12 (b) where the tantalum nanoparticles initially decorated a rounded step, which later became modified, favouring <100> directions.

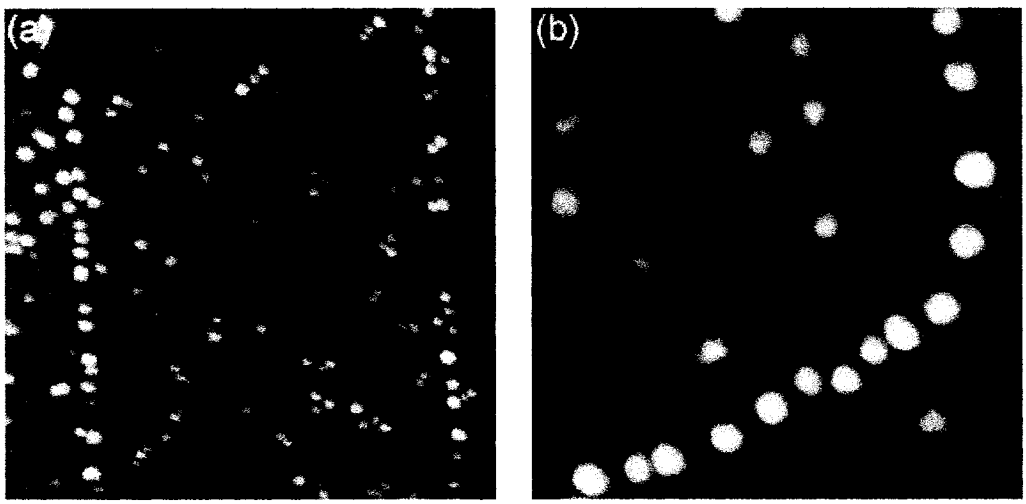

Figure 4.12: Tantalum nanostructures inside monatomic depth pits, prepared at a substrate temperature of 523 K: (a) 300 nm x 300 nm (Δf = -1.0 Hz), (b) 100 nm x 100 nm (Δf = -5.0 Hz).

In comparison with the samples prepared at room temperature, there is a lower density of particles and the particles are smaller. This may be caused by a lowered sticking coefficient for tantalum at higher temperatures. An intriguing possibility is that the tantalum chemically reacts with the bromine after it is desorbed by the incident charge during deposition. Tantalum and bromine spontaneously react at room temperature to form tantalum bromide compounds, the most common form being $TaBr_5$ [86]. This compound has a melting point of 538 K and is expected to be highly volatile at the sample preparation temperature of 523 K. As a result, if this compound does form, it would readily desorb from the surface, thereby reducing the size of the tantalum particles. It should be noted that the tantalum cannot react directly with the KBr substrate to form $TaBr_5$. The energy cost to dissociate a KBr molecule far exceeds that released by the synthesis of a tantalum compound [87]. As a direct demonstration, an experiment was performed where tantalum was deposited onto KBr at room temperature. Subsequent heating of the substrate to temperatures as high as 773 K failed to produce any pits or changes in the size of the tantalum particles.

The pits surrounding the tantalum are markedly smaller than the large pits shown in Section 3.3, despite the use of the same dose of charge. The mean area of the pits[25] containing the tantalum nanoparticles is 48 ± 2 nm^2, corresponding to a mean side length of 6.9 ± 1.4 nm. This small pit size reflects a reduction in the desorption efficiency to 17 ± 2 atoms per |e|. This is nearly half of that for the pits without tantalum structures inside. Generally, after the initial desorption of a surface atom, predominantly at kink sites [7, 43], an unzipping process is initiated along a step. In the case under consideration here, the unzipping may be interrupted by the presence of metal nanoparticles which physically obstruct the process.

The pit size distribution, shown in Figure 4.13, is quite sharply defined; however, there is a large tail at higher areas due to clustering and coalescence. The density of pits is 930 ± 70 / μm^2, which is nearly double that of samples without the metal structures (see Table 3.1). This indicates that the metal particles act as nucleation sites for the growth of the pits. Since the converse situation, the nucleation of metal particles at defect sites, is also known to occur (seen in Section 4.2.2 and [88, 89]), it is likely that both processes take place simultaneously. This also explains why the tantalum nanoparticles are often clustered in groups. After a pit expands around a nanoparticle, a new nanoparticle may nucleate along the pit edge.

[25] The area of the pits was taken to include the entire interior area, including the areas covered with tantalum.

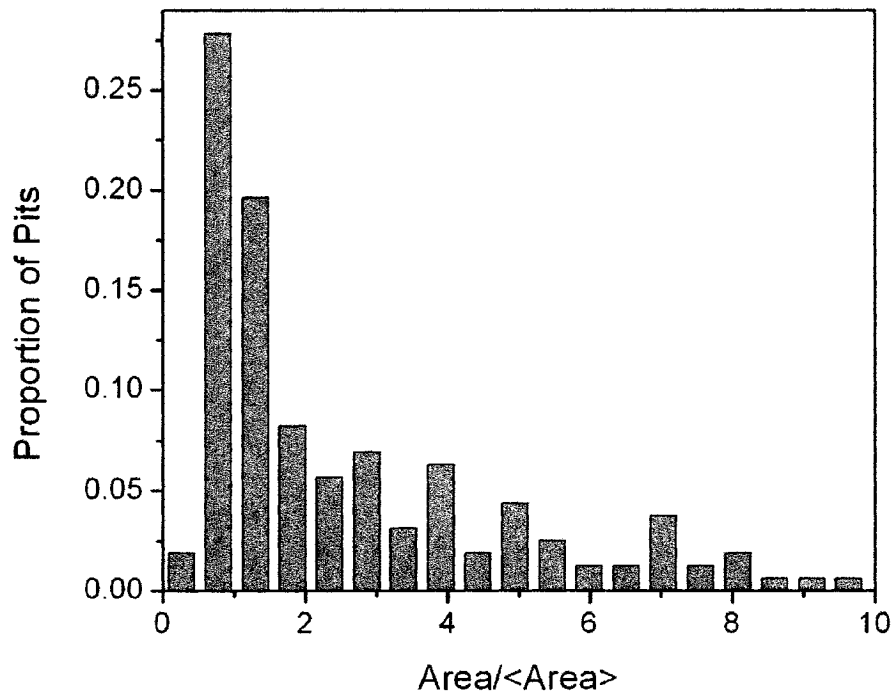

Figure 4.13: The size distribution of the pits surrounding the tantalum nanoparticles. The mean pit area is 48 ± 2 nm^2.

4.4 Palladium on KBr (001)

Palladium was chosen because it has some interesting properties which make it appealing for molecular electronics studies. It is well established that the electrode-molecule interface plays an important role in determining the electrical characteristics of molecule-based devices [19, 20]. Palladium has been shown to produce good ohmic contacts with carbon nanotubes [90]. Moreover, the electrode work function can be modified by exposing the system to hydrogen [90]. The tuneability of the work function may be used to further investigate the nature of metal-molecule contacts and potentially to facilitate transport by aligning the electrode work function with the molecular energy levels. There is also considerable interest in supported palladium nanostructures for catalysis [91].

Palladium was deposited onto KBr (001) surfaces at a rate of 0.008 nm/min. Figure 4.14 shows the growth at two coverages, 0.04 nm and 0.2 nm. In addition to the palladium nanoparticles, there are two other notable structures: flat islands with <100> edges, and gradually protruding areas. High resolution measurements of the flat islands (Figure 4.15) show that they have the same lattice constant as the KBr substrate and the expected height of a KBr layer. Thus, the square edged flat islands can be identified as KBr islands. The gradually protruding distortion in the KBr surface may be caused by palladium which interdiffuses under the KBr surface. Moreover, this may be what leads to the formation of the flat KBr islands. If enough palladium becomes embedded underneath the surface, the KBr lattice will be distorted and potentially displaced to the point where islands form at the surface. The gradually protruding areas would then represent an intermediate stage in the KBr island formation, where there is some lattice distortion, but not enough yet to produce an island. This is supported by the observation that the gradual protrusions have heights which range from 0.1 nm to 0.3 nm. These heights are similar to, but smaller than the KBr step height of 0.33 nm.

The high resolution images shown in Figure 4.15 also show some protruding structures on top of the KBr islands. These appear to have the lattice constant of KBr. In the case of Figure 4.15 (d), the height of the protrusion is about 1 nm. This may indicate that it is a palladium nanoparticle which is coated with KBr. This interpretation is consistent with the previous observation that the palladium may embed itself under the KBr surface. Finally, some of the protrusions show alignment with the <110> directions. One example is shown in Figure 4.15 (d). This may be an epitaxial palladium nanoparticle, similar to those seen with gold on KBr (001).

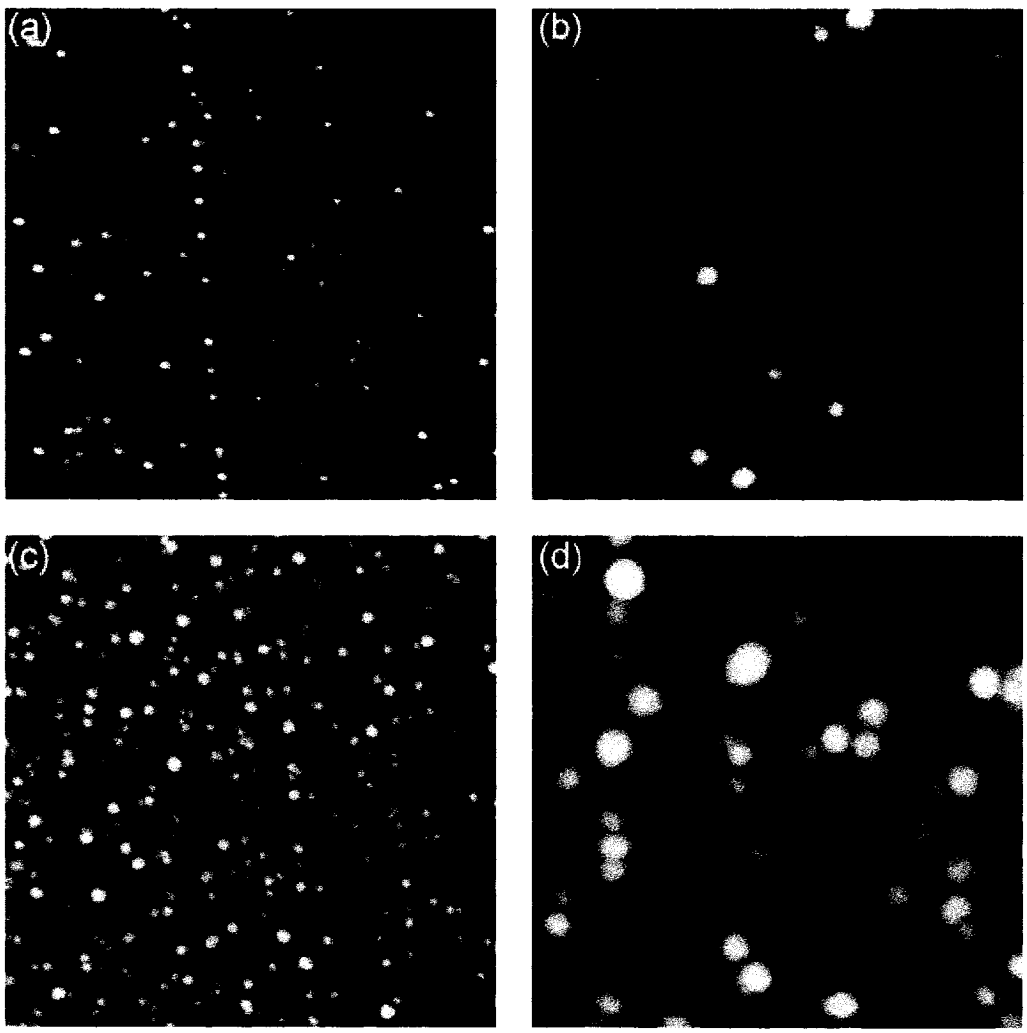

Figure 4.14: Palladium on KBr (001) at a coverage of 0.04 nm (a) 300 nm x 300 nm (Δf = -3.6 Hz), (b) 100 nm x 100 nm (Δf = -4.0 Hz); and a coverage of 0.2 nm (c) 300 nm x 300 nm (Δf = -4.6 Hz), (d) 100 nm x 100 nm (Δf = -4.3 Hz).

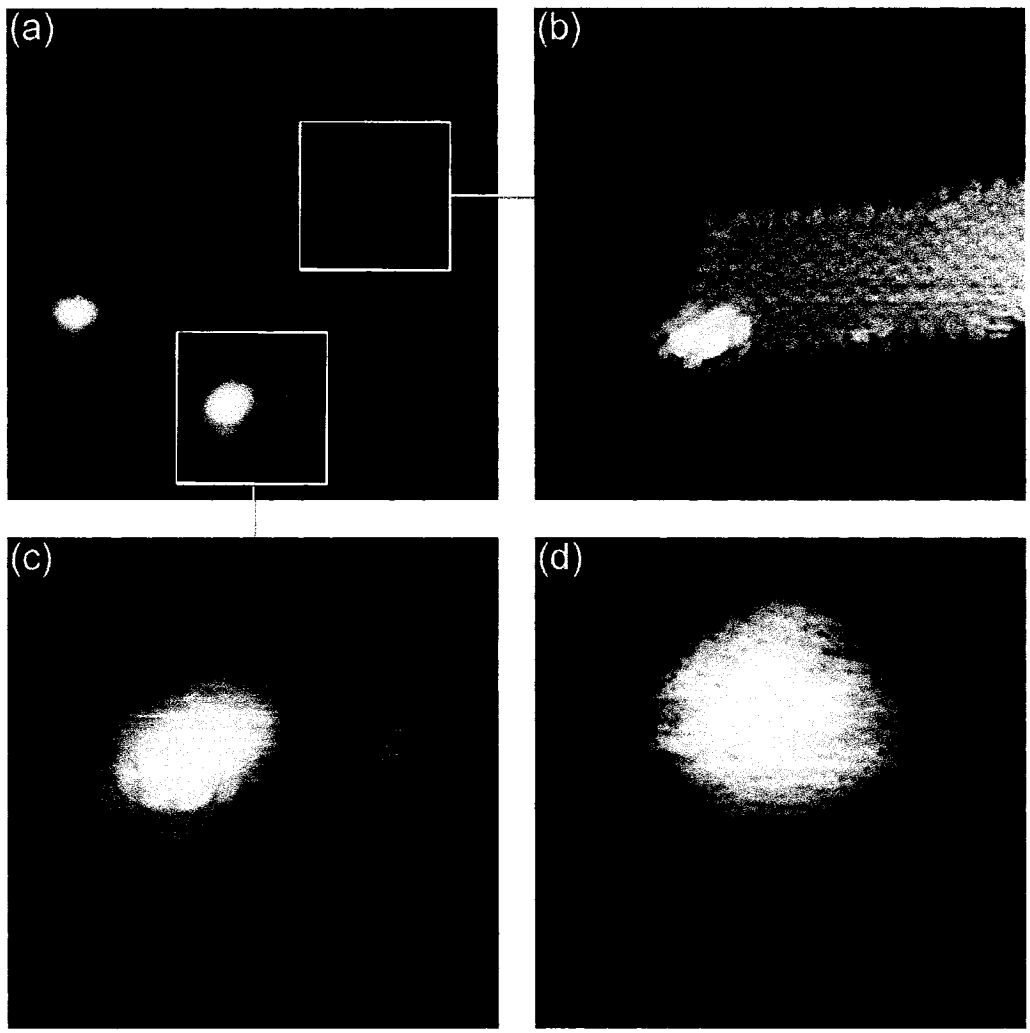

Figure 4.15: High resolution NC-AFM images of the palladium nanoparticles and the flat <100> faceted islands (a) 40 nm x 40 nm (Δf = -2.4 Hz), (b) 12 nm x 12 nm (Δf = -2.9 Hz), (c) 12 nm x 12 nm (Δf = -2.0 Hz), (d) 4.5 nm x 4.5 nm (Δf = -9.0 Hz).

4.5 Conclusions

The growth of gold, tantalum, and palladium on a KBr (001) surface was considered. Gold forms tall islands, with the height of the islands increasing with coverage. The number density of nanoparticles follows the expected dependence on coverage, with the density increasing, saturating, and then gradually decreasing as the system goes from

nucleation and growth, to pure growth, to coalescence regimes. At higher temperatures, an increasing number of <110> oriented rectangular epitaxial nanoparticles is observed. In agreement with previous TEM experiments and modeling, a diffusion barrier energy of 0.26 ± 0.06 eV for gold migration on KBr was determined. However, it was shown that the pit creation followed a very similar temperature dependence. This suggests that despite the use of a charge-deviating grid, there is a sufficient number of pits created during metal growth to control the growth characteristics. These same defects can be intentionally used to template the growth of metals. When gold is deposited on a pitted KBr surface, the gold is nucleated around the pit edges, mainly at the corners.

Tantalum grows as ramified islands. These are flatter than the gold islands, indicating a stronger interaction with the KBr substrate. There is extensive decoration of the substrate steps, leading to nanowire-like structures. However, TEM measurements show that there are some narrow discontinuities which are not seen with NC-AFM because of tip convolution. Growth at 423 K leads to smaller nanoparticles which are surrounded by rectangular pits in the substrate. The small size of the pits reflects a low desorption efficiency and provides evidence that the nanoparticles obstruct the desorption process. The number density of pits is nearly double the amount seen in pitted KBr samples without nanoparticles. This provides evidence that the nanoparticles nucleate the pits. The measurements also show that the metals are nucleated by surface defects such as steps. Therefore, the resulting picture of growth and pit creation is complex, with each process having an influence on the other. It is expected that this is what leads to the clustering of some nanoparticles: after a pit surrounds a nanoparticle, a new nanoparticle may nucleate at the newly formed step.

Some unexpected behaviour was observed in the growth of palladium on KBr. In addition to palladium nanoparticles, some rectangular KBr islands were created. It is suspected that these islands form as a result of lattice distortions which are caused by the diffusion of some palladium below the KBr surface. This is supported by the observation of some gradual protrusions with heights which are similar to, but smaller than the KBr step

height. These protrusions are thought to represent intermediate stages in the KBr island formation.

In terms of constructing electrodes on a KBr surface, the best candidate of the three metals is tantalum. The tantalum produced relatively flat islands and it is expected that thin films, with a thickness of a few nanometers, can be produced. Moreover, it should be possible to produce nanowires by evaporating tantalum onto KBr through a shadow mask. On the other hand, the gold produced tall, isolated islands which are not well suited for making continuous structures on the nanometer scale. Palladium was not a good candidate because of its damaging effect on the substrate.

5 Templated Growth of Molecules

5.1 Introduction to Molecular Growth

The prospect of using organic materials as active components in electronic and optoelectronic devices [92, 93] has sparked great interest in the growth of molecular adlayers on solid substrates [94]. In particular, molecules with conjugated bonds (alternating single and double bonds) are thought to be of importance for molecule-based electronics by virtue of their delocalized electronic structures. Because the structural quality of an organic film plays a critical role in determining its transport properties [95], an understanding of the processes governing the ordering of molecular crystals is of utmost importance. Molecular nanostructures are particularly promising for organic electronics because of the possibility of circumventing the problems imposed by grain boundaries [96], and the potential for interesting size effects [14].

As shown in Chapter 4, metal-on-insulator growth can lead to a variety of shapes and structures in the deposited film. The situation for molecular growth is even more complex. First of all, the fact that molecules have extended structures, often with some anisotropy, means that the orientation of the molecule is important. Furthermore, in the case of unsubstituted aromatic molecules, the molecule-molecule and molecule-substrate interactions are typically weak van der Waals and electrostatic (multipolar) type interactions. As a result, polymorphism, the existence of multiple configurations with similar lattice energies, is common [94]. The "soft" interactions between the molecules also enable the growth of highly strained films. Finally, the unit cell of the molecular lattice is generally much larger than the substrate lattice and typically has low symmetry, making commensurism more often the exception than the rule [97]. Most commonly, the overlayer energy is minimized by a "coincident" structure, where the larger overlayer lattice only meshes with the substrate lattice at certain intervals.

In the experiments reported here, two molecules were considered: 3,4,9,10-perylenetetracarboxylic dianhydride (PTCDA), and C_{60}. The structures of these molecules are shown in Figure 5.1. Both of the molecules have long been considered archetypes for organic electronics because of their extended π-systems and their ability to grow in a well ordered fashion on a wide range of substrates [94, 98]. The planar molecule, PTCDA, typically grows with the molecules lying flat on the substrate surface in a herringbone arrangement (Figure 5.1 (b)), forming stacks of 2-dimensional sheets. The interlocking herringbone structure corresponds closely to the (102) plane of the two known bulk polymorphs (termed α and β) [99] and is a result of the electrostatic interactions between the quadropole moments of the molecules.[26] Other arrangements have also been observed in thin films, depending on the overlayer-substrate interaction strength and lattice registry [100, 101]. C_{60}, also known as *buckminsterfullerene*, consists of a nearly spherical arrangement of 60 carbon atoms (Figure 5.1 (c)). The hollow carbon cage is made up of 20 hexagons and 12 pentagons, resembling a soccer ball or the geodesic domes of architect Buckminster Fuller. When grown in thin films, C_{60} generally crystallizes in a hexagonal structure, much like the (111) plane of the van der Waals bonded face-centered cubic bulk crystals [102]. However, in some cases, some molecules have different measured heights, either due to electronic effects such as charge transfer, or due to strong interactions with the substrate which induce local restructuring of the substrate [102]. The orientation of the molecules in the first layer depends on the substrate and sometimes on the particular site at which the molecule sits [103, 104]. On moderately interacting substrates, such as noble metals, the first layer molecules can slowly rotate at room temperature (~10^{-3} Hz) [105]. Generally, the molecules in the second layer and beyond rotate freely at a frequency of about 10^{10} Hz at room temperature, as in the bulk crystal [105, 106].

[26] The oxygen groups of the molecule are negatively charged and the adjoining sides are positively charged.

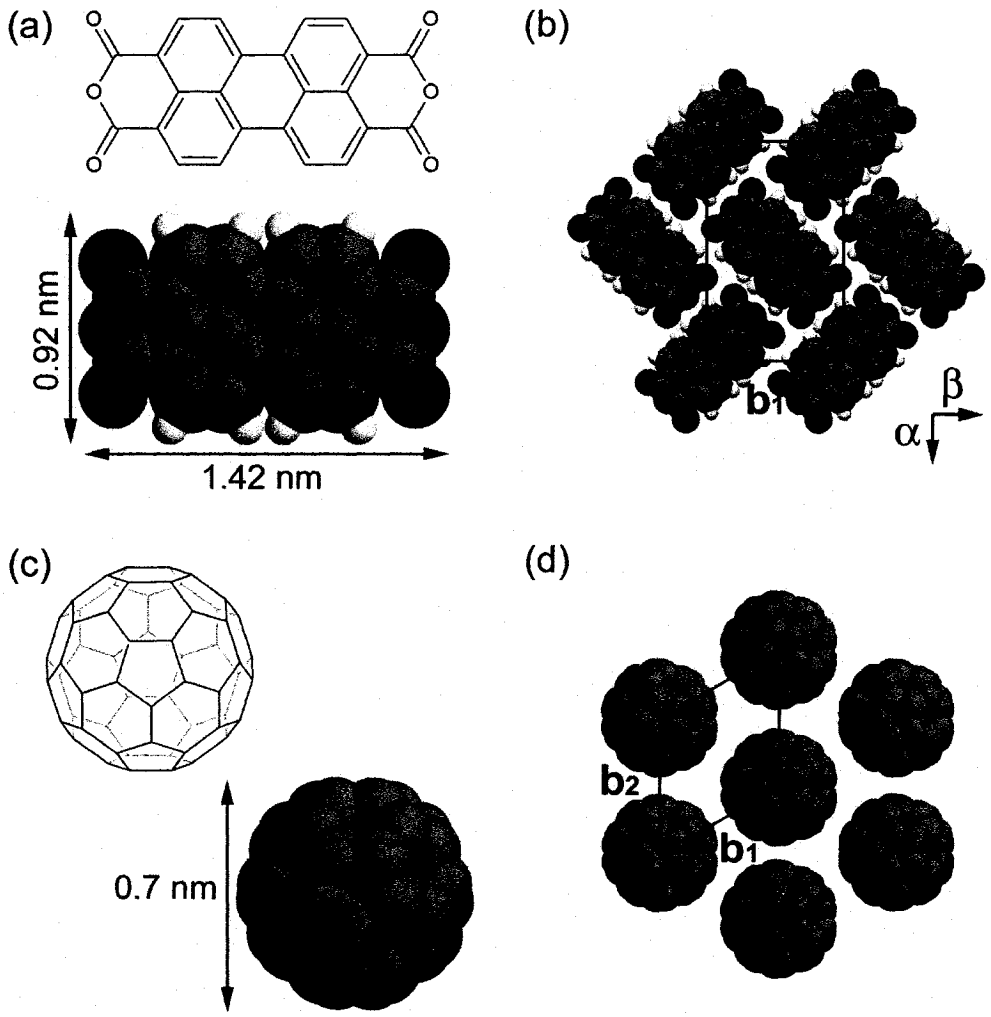

Figure 5.1: (a) Chemical structure and space-filling model of 3,4,9,10-perylenetetracarboxylic dianhydride (PTCDA), with dimensions. (b) Schematic of the PTCDA (102) plane with unit cell. The two bulk structures, the α-phase (b_1 = 1.196 nm, b_2 = 1.991 nm) and β-phase (b_1 = 1.245 nm, b_2 = 1.930 nm) differ in the direction of the offset between layers [99]. (c) Chemical structure and space filling model of C_{60}, with dimensions. (d) Schematic of a close-packed C_{60} layer. In bulk C_{60} crystals, $b_1 = b_2$ = 1.02 nm [107].

Scanning tunnelling microscopy and electron-based surface science techniques have greatly improved our understanding of the growth of PTCDA [100, 101, 108, 109], C_{60} [98, 103-105], and other molecules on conducting substrates [102, 110]; however, little is known about the growth of molecules on insulators. In the context of organic electronics, an insulating substrate is important for the construction of electrically isolated components. With the development of NC-AFM, the high resolution characterization of growth on insulators has recently become accessible. Nevertheless, there are still only a few examples with molecular resolution, including PTCDA on KBr [111], C_{60} on KBr [112], and vinylidene fluoride oligomers on KCl [113].

A general finding in the growth of medium sized molecules (< 100 atoms) on insulating substrates is that the molecules diffuse over long distances and nucleate primarily at step edges [112, 114]. Figure 5.2 shows NC-AFM images of PTCDA and C_{60} grown on a KBr (001) surface. Both molecules follow the island (Vollmer-Weber) growth mode. The PTCDA islands are compact and mainly form at the bottom of steps, while the C_{60} islands form complex branching structures which span across steps. It is thought that this difference reflects the different chemical interactions and geometry at play. In addition to the weak nonspecific van der Walls interactions, there are local electrostatic interactions between the quadropole moment of the PTCDA and the ionic surface. Furthermore, the PTCDA has a height of 0.32 nm [115] which is very similar to that of the KBr steps (0.33 nm). This facilitates the interaction between the molecules at the bottom of a step with the step ions and allows the PTCDA to have a higher coordination than on top of the step. Conversely, the C_{60} mainly experiences weak non-specific interactions with the substrate and is considerably taller than the KBr step (0.7 nm vs. 0.33 nm). Thus, the molecules do not notice a large difference between the coordination at the top and bottom of a step. The intriguing shapes of the C_{60} islands are the subject of further study in our group. High resolution NC-AFM measurements of the islands have shown the expected lattice structures for PTCDA [111] and C_{60} [112] films. In the C_{60} on KBr (001) system, simultaneous measurement of the substrate and overlayer lattice made it possible to measure an 8x3 coincident structure for a C_{60} island pinned at a (001) step [112]. The unit

cell has 4 molecules in registry with the substrate and 14 molecules which are not in registry.

In this chapter, two approaches to modifying the growth of molecules will be presented: (1) The use of nanostructured pits for trapping molecules, and (2) the use of metals for directing the growth of molecules.

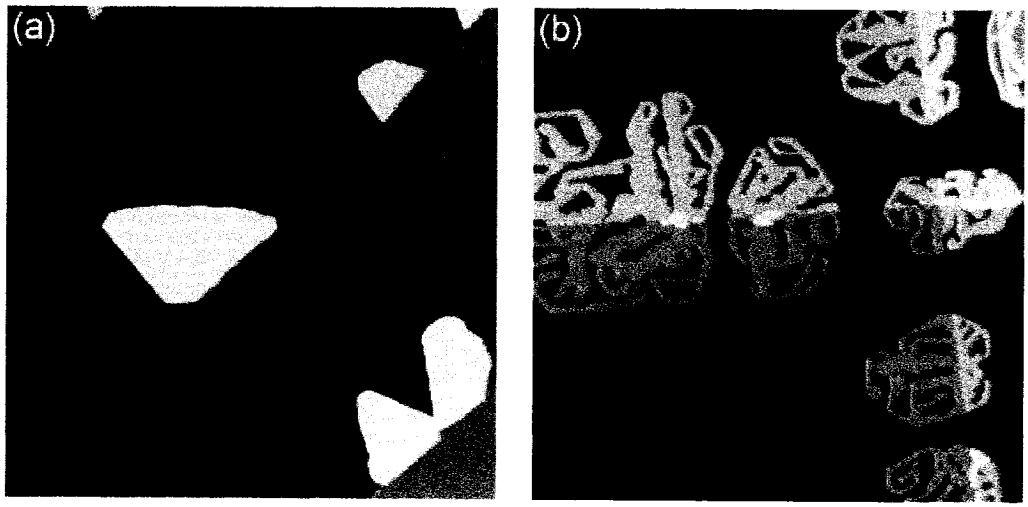

Figure 5.2: Overview NC-AFM images (1 μ m x 1 μ m) of (a) 0.4 ML PTCDA (Δf = -2.3 Hz) and (b) 0.5 ML C_{60} (Δf = -6.6 Hz) grown on a KBr (001) surface [(a) provided by S. Burke].

5.2 Molecules in Nanostructured Pits

One means of immobilizing molecules, first demonstrated by Nony *et al.* [114], is to use monolayer deep rectangular pits in an alkali halide surface as molecular traps. The size and shape of the resulting molecular nanostructures are determined by the dimensions of the pits which act as templates. Trapping in pits was first demonstrated for PTCDA molecules [114], although the structure of the trapped islands could not be determined. A later NC-AFM study with subphthalocyanine molecules showed an ordered structure at the center of the pits, with a mismatched structure at the edges, presumably due to a strong attraction between the molecules and the pit walls [11]. In this section, the influence of nanostructured pits on the growth of PTCDA and C_{60} is investigated.

5.2.1 PTCDA on Nanostructured KBr (001)

Two pit-templated KBr surfaces were considered, one with a mean pit size of 6.5 nm and the other with a mean pit size of 20 nm. Detailed characterization of the nanostructured substrates is given in section 3.3. Using a rate of 0.5 ML/min, a PTCDA coverage of 0.04 ML was used for the 6.5 nm pit sample, and a coverage of 0.4 ML was used for the 20 nm pit sample. These coverages were chosen in order to approximately correspond with the desorbed pit areas of 2 % and 27 %, respectively.

As shown in Figure 5.3, after depositing PTCDA onto the nanostructured KBr (001) surfaces, some of the rectangular pits are filled with molecules. The trapping can be understood on the basis of the same reasoning used to explain why PTCDA islands preferentially form at the bottom of steps: the PTCDA molecules experience local electrostatic interactions and have increased coordination at the bottom of the pit steps. Furthermore, the steps act as additional diffusion barriers; consequently, the mean diffusion length of the molecules is shortened from over 600 nm on the unstructured KBr surface to less than 200 nm on the pitted surface.

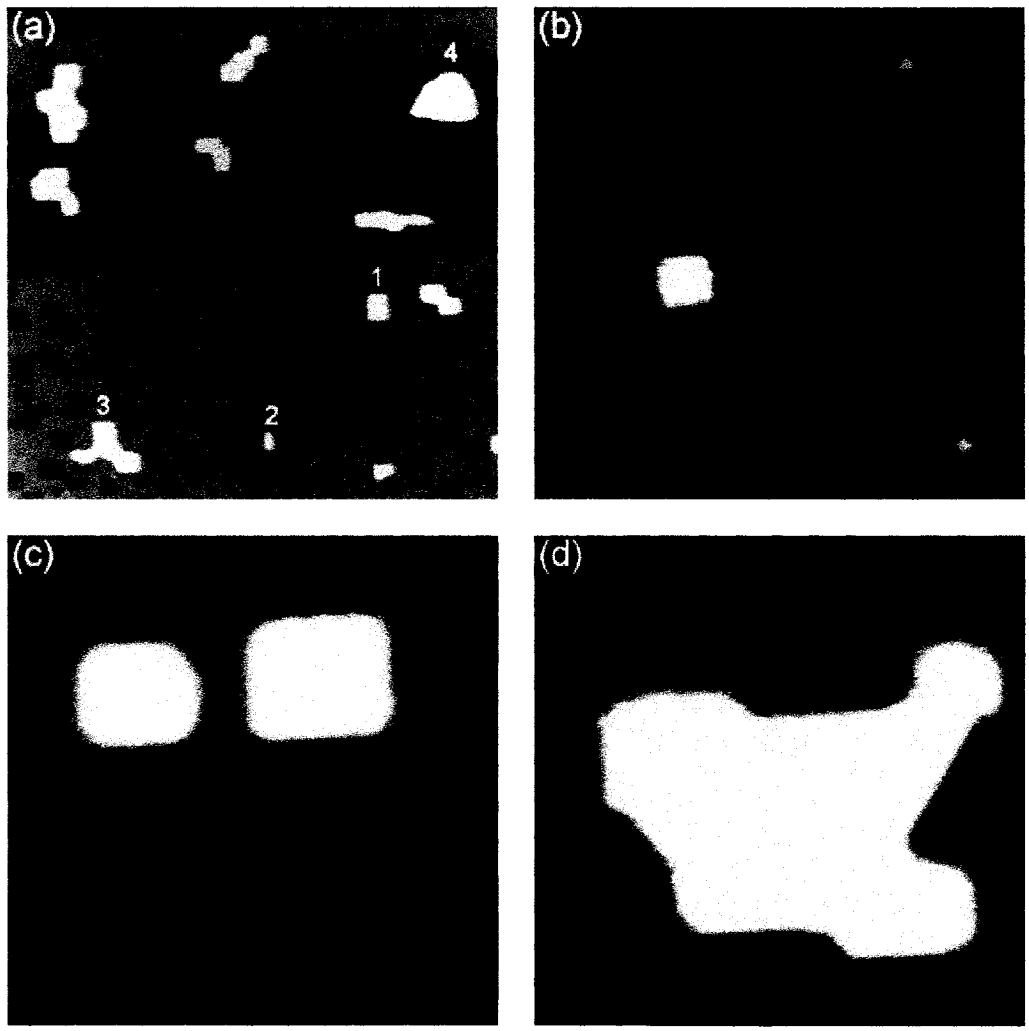

Figure 5.3: NC-AFM images of PTCDA molecules trapped inside monatomic depth pits on a KBr (001) surface: (a) 600 nm x 600 nm overview (mean pit size = 20 nm x 20 nm, Δf = -4.0 Hz) showing the different types of observed islands: 1. islands filling pits, 2. islands partially filling pits, 3. coalesced islands, and 4. large islands; 100 nm x 100 nm images of (b) small filled pits (mean pit size = 6.5 nm x 6.5 nm, Δf = -6.6 Hz), (c) large filled pits (mean pit size = 20 nm x 20 nm, Δf = -4.1 Hz), and (d) coalesced islands (mean pit size = 20 nm x 20 nm, Δf = -4.3 Hz).

The pits appear as 0.33 nm deep holes, while the molecule-filled pits appear as protrusions. Although height information in NC-AFM of heterogeneous systems is not always consistent with the true topographic height [116], the measured height of a PTCDA layer was determined to be 0.326 ± 0.004 nm, which is consistent with other experiments [115]. The vast majority of the PTCDA islands are 3 or 4 layers high, with the first PTCDA layer fully inside the pits and the top 2 - 3 layers protruding. Four main types of islands were observed, labelled 1 - 4 in Figure 5.3 (a): 1. islands filling pits, 2. islands partially filling pits, 3. coalesced islands, and 4. large islands. The islands filling pits are typically 3 or 4 layers high. Some 1 and 2 layer islands have been observed, however, only in the smallest pits, with side lengths smaller than 10 nm. Figure 5.3 (b) shows two small 2 layer islands, and one 3 layer island. All of the observed islands which partially fill the pits are 3 layers high, some with an elongated needle-like shape as seen in Figure 5.3 (a), island 2. The islands made up of smaller coalesced islands are 4 layers high or taller.[27] A small fraction of the islands are even taller, with heights corresponding to 5 - 7 layers. These islands tend to have some edges aligned with the <100> KBr directions, but are not well confined in the pits. Possible reasons for the island heights and shapes will be discussed in more detail later. Close-ups of the most common island types, islands filling pits and coalesced islands, are shown in Figure 5.3 (c) and (d), respectively.

[27] It should be noted that some 3 - 4 layer islands fill merged pits. These islands can be distinguished from coalesced islands by considering whether the component rectangles of the PTCDA island overlap.

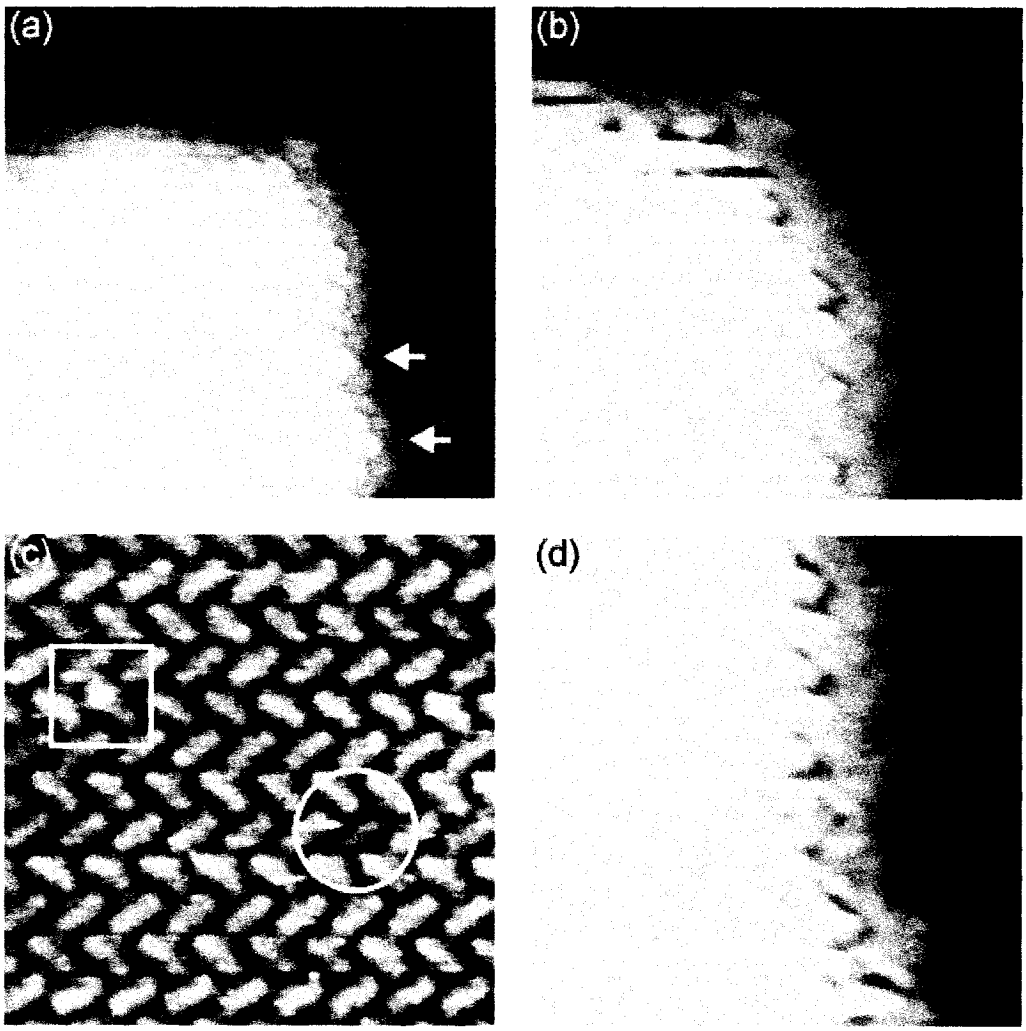

Figure 5.4: High resolution measurements of a 3 layer PTCDA island: (a) 20 nm x 20 nm, Δf = -5.1 Hz. The arrows point to third layer molecules which do not have second layer counterparts, thus precluding tip convolution as the origin of the edge features. 10 nm x 10 nm images showing (b) first, second, and third layer molecules (Δf = -8.6 Hz), (c) individual defects in the third layer (indicated by the square and circle, Δf = -9.4 Hz), and (d) edge molecules which have a distorted appearance during imaging with larger frequency shifts (Δf = -9.8 Hz). Note: these images were processed with a streak removal filter, a high pass filter, and a low pass filter in order to more easily see the structure.

High resolution NC-AFM was used to resolve the arrangement of the PTCDA molecules in the pits. The surface structure of a 3 layer PTCDA island is shown in Figure 5.4, along with the adjacent KBr lattice. The molecules are well ordered, with a herringbone structure similar to that found in the (102) plane of bulk PTCDA crystals [99]. The measured corrugation of the molecules is about 0.05 nm, which is similar to that measured in other NC-AFM studies of PTCDA [111]. To determine the lattice constants, the simultaneous measurement of the PTCDA and the KBr structures makes it possible to use the KBr lattice as a reference, compensating for both the piezo calibration and drift in the measurement. The lattice constants were measured by counting the maximum possible number of atoms or molecules along a primitive vector direction and measuring the distance between the end points from a line profile. The values were then adjusted by taking into account the known KBr lattice constant of 0.66 nm [117]. By averaging the results from 10 images, the third layer PTCDA lattice constants were determined to be $b_1 = 1.24 \pm 0.02$ nm and $b_2 = 1.93 \pm 0.02$ nm. These correspond very closely with the bulk β-phase lattice constants ($b_1 = 1.245$ nm, $b_2 = 1.930$ nm) [99]. The simultaneous measurement of the molecule and substrate lattices also makes it possible to measure a slight rotation of 4.0 ± 0.5 ° between the top PTCDA layer and the <100> direction of the KBr lattice.

High resolution NC-AFM also revealed individual lattice defects, and some first and second layer PTCDA molecules along certain crystallite facets. Second layer molecules can clearly been seen at the island edges in Figure 5.4 (a), (b), and (d). Although one may expect a similar appearance at edges due to tip convolution effects, it is shown in Figure 5.4 (a) that this is visibly not the case. The arrows indicate third layer molecules which do not have corresponding molecules in the second layer. A small shift in the b_1 direction between the second and third layer lattices was measured to be 0.07 ± 0.05 nm.[28] The direction of the shift is consistent with β-phase stacking; however, the magnitude of the shift is smaller than that found in the β structure (0.195 nm) [99]. This measurement may

[28] The large uncertainty reflects the difficulty in accurately measuring the positions of the edge molecules and the variability in the measurement.

indicate a relaxation or distortion of the lattice near the edges, or simply a deviation from perfect β stacking in the first few layers. In addition, the less coordinated, and hence, more weakly bound edge molecules are potentially displaced slightly by the AFM tip during measurement. This is evidenced during imaging at higher frequency shifts which show edge molecules with a modified appearance (Figure 5.4 (d)). In addition to the third and second layer molecules, two first layer molecules are seen in the upper right hand corner of the island in Figure 5.4 (b). These molecules appear to, at least approximately, be arranged according to the 2 x 3 lattice structure shown in Figure 5.5. A detailed discussion of the first layer structure at the island corner will be given at the end of the section. As expected, the molecular layer has nearly the same height as the KBr step height. Two defects in the third PTCDA layer can be seen in Figure 5.4 (c). One is a small protrusion (shown inside the square) which may correspond to a small contaminant or a defective PTCDA molecule. The other defect (circled) is a slightly dimmer molecule, which may indicate the presence of a vacancy or stacking fault below the molecule.

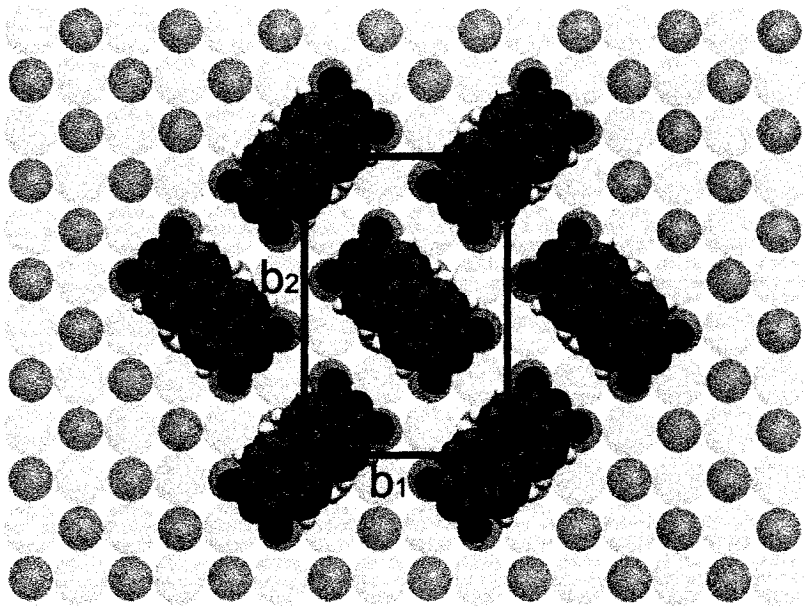

Figure 5.5: Schematic of a commensurate 2 x 3 PTCDA overlayer, which would allow the carbonyl oxygen atoms of the molecules to sit in close proximity to the K^+ surface ions (shown in blue). This PTCDA structure has a large strain in the b_1 direction, which may prevent exact commensurability in that direction.

Although it was possible to image the third layer and some of the first and second layer edge molecules, the structure of the buried layers is uncertain. It is believed that in the first layer, arrangements which maximize the interaction of the carbonyl oxygen atoms of the PTCDA with the cation sites of the alkali halide will be favoured [115]. Coincident PTCDA lattice structures on KBr are predicted for b_1 = 1.260 nm, b_2 = 2.006 nm, with a rotation of 23.3 ^{o} [118]. However, because the first layer here is constrained by the boundary conditions imposed by the KBr <100> pit walls, such a structure is unlikely. Instead, it is proposed that the first layer molecules align with the KBr <100> walls, leaving the layer strained by the resulting lattice mismatch. A commensurate 2 x 3 overlayer would allow all of the carbonyl oxygen atoms to sit in close proximity to the potassium surface ions (see Figure 5.5); however this structure has a rather large mismatch of 6.02 % in the b_1 direction and 2.59 % in the b_2 direction when compared with the β-phase structure. To reduce the lattice mismatch, it is more probable that a coincident structure may occur with commensurability in the b_2 direction, but not the b_1 direction. This hypothesis is supported by the observation of some elongated islands, as seen in Figure 5.3 (a) (island 2). The growth of quasi 1-d structures due to lattice match in one direction and mismatch in the other has previously been observed in other systems [62]. It is expected that the second layer takes on an intermediate structure between the stressed first layer and the slightly rotated, bulk-like third layer.

The mismatch between the PTCDA and the KBr lattices, and the resulting stress in the first 2 PTCDA layers, may explain the observed heights of the islands. As shown in Figure 5.3 (a), the pits are sometimes only partially filled with 3 layer crystallites. This, and the relative scarcity of shorter islands, points to an instability of the first two PTCDA layers. Thus, it is preferable for the molecules to stack three layers high, with the third layer having the bulk lattice constant, than to form an extended 1 or 2 layer island. The instability of 1 - 2 layer islands also explains why only islands 4 layers high or taller "leak out" of the pits and form coalesced islands: in order to have a stable configuration (more than 3 layers) extending laterally outside of the pits, the regions inside the pits must be at least 4 layers high. The 3 layer islands are well confined since there are only 2 layers protruding from the pits. The concept is illustrated in Figure 5.6.

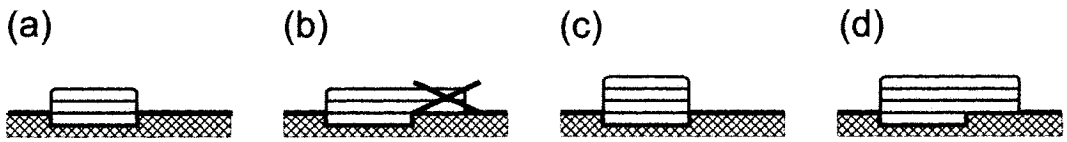

Figure 5.6: Cross-sectional illustrations depicting how an instability in the first 2 PTCDA layers can explain the observed island heights: (a) 3 layer islands are well confined in pits, since a 2 layer section extending outside of a pit is not allowed (b). 4 layer islands may be confined (c), or may extend outside of the pit (d), if there are enough molecules.

As mentioned previously, a small number of pits were observed with a height of 1 or 2 layers (see Figure 5.3 (b)), however only in pits with a side length smaller than 10 nm. This size effect is a result of the increased influence of the pit corners and edges in the smaller pits. It has previously been shown that the electrostatic potential inside the pits has a pronounced minimum at the corners and a gradually varying component which decays with the distance from the corners [11]. The enhanced trapping potential in the smaller pits appears to be sufficient to stabilize the otherwise unfavoured 1 - 2 layer PTCDA islands. A similar size effect was observed for subphthalocyanine molecules [11], where only pits smaller than 15 nm were filled with molecules. It is estimated that the smallest observed pits contain as few as 6 - 8 molecules (see e.g. Figure 5.3 (b)).

In addition to structural information, some dynamical information can be extracted from the high resolution NC-AFM data. As seen in Figure 5.7, some streaks are apparent on top of the PTCDA. Such streaks are characteristic of a mobile species, moving on a time scale faster than the time required for imaging. Similar noise in STM measurements due to diffusing species was first reported by Binnig *et al.* for mobile oxygen on a nickel surface [119], and has later been reported by several groups in molecular systems, including PTCDA on Au [101] and Ag [120] surfaces. Repeated measurements revealed that the streaks were only present over the PTCDA islands, and not the KBr areas. Therefore, the streaks are most likely due to the migration of PTCDA molecules, which

are confined to the top of the PTCDA islands. This interpretation is further supported by the fact that islands with incomplete layers were never observed. Instead of forming a partial layer, the molecules constitute a 2-dimensional gas confined by the island edges. The atomic resolution measurements of the bare KBr surface also contradict the literature statement that the KBr lattice cannot be imaged between PTCDA islands because of molecular diffusion [111].

An estimate of the energy barrier for the diffusion of a PTCDA molecule on a PTCDA surface was extracted by analyzing the distribution of the streak lengths. The probability that a molecule remains at the same position after a fixed amount of time is given by equation 4.1. Since the AFM tip is in motion during imaging, the residence time at a given position is only approximately related to the streak length. A more accurate determination of the residence time at a fixed position was obtained by plotting the streak length distributions for various tip velocities, calculating the associated time constants, and then extrapolating to zero tip velocity (see Figure 5.7). By this method, the hopping frequency was determined to be $\nu = 27 \pm 2\ s^{-1}$. Using equation 4.2 and assuming a typical attempt frequency of $\nu_0 = 10^{13}\ s^{-1}$ [121], the diffusion barrier for PTCDA on a PTCDA surface was calculated to be $E_D = 0.7 \pm 0.2$ eV. The error in the diffusion barrier reflects the uncertainty in the attempt frequency, which was assumed to have a lower limit of $10^{10}\ s^{-1}$ and an upper limit of $10^{16}\ s^{-1}$. The estimated value of the diffusion energy barrier correlates well with other studies of molecular diffusion [102, 122].

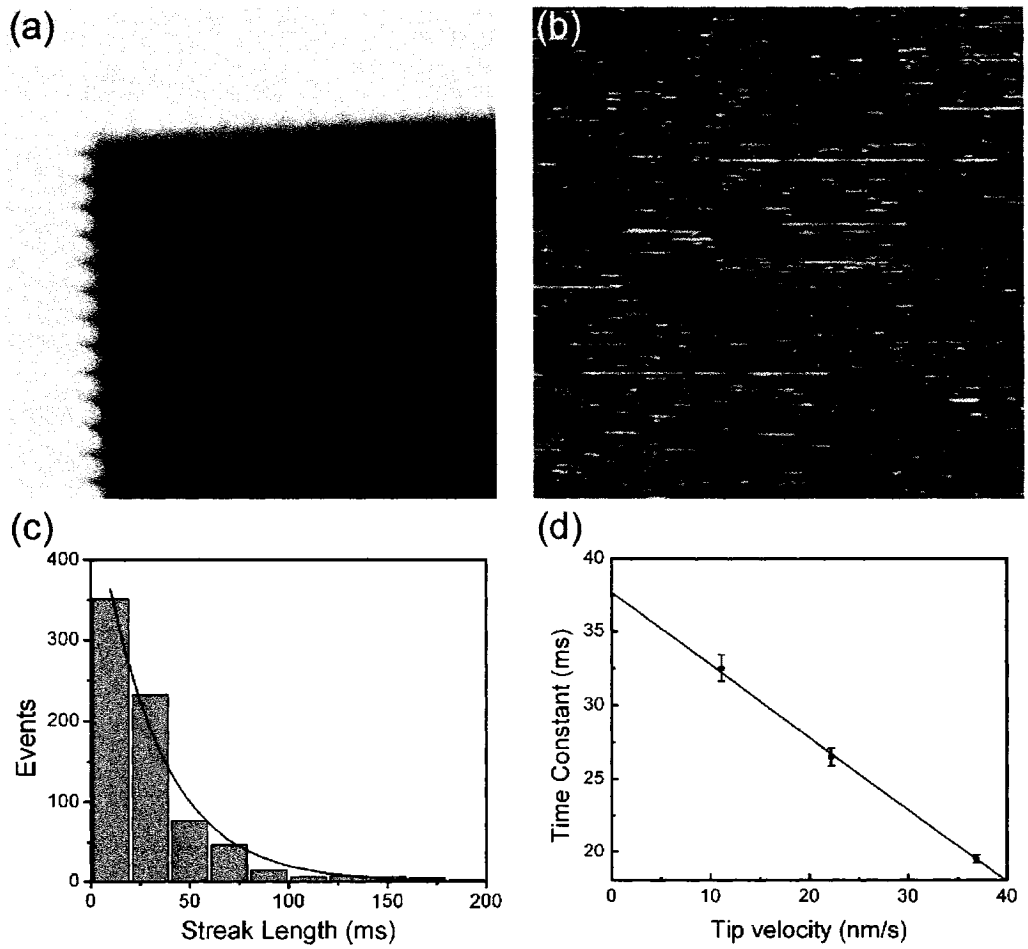

Figure 5.7: NC-AFM measurements of the substrate (a) show a clean KBr lattice (raw data, 10 nm x 10 nm, Δf = -9.7 Hz), while measurements taken on top of an adjacent PTCDA island (b) show streaks which are characteristic of diffusion events (raw data, 10 nm x 10 nm, Δf = -10.0 Hz). (c) The corresponding streak length distribution and exponential fit. (d) The time constants taken from exponential fits of the streak length distributions vary linearly with the tip velocity during measurement. The extrapolated value at zero tip velocity provides an estimate of $1/\nu$.

Several remarks about NC-AFM imaging considerations are in order. On ionic surfaces, one species of surface ion is imaged as bright and the other is imaged as dark, depending on the charge of the AFM tip apex. On lattices with inequivalent sites, such as CaF_2 (111), the species on the surface ions and the sign of the tip charge can be identified based on the asymmetry of the imaged lattice [123]. For highly symmetric ionic crystals, sublattice identification has so far only been possible though the analysis of site-specific force distance curves at low temperatures [29]. Here, an alternate method of sublattice identification is proposed. As seen in Figure 5.8, the first layer PTCDA molecules are aligned with the corrugation maxima (bright spots) of the imaged substrate lattice. In order to identify the corrugation maxima as K^+ ions or Br^- ions, the expected specificity of the molecule-substrate interaction is taken into account. In particular, the negatively charged oxygen groups at the extremities of the PTCDA molecules should be attracted to the surface K^+ ions. Therefore, it is reasonable to conclude that the bright surface ions represent K^+ ions. In this configuration, the oxygen groups of the PTCDA at the KBr step sit on top of two K^+ ions, and face another (Figure 5.8 (c)).

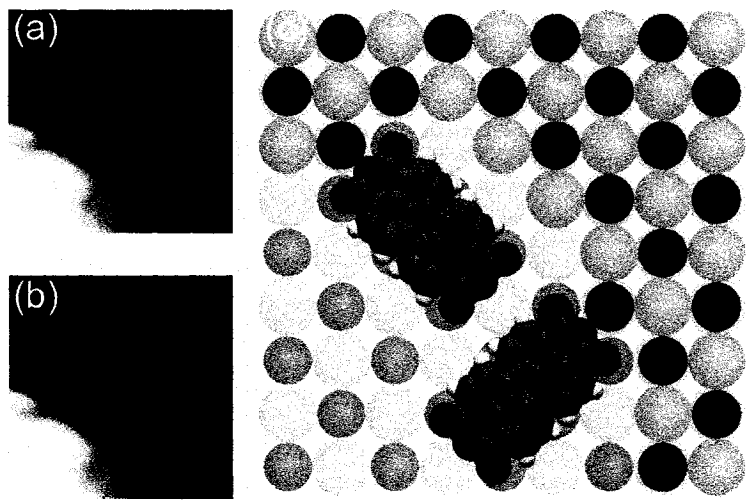

Figure 5.8: First layer PTCDA at the corner of a pit: (a) High resolution NC-AFM image, 3 nm x 3 nm, Δf = -8.6 Hz, (b) with lines showing the alignment of the PTCDA molecules with the imaged KBr lattice. (c) Model of the corresponding structure (blue = K^+, yellow = Br^-).

The measurement of the surface cations as corrugation maxima, implies a positively terminated probe tip [36]. In the case of this experiment, it is most likely that it is a K^+ ion at the tip apex, since the transfer of material from the substrate to the tip during imaging is thought to be common [35]. This is frequently manifested during imaging as distinct jumps ("tip changes"), or more dramatically during the sample approach ("tip crash"). An example of a reversible tip change, seen just prior to the high resolution measurements in this section, is shown in Figure 5.9. The tip change is accompanied by a change in the image detail, even though the frequency shift remains the same. This demonstrates, as other studies have [35], the important influence of the final tip atoms on the sensitivity to short range forces during the NC-AFM measurement. The tip change in Figure 5.9 is possibly a K^+ ion jumping from the surface to the sample or a rearrangement of the tip structure. While it should be emphasized that it is exceedingly difficult to substantiate any claims about the detailed tip structure, the transfer of a K^+ ion to the tip apex is consistent with the observation that the measured height change associated with the tip change is 0.23 ± 0.05 nm. This is comparable to the ionic diameter of K^+, which is about 0.28 nm [117]. The identification of the imaging atom is useful for modeling the origin of the contrast formation during NC-AFM measurement.

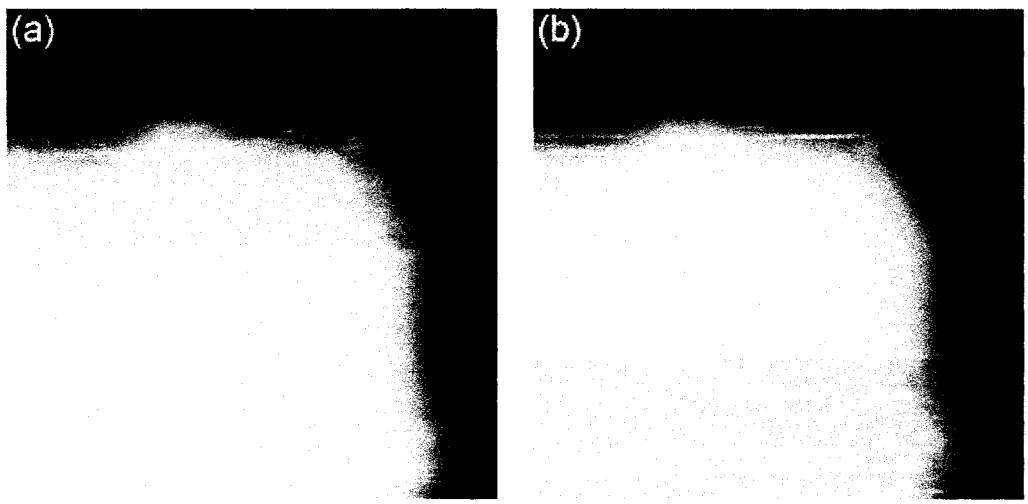

Figure 5.9: A reversible tip change is observed during NC-AFM imaging, accompanied by (a) a switch from higher to lower resolution (20 nm x 20 nm, Δf = -4.3 Hz), and (b) vice versa (20 nm x 20 nm, Δf = -4.7 Hz).

Finally, by performing scans at progressively negative frequency shifts (larger attractive forces), it was found that PTCDA islands could be manipulated out of the pits. In the case shown in Figure 5.10, a frequency shift of -13.0 Hz was used to move the molecules out of the pit. Based on the method developed by Sader and Jarvis [124] for converting frequency shifts to forces, this corresponds to an average attractive force of about 10 nN. Similar forces were required for manipulating other islands of comparable size. The pit in Figure 5.10 appears to be a bit smaller than the PTCDA island, indicating that the upper layers "overflow" slightly outside of the pit. Some of the molecules remain at the pit edges after the initial manipulation (Figure 5.10 (c)), indicating a stronger PTCDA-substrate interaction at the steps. This is not surprising given that step edges have an enhanced electrostatic interaction, because they are less coordinated, and that the edge PTCDA is attracted to the K^+ at the steps (Figure 5.8). In addition, the pit edges have a ragged appearance. This may also stem from the attraction of the PTCDA to the step edges, and may either be because of a rearrangement of the step edges to accommodate the molecules, or due to edge ions being uprooted during the PTCDA manipulation. The first interpretation is supported by the pit shape observed at the corner in Figure 5.8. The visible pit edge is along a <110> direction, instead of the usual <100> directions.

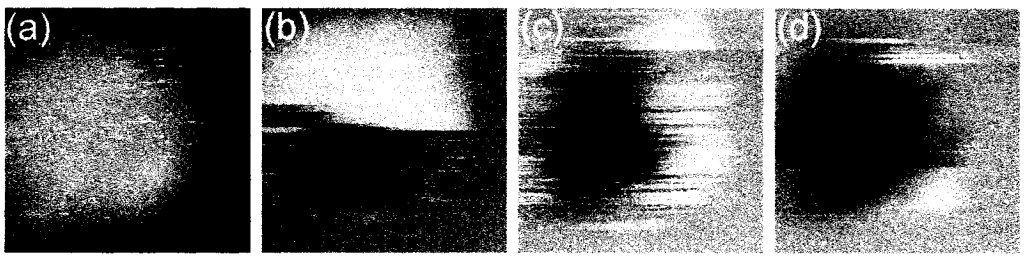

Figure 5.10: Sequence of images recorded (a) before (Δf = -10.0 Hz), (b) during (Δf = -13.0 Hz), and (c), (d) after (Δf = -10.0 Hz) PTCDA molecules are manipulated out of a pit. Each image has a frame size of 10 nm x 10 nm.

5.2.2 C_{60} on Nanostructured KBr (001)

Pits were created with a mean side length of 20 nm. Using a rate of 0.4 ML/s, 0.6 ML of C_{60} was deposited onto the substrate. Overview images are shown in Figure 5.11. As with the PTCDA molecules, the pit steps act as additional diffusion barriers, shortening the mean diffusion length from over 600 nm on the unstructured KBr surface to 100 - 200 nm. The C_{60} islands were typically 2 layers high, as is the case for C60 on the unstructured KBr (001) surface. The C_{60} layer height was measured to be 0.81 ± 0.01 nm, which is in agreement with the expected height of 0.818 nm, i.e., the spacing between <111> planes in bulk crystals [107].

Although there are some rare indications of trapping of first and upper layer molecules at step sites (see Figure 5.11 (b)-(c)), in general, the interaction between the C_{60} and the pit steps is insufficiently strong to confine the molecules. This is not unexpected, given the fact that C_{60} islands typically spread across KBr steps. The high resolution image in Figure 5.11 (c) shows some loosely bound third layer molecules at a step edge: The molecules appear as streaks, because they are mobile; however, the streaks are confined to a small area, because they are trapped by the step potential. Measurements performed while scanning from right to left and from left to right showed trapping in the same areas, demonstrating that the build-up of molecules at one side of the pit is not tip-induced.

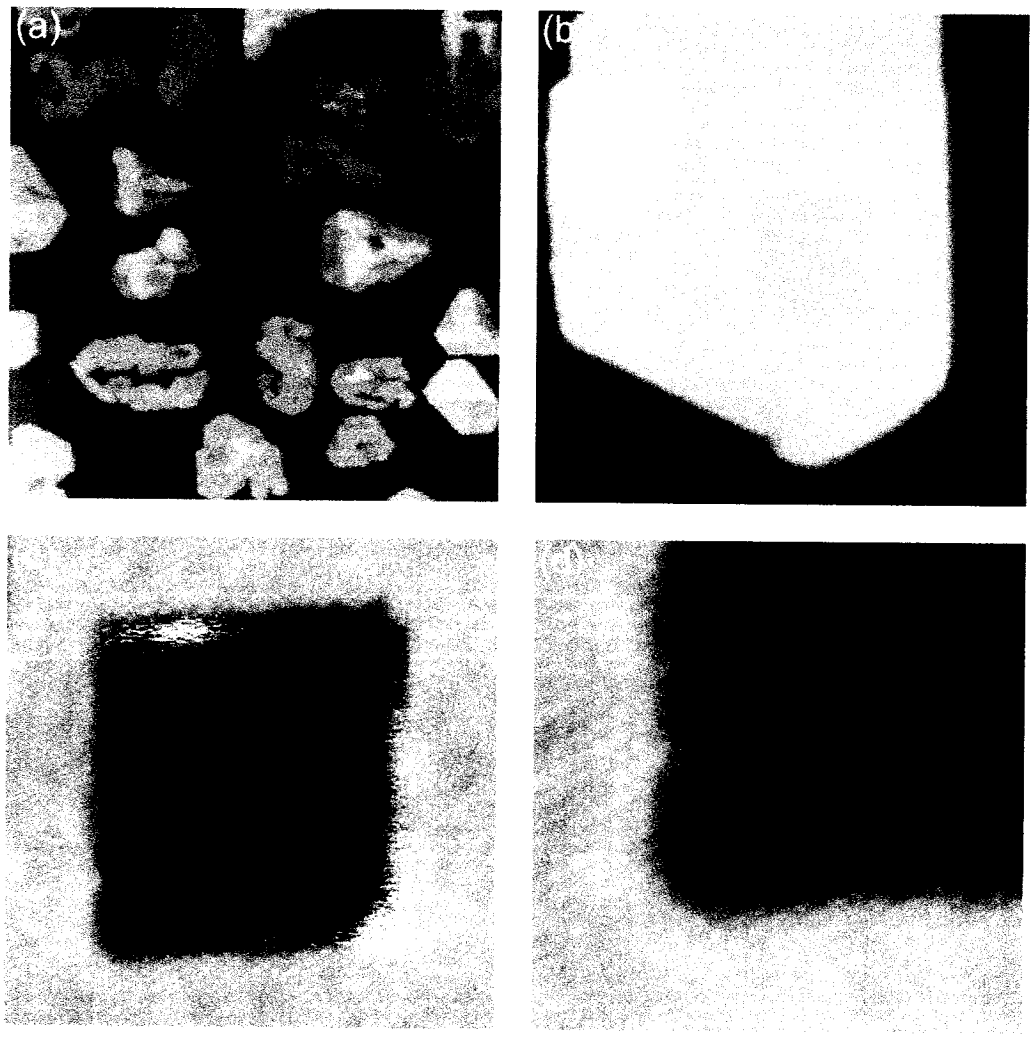

Figure 5.11: NC-AFM images of C_{60} on a pitted KBr (001) surface: (a) 600 nm x 600 nm overview (Δf = -3.5 Hz), (b) 100 nm x 100 nm close-up of an island with trapped third layer molecules (Δf = -6.0 Hz), (c) 40 nm x 40 nm molecular resolution image showing evidence of loosely bound molecules at step edges (Δf = -8.2 Hz), (d) 20 nm x 20 nm molecular resolution image showing the structure of the C_{60} lattice as it spans across a KBr step(Δf = -10.2 Hz).

Generally, as seen in Figure 5.11 (d), the molecular lattice is unaffected at the steps. The C_{60} layers sit atop the substrate much like a carpet, covering and conforming to the topography of the substrate below. That is not to say that the pits do not affect the structure of the C_{60} islands. To the contrary, despite the weak trapping by the pits, all islands were observed to have some facets which are aligned with the <100> directions of the substrate. This alignment is seen directly in high resolution images which show the structures of the C_{60} and KBr lattices (see Figure 5.12). By averaging the results from three images, the second layer lattice constants were determined to be $b_1 = 0.99 \pm 0.02$ nm and $b_2 = 0.99 \pm 0.01$ nm.[29] These correspond closely with a 13 x 3 coincident structure ($b_1 = 0.990$ nm and $b_2 = 0.990$ nm); however, an 8 x 3 structure ($b_1 = 1.010$ nm and $b_2 = 0.990$ nm) is within the uncertainty range and cannot be ruled out (see Figure 5.12). Furthermore, it should be noted that the first layer C_{60} structure may differ slightly from the second layer structure. Previous measurements in our lab determined an 8 x 3 coincident structure for a C_{60} island at a <100> step [112]. However, lattice averaging methods were required, since it was not possible to directly observe the KBr lattice positions [10]. This technique is prone to error because of difficulties related to defining an accurate unit cell for the unit cell averaging.

[29] The lattice constants were determined in the same way as outlined for PTCDA in Section 5.2.1, i.e., by direct counting and measurement of distances from line profiles.

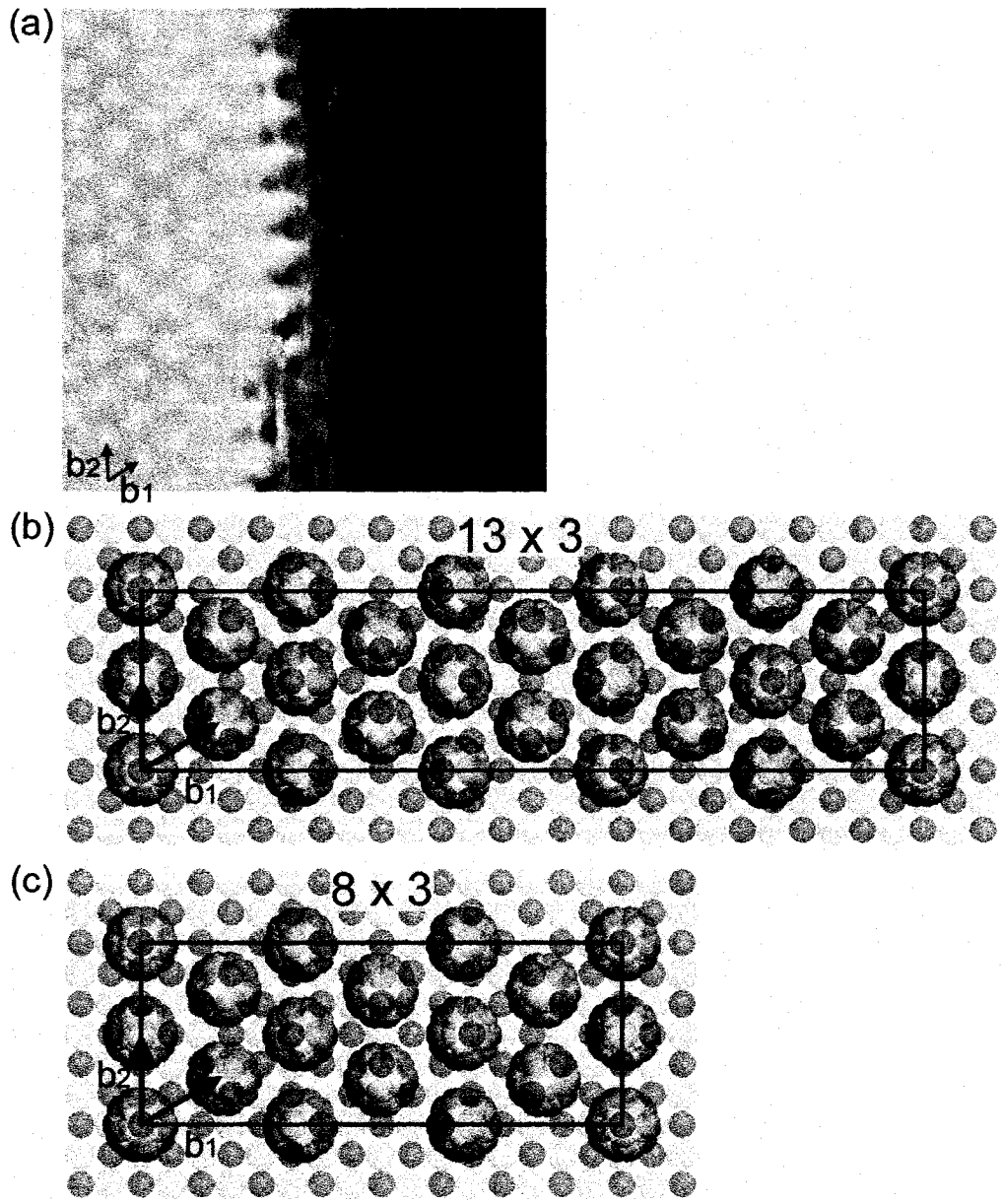

Figure 5.12: (a) High resolution NC-AFM image used to determine the relationship between the KBr substrate and the C_{60} overlayer. (Rotated by 90 ° to correspond roughly with (b) and (c), high-pass and low-pass filtered, Δf = -13.3 Hz). Schematic of the (b) 13 x 3 and (c) 8 x 3 coincident structures.

The peculiar patterns of bright and dim C_{60} molecules were seen on all of the islands. It was observed that the number of bright versus dim molecules varied with time and varied from C_{60} layer to C_{60} layer. Generally, as time progressed, the number of dim molecules increased. Measurements of the second C_{60} layer taken within 12 hours of deposition showed very few dim molecules, less than 2 %. The height difference between the isolated dim molecules and the surrounding bright molecules is 0.021 ± 0.004 nm. After more than 24 hours, measurements of several 2 layer islands showed a spectrum of molecular heights, with a maximum height difference between bright and dim of 0.050 ± 0.004 nm (Figure 5.13 (b)). Over the course of the measurements some individual switching events were observed. There were a few examples of switching from bright to dim, but only one instance of switching from dim to bright. An individual switching event is shown in Figure 5.13 (c)-(d), captured by imaging the same 20 nm x 20 nm area for 2 hours. There appeared to be little change in the bright/dim patterns after more than 48 hours following the C_{60} deposition.

The dependence of the bright/dim pattern on the C_{60} layer is shown in Figure 5.14. After more than 48 hours, the first layer had a uniform appearance (Figure 5.14 (a)). There are two obvious interpretations: (1) all of the molecules are bright, or (2) all of the molecules are dim. It should be noted that the sample had very few first layer regions; therefore, it was difficult to verify whether other areas had any bright or dim molecules. The third layer (Figure 5.14 (c)) had a similar appearance to the second layer (Figure 5.14 (b)), although the pattern had a more continuous range of heights, with a maximum height difference of 0.076 ± 0.005 nm (versus 0.050 ± 0.004 nm for the second layer).

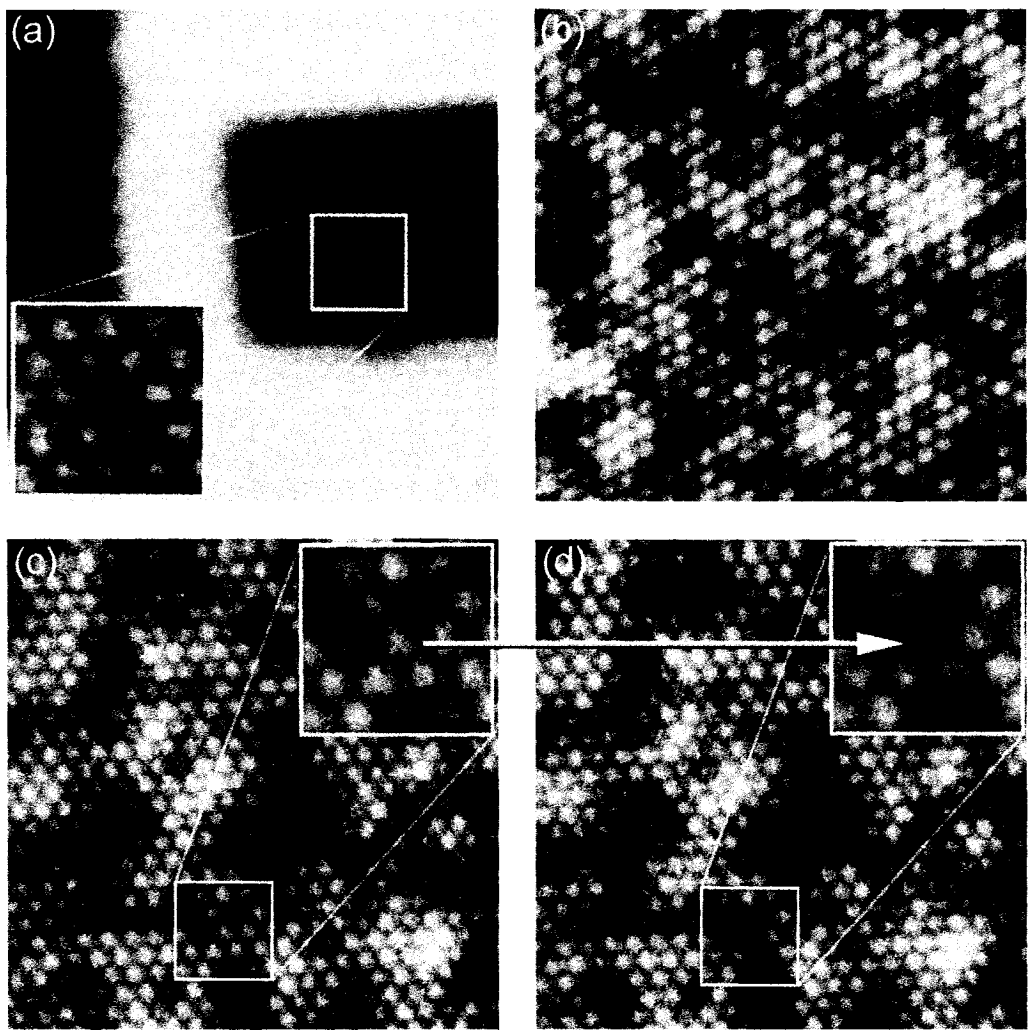

Figure 5.13: The time dependence of the second layer C_{60} bright/dim patterns: 20 nm x 20 nm NC-AFM measurements taken (a) 12 hours (Δf = -13.1 Hz), and (b) 32 hours (Δf = -9.8 Hz) after C_{60} deposition. An individual switching event is captured with a single molecule changing from (c) bright (Δf = -9.8 Hz) to (d) dim (Δf = -9.8 Hz). All insets are 4 nm x 4 nm.

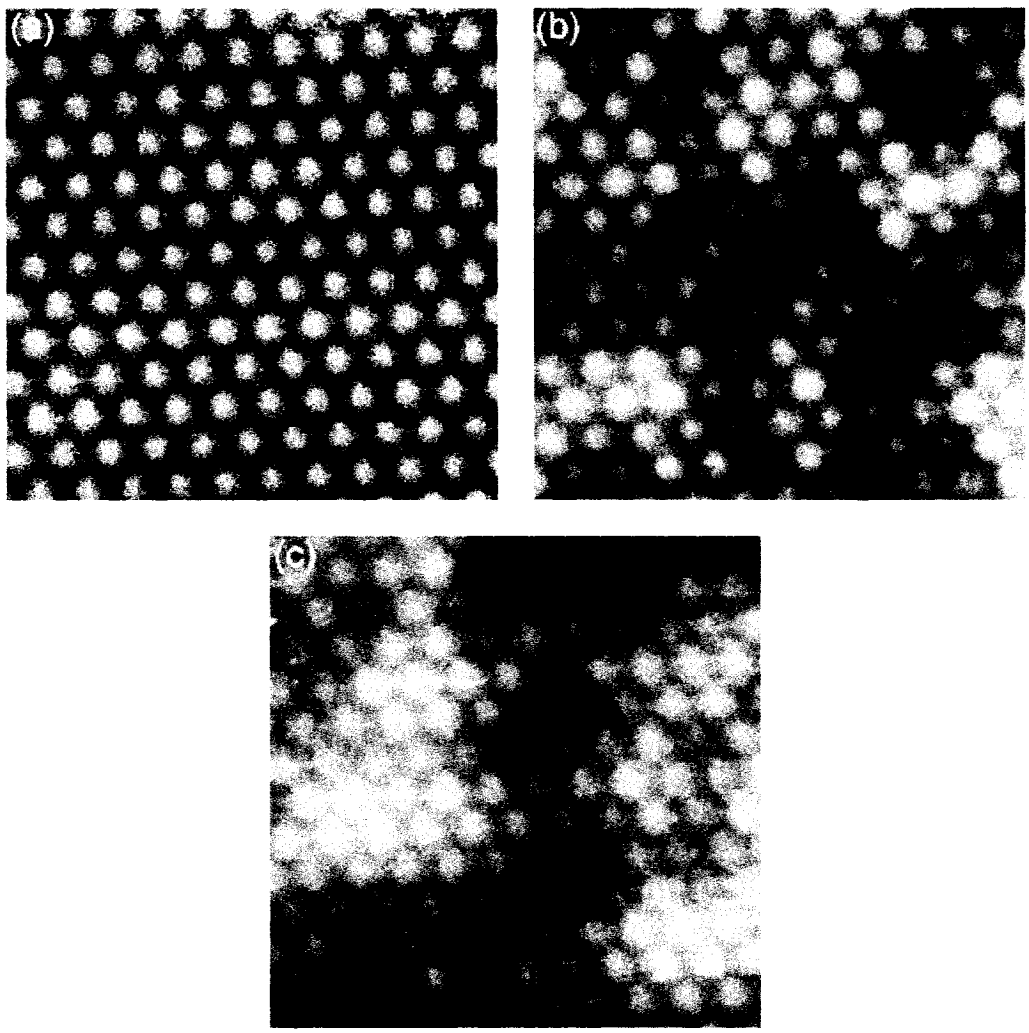

Figure 5.14: NC-AFM measurements (10 nm x 10 nm) showing the layer dependence of the bright/dim C_{60} patterns: (a) first layer (Δf = -9.6 Hz), (b) second layer (Δf = -9.7 Hz), (c) third layer (Δf = -9.6 Hz).

C_{60} molecules with differing heights have been seen by STM on several metal substrates [102, 104, 105]; however the cause of the observed heights has been a topic of strong controversy [102]. On some substrates, the heights are accounted for by electronic differences between differently oriented molecules [105], while on other substrates the heights are thought to have a geometric origin, either due to reconstruction of the

underlying substrate [103], or because of lattice buckling [104]. It should be noted that the height differences measured on metal surfaces are typically 10 times larger than those measured on KBr. It was previously suggested by our group [112] that the subtle height differences seen in the C_{60}-KBr system can be explained by the geometric height differences between C_{60} molecules contacting the substrate with 5-fold versus 6-fold rings.

In light of the new results presented in this section, many of the above explanations can be ruled out as origins of the two molecular heights seen in the C_{60} - KBr system. Firstly, most of the above mechanisms are interface effects; that is, the measured height of the first layer molecules is modified because of the nature of the molecule-substrate interaction. This may lead to charge transfer, a preferred molecular orientation at the interface, or a reconstruction of the substrate surface. Although some of the resulting height differences would be transferred to the C_{60} layers sitting on top, the height differences seen in the upper layers would be similar to or smaller than the differences in the bottom layers. Clearly, this cannot account for why the upper layers have progressively larger height differences. Moreover, the fact that the height difference is larger in the upper layers is a strong indication that the effect is geometric, and occurring in each of the layers. Therefore, the topography of each layer contributes additively to the overall measured heights.

In the second layer, the maximum height difference is 0.050 ± 0.004 nm. It is expected that this maximum value represents the topographic difference between a bright molecule sitting above first layer bright molecules (bright + bright) and a dim molecule sitting above first layer dim molecules (dim + dim). Assuming that the bright and dim molecules have consistent height differences in each of the layers, the height difference per layer is half of the value obtained from the second layer topography. This yields a height difference per layer of 0.025 ± 0.002 nm, which correlates well with the height difference for an isolated dim molecule, 0.021 ± 0.004 nm. Furthermore, in the third layer, the maximum measured height difference is 0.076 ± 0.005 nm. This is expected to represent the situation of (bright + bright + bright) – (dim + dim + dim). The height

difference per layer is calculated to be 0.025 ± 0.002 nm, also in accordance with the measurements of isolated dim molecules. Thus, it is postulated that each geometric distortion contributes about 0.0025 nm to the topographic change. However, this picture is complicated by the fact that each molecule in the close-packed layers sits on top of three molecules, some of which may be bright and some of which may be dim, leading to intermediate heights. The geometric origin of the height differences is also supported by the observation that the third layer has a more continuous spectrum of heights than the second layer. This is because in taller islands, there are more contributing layers, and hence, more possible ways to add the constituent heights.

There are two main geometric mechanisms to consider: lattice buckling and molecular orientation effects. The first explanation was initially presented by Pai *et al.*, where it was observed that under certain growth conditions, the C_{60} on a Cu (111) surface is highly compressed, with a C_{60} nearest neighbour distance of 0.9654 nm [104]. In response to the C_{60} - C_{60} repulsion, some of the C_{60} in the lattice buckles in or out of plane. Because the C_{60} sits on a lattice with triangular symmetry, the situation is much like in a system of coupled antiferromagnets on a triangular lattice, with the upward and downward buckling analogous to the spin up and spin down states. This type of frustrated system can lead to complex disordered maze patterns (see Figure 5.15). In the case under consideration here, the lattice is also compressed, but to a lesser degree; the nearest neighbour distance is 0.99 ± 0.02 nm versus 0.9654 nm in the C_{60} on Cu (111) system. The nearest neighbour distance in the bulk is 1.02 nm. Therefore, it is not unexpected that the distortions would be smaller than the case of Cu (111). Qualitatively, the bright-dim pattern resembles the disordered maze pattern arising from the frustrated magnet system. However, the situation under consideration here is further complicated by the interactions between layers. Although this mechanism has some attractive features, it should be noted that based on a buckling displacement of about 0.025 nm, the effect on the nearest neighbour distance is minimal (0.0003 nm). Thus, the energy benefit gained from buckling appears to be negligible, making buckling an unlikely factor. In the case of Cu (111), where the displacements are 10 times larger, the effect is considerable. Moreover, it is improbable

that the molecules can buckle inward towards the substrate, as would be implied by the appearance of dim molecules.

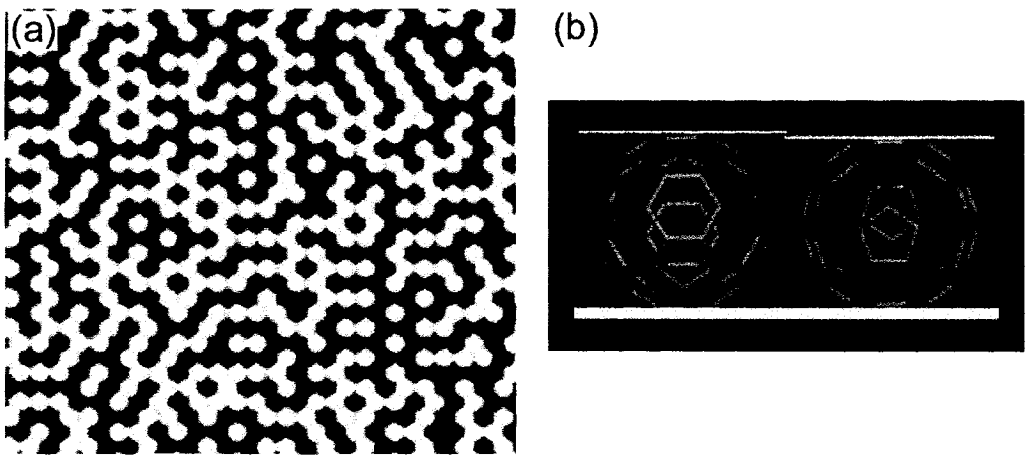

Figure 5.15: (a) A simulation of a buckled C_{60} lattice, with the C_{60} behaving much like coupled antiferromagnets on a triangular lattice (figure reproduced from [104]), (b) The two C_{60} orientations proposed by Burke *et al.* [112], with a 5-fold ring (left) and 6-fold ring (right) facing the substrate (figure reproduced from [112]).

The other potential source of topographic height differences, preferred molecular orientations, was previously considered in our group [10, 112]. Earlier measurements showed a few dim molecules, each with a measured height difference of 0.021 ± 0.003 nm with respect to the surrounding molecules. This height closely correlates with the geometric height difference of 0.0207 nm between molecules with 5-fold rings or 6-fold rings facing the substrate (Figure 5.15). It was thought that the interaction between the C_{60} and the KBr may be sufficiently strong to inhibit rotation in the first layer, and favour the proposed orientations. However, as mentioned above, this sort of interface effect cannot explain the height differences seen in upper layers. Furthermore, it is unlikely that the C_{60} in the upper layers would adopt the suggested orientations. In bulk C_{60}, at room temperature, the molecules rotate quasi-isotropically at a rate of 10^{10} Hz [106]. A first-order phase transition occurs at about 260 K, in which

there are two preferred orientations. However, the molecules rapidly switch between the orientations at about 10^9 Hz [125]. The two configurations, denoted H and P, are shown in Figure 5.16. In the H configuration, a hexagon faces the double bond of a neighbouring molecule, and in the P configuration, a pentagon faces the double bond of its neighbour [126]. The rotations are frozen out at temperatures below about 90 K [127]. Similar phase transitions also occur as a result of applied pressure (see Figure 5.16). Although the P orientation has a lower energy under ambient conditions, the H orientation occupies a 1 % smaller volume [128]. Therefore, as the pressure is increased, the smaller H phase is favoured, and the proportion of H molecules increases. It should be noted that even if the rotations were frozen, with some molecules in the P and some in the H configuration, the associated height difference would be 10 times too small to account for the observed heights.

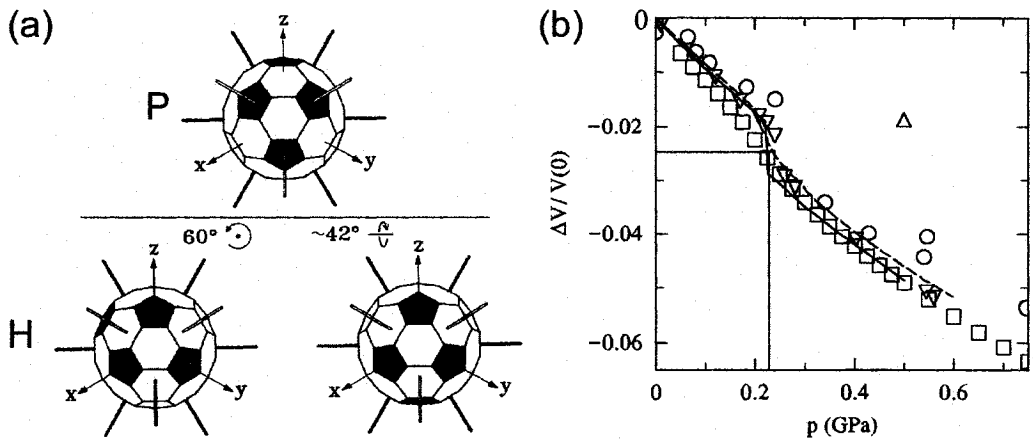

Figure 5.16: (a) A top view of (111) plane C_{60} in the P and H orientations. The 12 nearest neighbours sit in the 12 <110>directions, represented by the rods, with either a pentagon (P) or a hexagon (H) facing double bonds of neighbouring molecules. There are 2 inequivalent H orientations which are related to the P orientation by rotations about the [111] or [1$\bar{1}$0] directions (figure adapted from [126]). (b) The dependence of the fractional volume change in a C_{60} crystal on pressure, with data from several groups. A phase transition from an orientationally disordered to an orientationally ordered phase takes place at about 0.22 GPa. The strain-induced volume change for the experiments under consideration is denoted in red (figure adapted from [129]).

An alternative explanation for the height differences is as follows. When pressure is applied to a C_{60} crystal, the lattice constant is reduced, and the nearest neighbour interactions become increasingly important. This hinders molecular rotation, and leads to favoured orientations. Because the C_{60} lattice in the sample under consideration is strained, it is expected that a similar optimization of the nearest neighbour interactions is at play. The measured nearest neighbour distance in the C_{60} films is about 1.2 % smaller than in the bulk, corresponding to a fractional volume change of 3.5 %. This is similar to the nearest neighbour distance in a C_{60} crystal held at a pressure of about 0.22 GPa. This is also the pressure at which the first phase transition occurs, at room temperature [129] (see Figure 5.16). Therefore, it is proposed that during observation of the sample in the first 12 hours, the C_{60} has not yet entirely cooled to room temperature, and the C_{60} is rotating quasi-isotropically. At later times, the sample is at the phase transition, with some of the molecules having reduced rotational freedom, and others still rotating nearly freely.

The observed height difference can be accounted for by the difference in height between the two types of rotating molecules. The nearly freely rotating molecules rotate in all directions, and on average, over the time scale of the measurements, have a spherical shape. The other molecules, although rapidly switching between the H and P orientations, are always sitting with a hexagonal face parallel to the surface (see Figure 5.16). The resulting height difference Δh is given by

$$\Delta h = h_{rot}\left(\frac{d_{rot} - d_6}{d_{rot}}\right), \tag{5.1}$$

where h_{rot} is the measured height of the taller species; d_{rot} and d_6 are the calculated diameters of the rotating and 6-fold ring down configurations. The rotating molecules have a diameter d_{rot} given by the average diameter of a truncated icosahedron, which is the geometric shape of a C_{60} molecule. The diameter d_6 is the distance between the hexagonal faces. For a truncated icosahedron with an edge length of 1, $d_{rot} \approx 4.727$ and

$d_6 \approx 4.535$ [130]. With a measured h_{rot} = 0.81 nm, the height difference Δh = 0.033 nm. This corresponds reasonably well with the estimated height difference of about 0.025 nm. The above hypothesis can be tested experimentally by performing the same measurements at a lower temperature. It is anticipated that all of the bright molecules will become dim as the molecules go into the rotationally ordered state, leaving a uniform C_{60} topography.

As for the observed patterns, given that the orientation of a C_{60} molecule affects its interaction with its neighbours, especially when the lattice is compressed, it is not surprising that the bright - dim pattern is not random. Adjacent molecules in the H and P state fit together by means of the electron rich double bond of one molecule facing the electron poor opening in the hexagon or pentagon of the other molecule [126]. It is likely that the H and P oriented molecules recruit adjacent molecules to adopt the same orientations, in order to optimize the nearest neighbour interactions. Conversely, the quasi-isotropically rotating molecules are less likely to have H and P oriented molecules beside them since the rotating molecules essentially act as spheres, with little influence on the orientation of their neighbours. Therefore, it is proposed that the dim molecules preferentially appear next to other dim sites, leading to propagating fronts of dim molecules as the phase transition proceeds.

Finally, after annealing the sample at 175 °C for 3 hours, the island shapes became more compact (Figure 5.17). This provides an indication that the branching structures seen prior to heating are metastable. It is expected that the islands adopt their compact morphologies via edge diffusion, which is facilitated at elevated temperatures. In addition, most of the islands are 3 layers high, instead of the 2-layers seen prior to annealing. High resolution measurements show that bright and dim molecules remain after annealing; however, the pattern appears to have "reset", with only a few dim molecules appearing. This is consistent with the interpretation that the C_{60} molecules are undergoing a rotational order phase transition at room temperature. When the sample is heated, the molecules are all in the disordered rotor phase. As the sample cools to room temperature once again, dim molecules begin to appear.

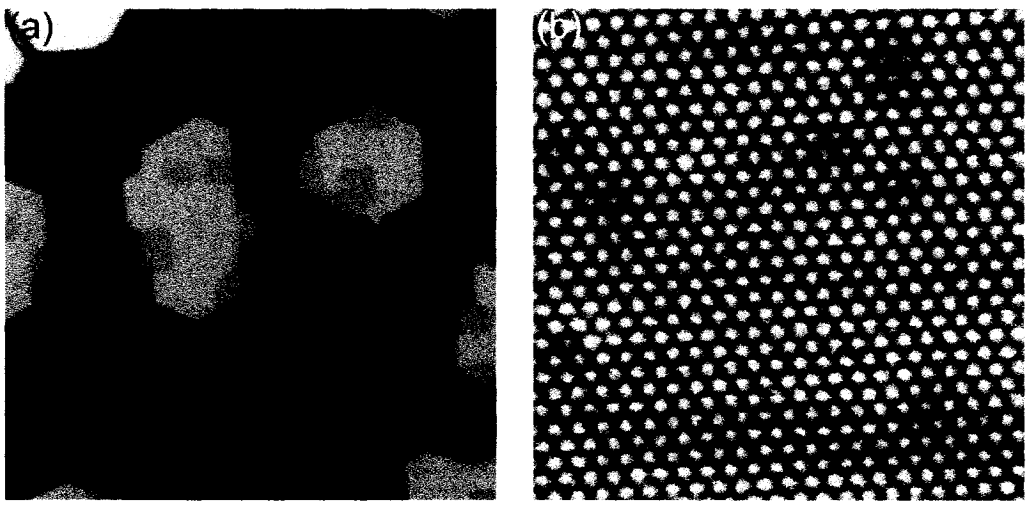

Figure 5.17: NC-AFM images of C_{60} on a nanostructured KBr (001) surface after annealing at 175 °C for 3 hours: (a) a 300 nm x 300 nm overview (Δf = 1.6 Hz), (b) a 20 nm x 20 nm molecular resolution image of third layer C_{60}, 4 hours after heating (Δf = -10.2 Hz).

5.3 Molecules and Metals on KBr (001)

In order to study the interactions between metals and molecules on an insulating surface, some experiments were performed where metals and molecules were both deposited onto a KBr (001) surface. This is not only important for characterizing the strength of the molecule-metal interactions, which play a key role in determining the transport behaviour of a molecular device [19, 90], but also for understanding how the interactions affect growth. The latter consideration is essential for devising a device fabrication roadmap. In this section, a few combinations of metals and molecules are considered.

In the first set of experiments, C_{60} was deposited prior to gold. As shown in Figure 5.18, away from the C_{60} islands, the gold grows in the usual way, i.e., nanoparticles are formed with separations of less than 50 nm. This is because the gold has a short diffusion length and only samples a small area of the substrate before a critical cluster size is reached.

Near the C_{60} islands, the gold interacts with the C_{60} and nucleates along the C_{60} island edges (see Figure 5.18 (b)). In addition, many protrusions are seen in the molecular islands. High resolution measurements show that the protrusions are made up of C_{60} molecules which are 0.26 ± 0.03 nm taller than the surrounding molecules. This height corresponds reasonably well with the height of a single atomic layer of gold; e.g., for the (111) plane, the height is 0.235 nm. Therefore, the gold which impinges on the C_{60} islands diffuses through the C_{60} lattice, probably through the interstices, and forms flat islands underneath or between the C_{60} layers. The protrusions are separated by only a few nanometers, implying a reduced diffusion of the gold through the C_{60}. Previous STM studies of gold growth on C_{60} films have shown similar protrusions which were attributed to the presence of intercalated gold [131].

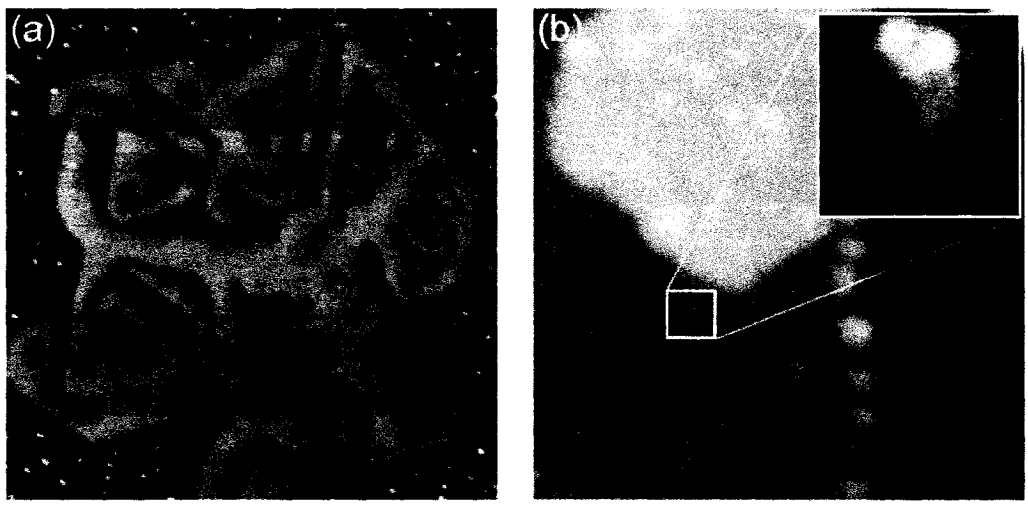

Figure 5.18: NC-AFM images of a KBr (001) surface after depositing 0.2 ML C_{60} followed by 0.02 nm Au: (a) 600 nm x 600 nm (Δf = -3.7 Hz), (b) 50 nm x 50 nm (Δf = -9.8 Hz).

In terms of design strategies for building molecule-based electronic devices, the diffusion of metal atoms into the molecular structures would clearly cause unwanted complications such as contamination and short circuits. Several experiments have been reported where

metals were deposited onto molecular films for producing vertical "sandwich" based devices [132, 133]. It is commonly assumed that simple layered structures are formed. However, it is clear, based on the current measurements, that atomic diffusion through the molecular layers is a distinct possibility, and must be taken into account. Otherwise the structures of the actual devices may differ substantially from the idealized model systems being considered.

Deposition in the reverse order, that is, metal then C_{60}, leads to very different structures. After depositing a small amount of C_{60} (0.001 ML) onto KBr (001) samples already covered with gold or palladium nanoparticles, many of the structures became about 1 nm taller and slightly larger (Figure 5.19). This suggests that the metal nanoparticles act as nucleation sites for the C_{60}. High resolution NC-AFM imaging confirms this picture. Figure 5.19 (b) shows a small palladium nanoparticle covered with 8-10 C_{60} molecules.

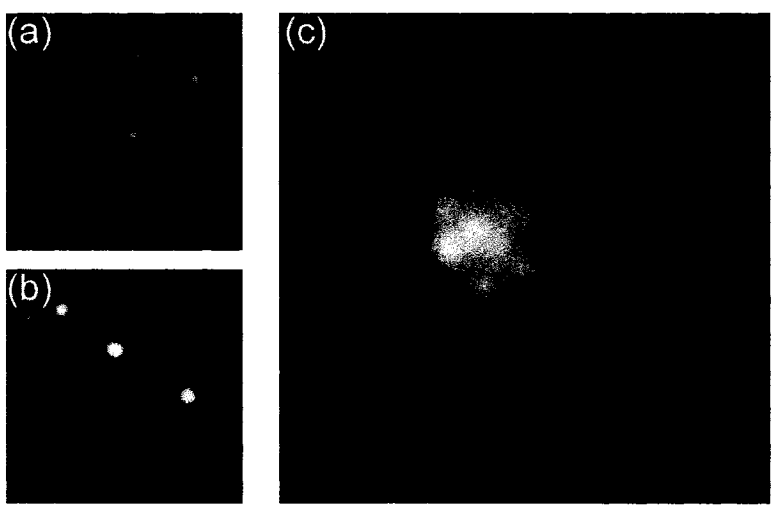

Figure 5.19: NC-AFM images (100 nm x 100 nm) of a KBr (001) surface after depositing (a) 0.001 nm Au (Δf = -5.0 Hz), and (b) 0.001 nm Au followed by 0.001 ML C_{60} (Δf = -5.2 Hz). The z-scale in both images is 2.2 nm. (c) High resolution 15 nm x 15 nm image of a metal-nucleated C_{60} cluster (0.001 nm Pd and 0.001 ML C_{60}, Δf = -3.9 Hz, with high pass and low pass filtering).

At higher C_{60} coverages (Figure 5.20), the nucleation of the C_{60} around the metal nanoparticles becomes increasingly evident. Many small compact C_{60} islands are formed with the spacing between the islands determined by that of the nucleating nanoparticles. These experiments were performed with gold, tantalum, and palladium nanoparticles. At the center of each island is a metal core. This can be seen in Figure 5.20 (d), where the buried palladium nanoparticle creates a small protrusion in the otherwise well ordered C_{60} lattice. An exception to this behaviour can be seen in Figure 5.20 (a). On areas where there is a high density of gold nanoparticles, such as at KBr steps, there are some bare nanoparticles. It is believed that this is caused by coalescence. The C_{60} initially nucleates around the gold structures; however, once the C_{60} islands come into contact with one another, the islands reshape in order to minimize their surface energy. The fact that this was observed for gold but not for tantalum or palladium nanoparticles indicates that the C_{60} - gold interaction is weaker than that for the other metals. In the cases of tantalum and palladium, the C_{60} is strongly bound such that the molecules cannot pull away from the nucleating centers during coalescence.

It was also observed that the size of the metal-nucleated C_{60} islands was fairly uniform. The size distribution for C_{60} islands nucleating around gold nanoparticles is shown in Figure 5.21. There are two peaks. The first corresponds to the mean island size. The second corresponds to cases where two islands are close together and are measured by the software (WSxM 3.0) as a single island; i.e., the measured area is two times the mean island size. The mean island size based on the first peak is 557 ± 8 nm^2, with a standard deviation of 110 nm^2. The second peak value, divided by two, is 535 ± 30 nm^2, with a standard deviation of 134 nm^2, in accordance with the island size determined from the first peak. The monodisperse size is a direct consequence of the nucleation at preferred sites. Because there is a high density of metal nucleation centers, the first molecules arriving at the surface do not have to diffuse very far before attaching to a metal site. As a result, the islands are all rapidly, nearly simultaneously, nucleated at the start of growth. Subsequent deposition leads to island expansion. In other words, the growth proceeds almost immediately in the pure growth regime (see Section 4.1).

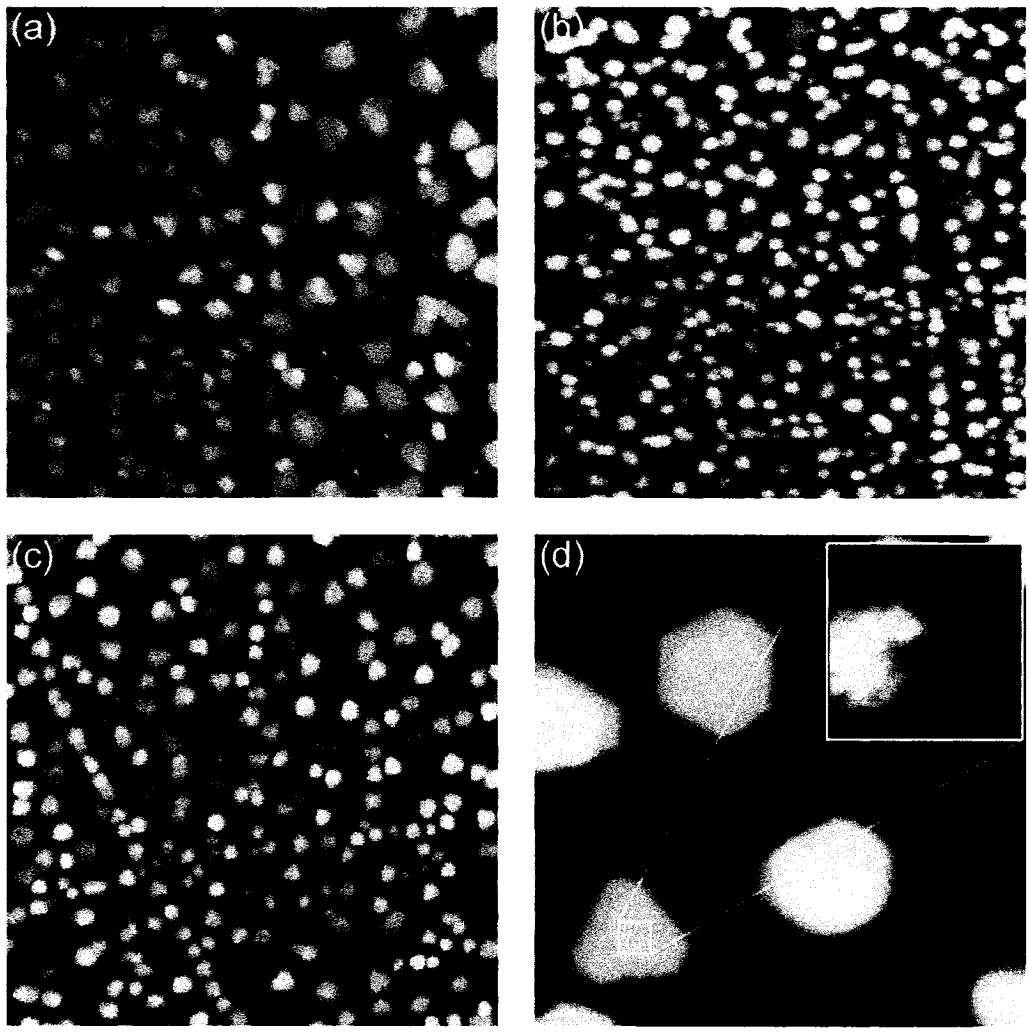

Figure 5.20: Overviews (600 nm x 600 nm) of KBr (001) samples with C_{60} nucleating around metal nanoparticles: (a) 0.005 nm Au, 0.6 ML C_{60} (Δf = -2.1 Hz), (b) 0.2 nm Ta, 0.6 ML C_{60} (Δf = -5.1 Hz), (c) 0.04 nm Pd, 0.6 ML C_{60} (Δf = -2.0 Hz). (d) A close-up (100 nm x 100 nm) of several islands. The inset shows a protrusion at the center of an island, where a nucleating nanoparticle is buried (0.04 nm Pd, 0.6 ML C_{60}, Δf = -3.3 Hz).

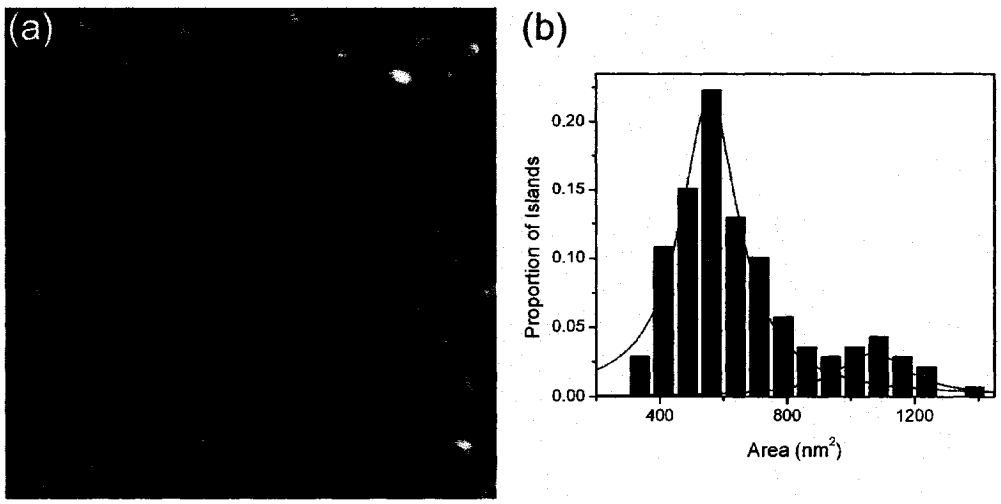

Figure 5.21: (a) NC-AFM image (600 nm x 600 nm) of C_{60} islands formed around Au nanoparticles (0.005 nm Au, 0.6 ML C_{60}, Δf = -2.4 Hz), and (b) the corresponding island size distribution.

The nucleation around the metal nanostructures can be explained by the relative strengths of the interactions at play. The molecule-substrate interaction is weak, as evidenced by the long diffusion length of the C_{60} on the KBr (001) surface. Conversely, the interaction between C_{60} and most metals is quite strong. For example, C_{60}-induced surface reconstructions have been observed on Ag (001) [103], Cu (111) [104], Au (110), Pd (110), and Ni (110) surfaces [102]. On the Au (111) surface, the 23 x $\sqrt{3}$ reconstruction which is normally present is lifted by adsorbed C_{60} [105]. Recent density functional theory calculations have characterized the interaction between C_{60} and gold as mainly covalent in nature [134]; i.e., the molecules are chemisorbed to the metals, with the bonding involving shared electrons.

The anchoring of molecules around metal structures is potentially useful for controlling the position of molecules on an insulating surface. Moreover, for building molecule-based devices, it is expected that C_{60}, and most likely other molecules as well, would "self-assemble" into a pre-existing electrode gap and form a robust bond with the

electrodes. This is because the deposited molecules, which are weakly physisorbed to the substrate, freely diffuse and sample large areas of the surface until the metal structures are encountered. The strong coupling between the molecules and electrodes is not only structurally important, but is also necessary for ensuring a good electrical contact with the molecule [135].

Some preliminary experiments were performed with PTCDA molecules as well. Figure 5.22 shows that the PTCDA molecules deposited after gold do not strongly bind to the gold. This is consistent with STM measurements which show that the PTCDA-gold interaction is quite weak [94, 101]. On the Au (111) surface, PTCDA growth does not remove the 23 x $\sqrt{3}$ gold reconstruction [101], as C_{60} does. Nevertheless, it is known that PTCDA does interact strongly with some metals, such as Cu [100], and it is expected that preferential nucleation around these metals would occur.

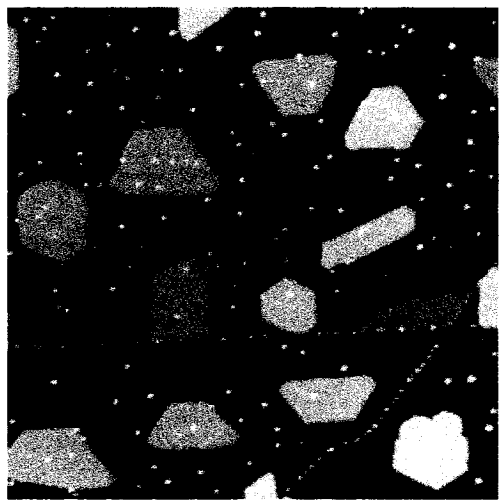

Figure 5.22: Au followed by PTCDA deposition on KBr (001), 600nm x 600 nm (Δf = -3.7 Hz).

5.4 Molecules and Metals on Nanostructured KBr (001)

Molecules can also be placed in close proximity to metal nanostructures by using monatomic-depth rectangular pits. Figure 5.23 shows an example where the sample was prepared by depositing gold and then PTCDA onto a nanostructured KBr (001) surface. As shown in Section 4.2.3, the gold nucleates predominantly at the pit corners, on top of the steps. The PTCDA, as seen in Section 5.2.1, becomes trapped inside some of the pits. Because the PTCDA interacts weakly with gold, the gold does not interfere with the PTCDA growth. However, since the PTCDA is not chemically bound to the gold, the molecules are expected to have a weak electrical coupling with the adjacent metal nanoparticles. Low temperature transport measurements in the weak coupling regime can potentially be used to study single electron tunnelling, and Coulomb blockade behaviour, where electrons must overcome a charging barrier in order to tunnel into the molecular energy levels.

For building a molecular device, the metal nanoparticles may serve as nanoscopic contact pads for the molecular crystallites. A technique such as shadow mask deposition [72] or field emission from an AFM tip [136] may be used to connect the contact pads to larger scale electrodes. Furthermore, in future experiments, the nanoparticles can be made larger by depositing more metal, making the problem of interfacing with the system a matter of contacting a 20-40 nm structure rather than a 1-10 nm structure. The spacing of the nanoparticles, and the number of molecules trapped between them, is controlled by the pit size which can be readily varied (Section 3.3). For studying the structure-function relationship in such a device, it was shown in Section 5.2.1 that the positions of the molecules can be measured by NC-AFM. In addition, the nanoparticles have well-defined crystal structures which can be characterized by TEM (Section 4.2). A well-defined system structure is desirable for stringent comparisons with modeling, which shows that the detailed structure of the device, and in particular the molecule-electrode interface, is of primary importance [19, 20].

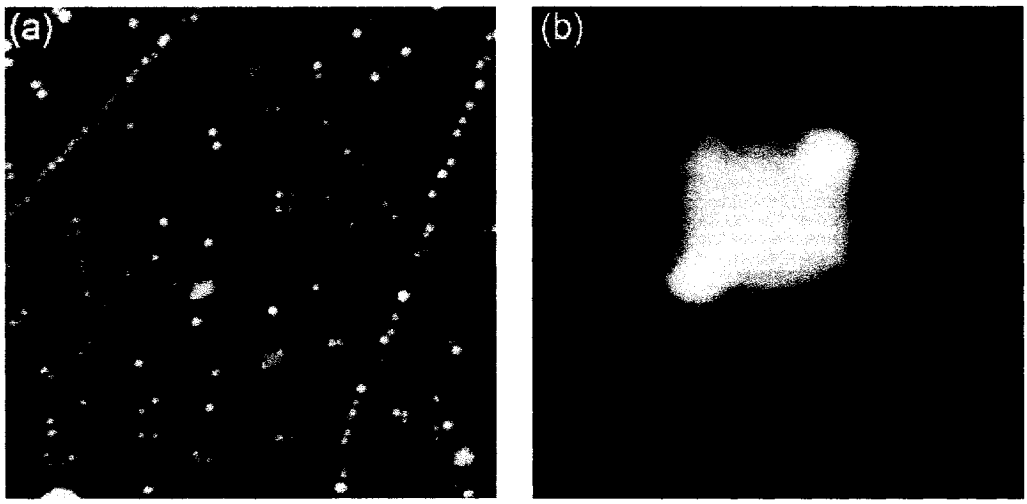

Figure 5.23: NC-AFM images showing PTCDA molecules trapped inside pits, with Au nanoparticles at the pit corners (a) 300 nm x 300 nm (Δf = -1.6 Hz), (b) 40 nm x 40 nm (Δf = -3.2 Hz). Sample preparation conditions: Au source, 0.36 ± 0.03 μ C/cm^2 at 423 K; 0.005 nm Au; 0.1ML PTCDA.

5.5 Conclusions

It was demonstrated in this section that the growth of molecules on a KBr (001) surface can be drastically modified by the presence of nanostructured pits and metal nanoparticles.

Nanometer-scale PTCDA crystallites were produced by trapping the molecules inside pits. Most of the islands were 3 - 4 layers high. However, some 1 - 2 layer islands were stabilized in pits with side lengths smaller than 10 nm. High resolution NC-AFM images showed the herringbone arrangement of the molecules and a 4.0 ± 0.5 ° deviation from the <100> direction of the substrate. The observed molecule-substrate lattice mismatch and the heights of the crystallites indicate a strain in the first two PTCDA layers, which is relieved by the third layer, where the bulk β-phase lattice constants were measured. During high resolution imaging, some streaks were observed on top of the islands. These signatures of molecular diffusion were used to estimate a hopping frequency of

$27 \pm 2\ s^{-1}$ and a diffusion barrier of 0.7 ± 0.2 eV for a PTCDA molecule on top of a PTCDA island. Furthermore, the specificity of the molecule-substrate interactions provided a new method for identifying the imaged substrate sublattice. In the case considered here, the maxima were identified as K^+ ions. Also, by using sufficiently large frequency shifts during imaging, it was possible to manipulate the PTCDA molecules out of pits.

The deposition of C_{60} molecules on nanostructured KBr (001) surfaces did not lead to molecular trapping; nevertheless, the molecules were observed to align with the <100> substrate directions. High resolution NC-AFM measurements showed that the C_{60} lattice is compressed and has a 13 x 3 coincident overlayer structure. The high resolution measurements also showed a peculiar pattern of bright and dim molecules, which exhibited height differences of 0.021 - 0.076 nm. It was found that the number of dim molecules increased with time until stabilizing at about 50 % after 48 hours. In addition, the maximum height differences were higher in upper C_{60} layers. Several mechanisms such as interface effects, buckling, and molecular orientations were considered. It was inferred that the height differences are of geometric origin, most likely due to the molecules undergoing a phase transition where the molecules become orientationally ordered. The ordered molecules have a lower height than the freely rotating ones. This interpretation is supported by the measurements of an annealed sample which showed a decrease in the number of dim molecules following heating. The annealed sample also had more compact islands than before annealing, indicating that the initial island structures are metastable.

The deposition of molecules and metals in sequence showed that the order of deposition and the strength of the molecule-metal interaction are of utmost importance in determining the nature of the growth. When C_{60} was deposited prior to gold, the gold diffused into or under the C_{60} layers. This is not ideal for device fabrication and indicates that the deposition of metals after molecules should be avoided. Deposition in the reverse order provided a means of gauging the relative strengths of the molecule-metal interactions: strongly interacting pairs (C_{60}-Au, C_{60}-Ta, and C_{60}-Pd) showed nucleation of

the molecules around the metals, and weakly interacting pairs (PTCDA-Au) grew nearly independently. The interaction between C_{60} and gold was somewhat weaker than with other metals. This was evident in areas with high densities of gold nanoparticles, where the C_{60} islands coalesced and uncovered some of the gold structures. In the case of strong molecule-metal interactions, molecular islands were formed with metal nanoparticles at the center. Because of the nearly simultaneous nucleation of the islands, the island sizes were fairly uniform. The nucleation of molecules around metal structures is potentially useful for positioning molecules around electrodes and for obtaining a strong electrical coupling with the electrodes.

Finally, despite the weak interaction between PTCDA and gold, it was demonstrated that PTCDA molecules can be positioned in close proximity to gold nanoparticles by using nanostructured pits as templates. The gold nanoparticles nucleate at the corners of the steps, on the top of the steps, and the PTCDA becomes trapped inside some of the pits.

The above methods for positioning molecules on an insulator are promising, and may be useful for assembling a molecular device. For example, the monatomic depth pits may be used to control the spacing of metal nanoparticles which are used as both contact pads to the molecules and for nucleating the growth of molecules.

6 Conclusions and Outlook

The study of insulating surfaces at the atomic scale is a nascent field. In the present work, NC-AFM was applied to investigating the creation of pits (Chapter 3), the growth of metals (Chapter 4), and the templated growth of molecules (Chapter 5) on the KBr (001) surface. These measurements demonstrate the utility of NC-AFM for providing atomic and molecular scale structural information which is otherwise inaccessible by other techniques. What follows is a summary of the main results and a brief look at directions for future experiments aimed at building molecular electronic devices.

Firstly, it was demonstrated that an electron beam evaporator can be used as a source of charge for creating monatomic depth rectangular pits in a KBr surface. The new technique provides very small current densities, less than 200 pA/cm^2, making it possible to precisely control the dose of charge reaching sample. It was shown that the size of the pits can be tuned by varying the dose of charge. In addition, the pit number density can be adjusted by using different temperatures during charge irradiation. The pits created at substrate temperatures of 150 ^{o}C and above preserved the structure of the KBr lattice. However, pits prepared at room temperature contained protrusions which are believed to be alkali atoms left over from the preferential non-thermal desorption of halogen atoms.

Next, the growth of three metals on a KBr (001) surface was considered: gold, tantalum, and palladium. It was shown that despite the use of a charge deviating grid, the charge emitted by the evaporator during deposition had a significant effect on the growth. For the gold growth, the number density of nanoparticles followed nearly the same temperature dependence as the pits, with the respective systems exhibiting activation energies of 0.075 ± 0.018 eV and 0.072 ± 0.012 eV. Using atomistic nucleation theory, the diffusion energy of gold on KBr was determined to be 0.26 ± 0.06 eV. Although this is in agreement with previous TEM and theoretical studies, it does not take into account the influence of charge-induced desorption on the metal nucleation. Future work must

either include the preferred defect sites in the modeling, or use a specially designed evaporator which provides the sample with better shielding from charge. The effect of charge during growth was also seen in the tantalum system where pits surrounded the nanoparticles prepared at 250 °C. The small size and low desorption efficiency reflects an obstruction of the pit expansion by the nanoparticles. In addition, the number density of pits was double that in pitted KBr samples created with the same dose of charge. This suggests that the nanoparticles nucleate the pits. Because the nanoparticles also preferentially nucleate at defects such as steps, the processes of nanoparticle and pit nucleation appear to be intertwined and complex. In addition, it was demonstrated that the pits can be used to template the growth of metals. The deposition of gold onto a pitted surface resulted in the preferential nucleation of nanoparticles at the pit corners.

The three metals exhibited different growth morphologies. The gold nanoparticles were quite tall, with the height steadily increasing with coverage. Some of the nanoparticles were multiply twinned particles and others were <110> oriented epitaxial particles. In accordance with earlier studies, at higher temperatures, the proportion of epitaxial particles increased. In contrast, the tantalum grew as fractal islands. The nanoparticles were about 3 times shorter than the gold islands, indicating a stronger interaction with the substrate. Moreover, the tantalum interacted strongly with the KBr steps, leading to extensive step decoration and nearly continuous nanowire structures. The palladium growth resulted in the formation of nanoparticles as well as KBr islands and gradually protruding areas in the substrate. It is expected that the latter structures are caused by the interdiffusion of some palladium under the KBr surface. In terms of building patterned metal structures on a KBr surface, the tantalum nanoparticles exhibited the most favourable characteristics. Future experiments should investigate whether continuous tantalum nanowires can be produced by evaporating through a shadow mask.

As for molecular growth, it was demonstrated that the presence of pits and metal nanostructures can have an important effect. Monatomic depth rectangular pits were used to trap PTCDA molecules and form nanometer-scale crystallites. The PTCDA lattice was also observed to nearly align with the <100> direction of the substrate, showing only a

4.0 ± 0.5° deviation. Similar experiments with C_{60} molecules did not result in molecular trapping; however, the molecules did align with the <100> directions of the substrate. Simultaneous high resolution measurements of adjacent molecule and substrate lattices made it possible to use the substrate lattice as a reference in determining the molecular lattice constants. The PTCDA molecules were arranged in a herringbone pattern, while the C_{60} molecules were in a close-packed arrangement. Both structures are similar to known bulk structures formed by the respective molecules. In the PTCDA system, the attraction of the molecule's oxygen groups to K^+ surface ions of the substrate made it possible to identify the imaged substrate lattice. In addition, streaks during NC-AFM imaging, caused by diffusing molecules, were used to estimate the hopping frequency and diffusion barrier for PTCDA diffusion on top of a PTCDA island. High resolution measurements of the C_{60} system also showed some interesting behaviour. Patterns of bright and dim molecules were observed, with the proportion of dim molecules increasing with time. It was determined that the cause of the height difference between the two types of molecules was of geometric origin, and most likely caused by the molecules undergoing a phase transition from a state of rotational disorder to rotational order.

The sequential growth of molecules and metals showed that the order of deposition and the strength of the interaction between the molecule and metal are both important in determining the resultant structures. The deposition of C_{60} before gold led to the diffusion of gold through the C_{60} layer. Deposition in the reverse order led to the nucleation of the molecules around the metal structures, in cases where the molecule-metal interactions are sufficiently strong. This was observed for C_{60} with gold, tantalum, and palladium. On the other hand, PTCDA did not nucleate around gold nanoparticles, indicating a weak molecule-metal interaction. Despite this weak interaction, it was possible to place PTCDA in close proximity to gold nanoparticles by decorating pits with gold and then trapping PTCDA inside the pits.

The above results have important implications insofar as constructing a molecular device is concerned. First, to avoid the interdiffusion of metals into the molecular layers, the molecules should be deposited after the metals. In addition, it was shown that molecules

can be positioned on the substrate in two ways: in cases where the molecules interact sufficiently strongly with the substrate steps, the molecules can be trapped inside pits, and in cases where the molecules interact strongly with a given metal, the metal can be used to nucleate the growth of the molecule. Furthermore, the pits can be used as templates for positioning metals at the pit corners.

Based on these observations, the following device fabrication sequence is proposed (Figure 6.1): First, create pits in an atomically flat KBr (001) surface. Next, deposit a metal, such as gold, so that the corners of the pits are decorated. The resulting nanoparticles will be used as contact pads to the molecules. The size of the pits, which can easily be tuned, defines the spacing of the contact pads, and hence the size of the molecular device. It is likely that the first devices constructed will have tens or hundreds of molecules, but in principle, this approach can be applied to smaller structures. In order to facilitate contacting the structures, the metal nanoparticles can be several nanometers in size. Next, the mesoscopic electrodes, which connect the nanoparticles to macroscopic leads, should be deposited. At present, the deposition of the mesoscopic wires remains the greatest challenge in fabricating the device. There are two main options for creating the electrodes: the deposition of a metal through a stencil mask [72], or the field emission of metal from a metal coated AFM tip [136]. Both techniques are currently under development in our lab. Finally, the molecules can be deposited on the surface. As shown in Chapter 5, molecules which interact weakly with the substrate will diffuse over a long distance until they are trapped at a pit or metal structure. The molecules can be engineered to assemble in the desired manner. For example, a polar molecule with a size which matches the periodicity of the substrate lattice may interact strongly with the KBr steps and be efficiently trapped inside the pits. Alternatively, a thiolated molecule can be used for a robust connection to the electrodes.

Finally, once the device is constructed, the primary goal is to study the relationship between structure and function. As shown in section 5.2, the positions of the molecules can be measured by NC-AFM. So far, it has not been possible to measure the atomic positions in metal nanostructures by NC-AFM. However, it was shown in Section 4.2 that

the crystallographic structure of the nanoparticles can be measured by *ex situ* TEM. Therefore, after measuring the electrical properties and molecular structure of the device *in situ*, the sample can be removed from UHV and the electrode structure determined by TEM. Alternatively, a different combination of metal and insulator may produce flatter nanoparticles which are more easily imaged by NC-AFM. In this case, the entire process of device fabrication and characterization may be done entirely under UHV conditions.

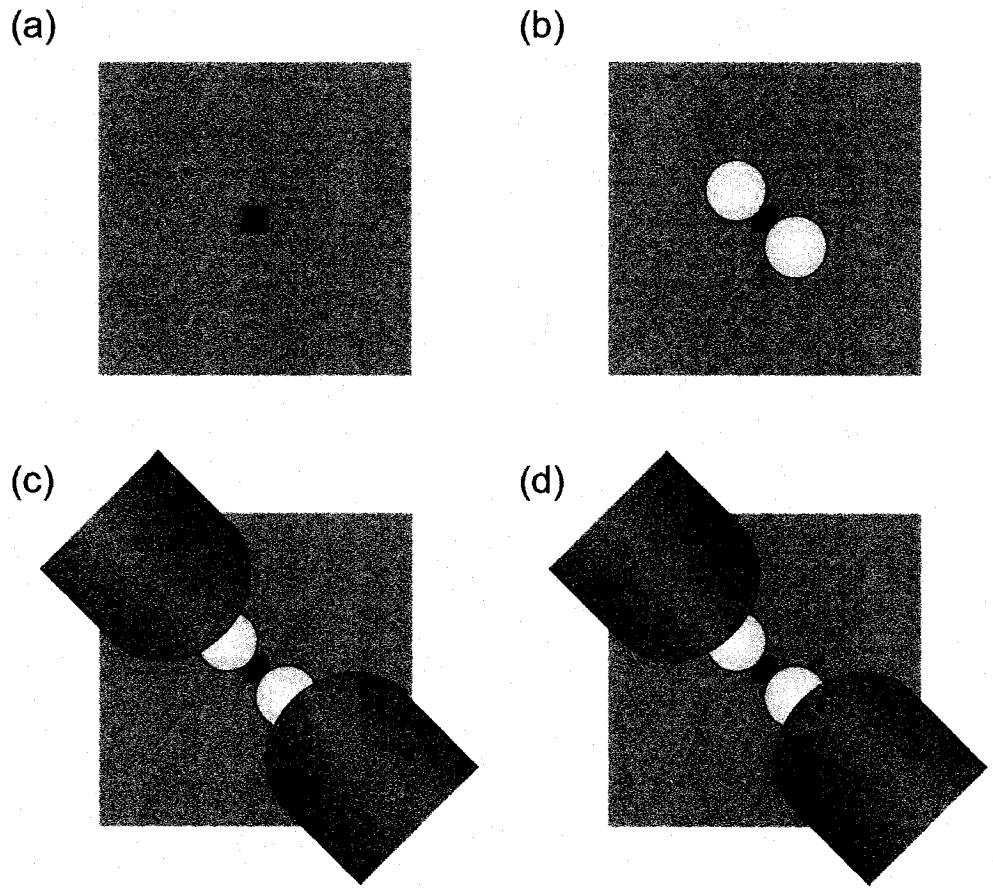

Figure 6.1: Diagram of the proposed device fabrication sequence: (a) create pits, (b) decorate the pit corners with metal nanoparticles, (c) connect the metal nanoparticles to contact electrodes, and (d) deposit the molecules.

Appendix A: Evaporator Port Schematics

A custom built port was designed for the UHV system in order to accommodate the electron beam evaporator and the molecule evaporator. Schematics of the port are shown in Figures A.1 and A.2. The port consists of 6 smaller ports. The ports for the evaporators point towards the central axis of the preparation chamber. This allows the sample to be oriented normal to either evaporator beam. The sample storage carousel which is housed in the sample preparation chamber is used to rotate the sample to face either evaporator. The view port, labelled 3 in Figure A.1, also faces the central axis of the chamber. This port is often used for monitoring sample cleavage and was also used for the optical pyrometer measurements shown in Section 2.3.1. In addition, three extra ports were included for future expansion of the system. Port 4 faces the center of the preparation chamber. Ports 5 and 6 are oriented parallel to ports 1 and 2, respectively. These can potentially be useful for aligning shadow masks with the evaporators.

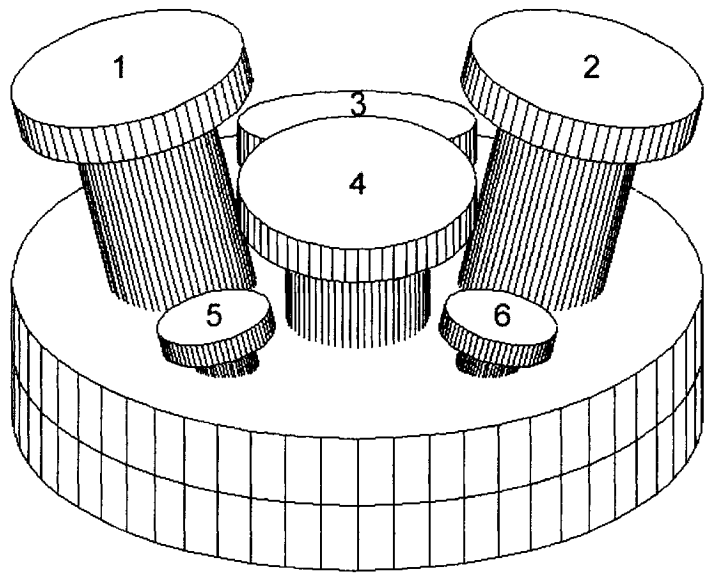

Figure A.1: A 3-dimensional illustration of the custom built evaporator port. The labelled ports are: 1. the electron beam evaporator port, 2. the view port, 3. the molecule evaporator port, 4-6. ports for future expansion.

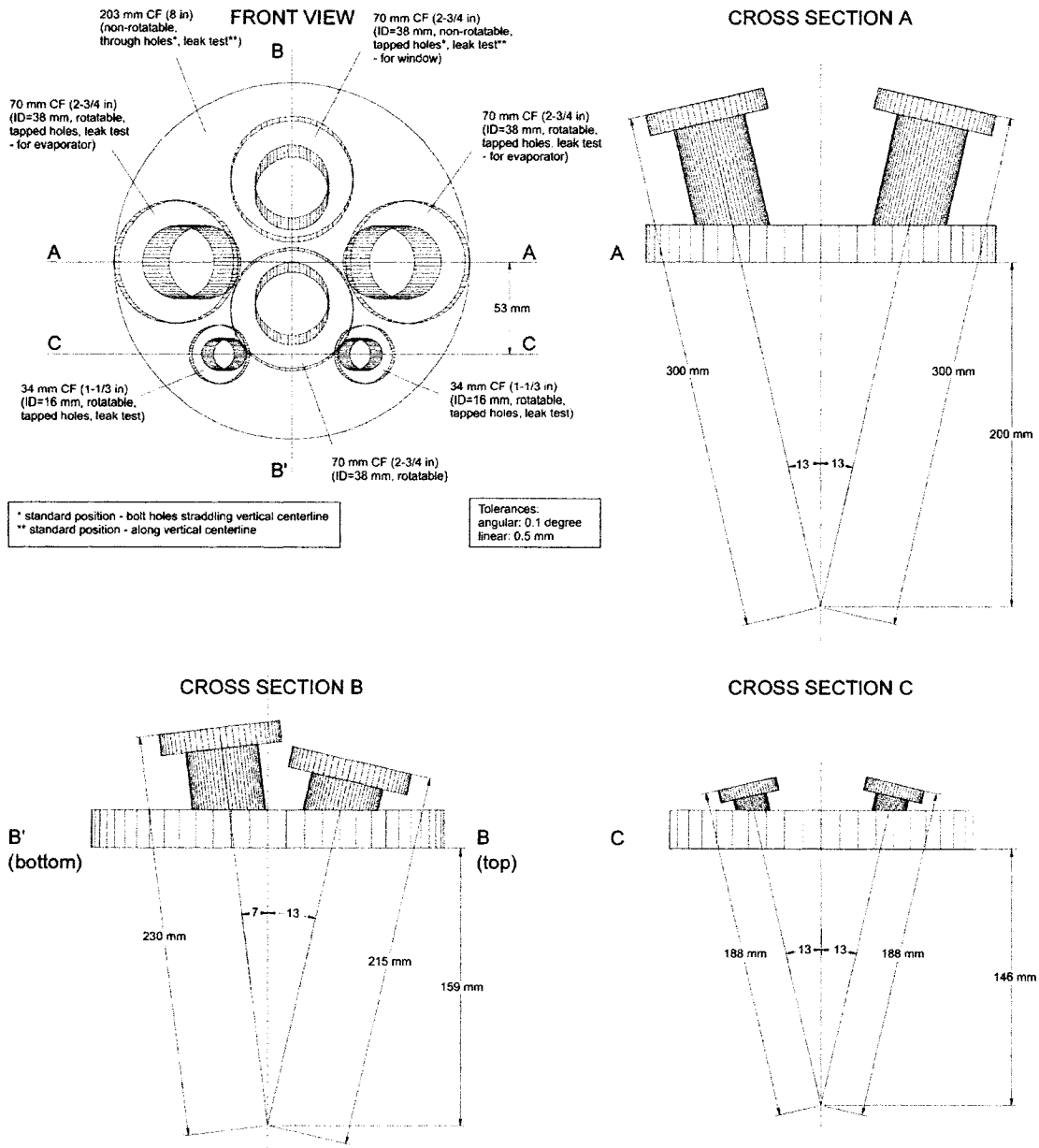

Figure A.2: Schematic showing front and cross sectional views of the custom built evaporator port.

Appendix B: Electron Beam Evaporator Calibration

The electron beam evaporator is equipped with an ion current collector which can be used to measure the evaporation rate. For all of the experiments presented in this thesis, the evaporation rate was verified with the quartz crystal microbalance prior to each deposition. Nevertheless, the ion current is still sometimes useful for real-time rate monitoring. The ion current was calibrated with the quartz crystal monitor. Figure A.3 shows the deposition rate as a function of the ion collector current for gold, tantalum, and palladium.

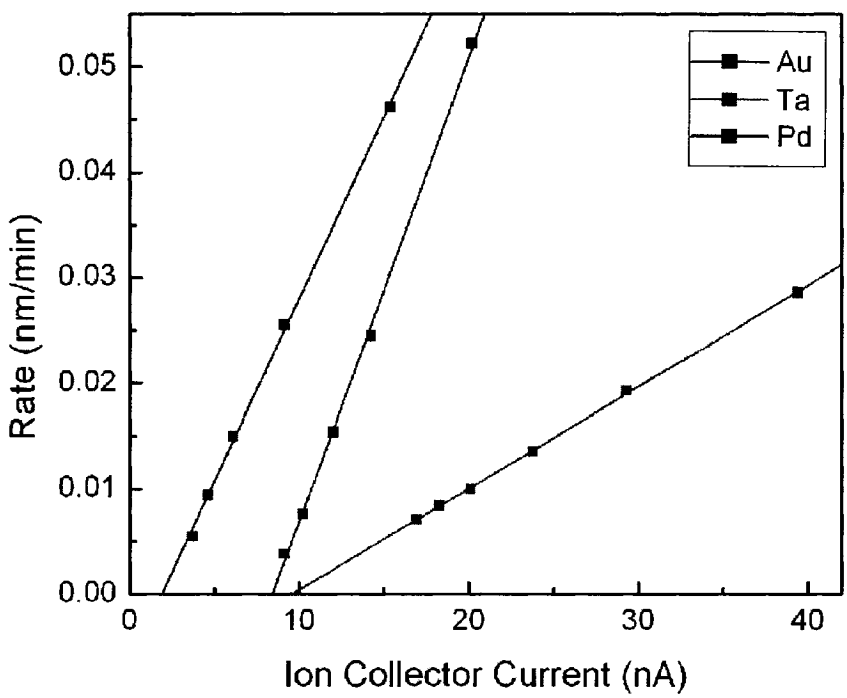

Figure A.3: The deposition rate as a function of the electron beam evaporator ion collector current for gold, tantalum, and palladium.

The charge emitted by the evaporator was measured for all three metals as well. Figure A.4 shows the current density divided by power as a function of sample voltage. Each curve represents an average of at least 4 data sets, taken at different powers. As described in Section 3.2, these plots can be used to determine the current density for any applied power.

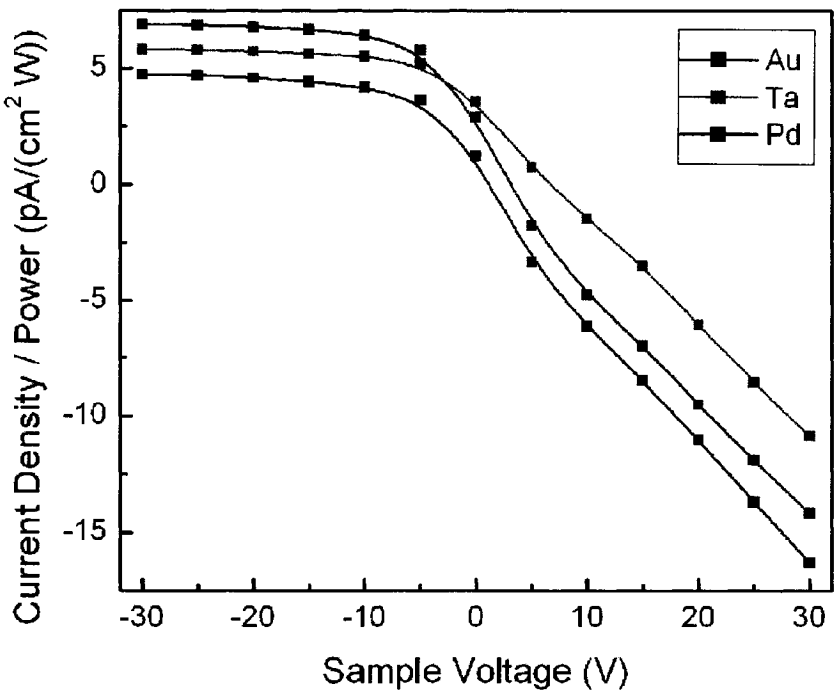

Figure A.4: The current density/power emitted during evaporation of gold, tantalum, and palladium, as a function of the sample voltage.

References

[1] K. Oura, *Surface science : an introduction* (Springer, Berlin ; New York, 2003).

[2] E. Meyer, H. J. Hug, and R. Bennewitz, *Scanning probe microscopy : the lab on a tip* (Springer, Berlin ; New York, 2004).

[3] T. R. Albrecht, P. Grutter, D. Horne, and D. Rugar, Journal of Applied Physics **69**, 668 (1991).

[4] S. Kitamura and M. Iwatsuki, Japanese Journal of Applied Physics Part 2-Letters **34**, L145 (1995).

[5] F. J. Giessibl, Science **267**, 68 (1995).

[6] M. Bammerlin, R. Luthi, E. Meyer, A. Baratoff, J. Lu, M. Guggisberg, et al., Applied Physics a-Materials Science & Processing **66**, S293 (1998).

[7] R. Bennewitz, S. Schar, V. Barwich, O. Pfeiffer, E. Meyer, F. Krok, et al., Surface Science **474**, L197 (2001).

[8] S. Orisaka, T. Minobe, T. Uchihashi, Y. Sugawara, and S. Morita, Applied Surface Science **140**, 243 (1999).

[9] C. Loppacher, M. Bammerlin, M. Guggisberg, S. Schar, R. Bennewitz, A. Baratoff, et al., Physical Review B **62**, 16944 (2000).

[10] S. A. Burke, *Buckminsterfullerene on KBr studied by High Resolution NC-AFM: Molecular nucleation and growth on an insulator* (MSc Thesis, McGill University, 2004).

[11] L. Nony, E. Gnecco, A. Baratoff, A. Alkauskas, R. Bennewitz, O. Pfeiffer, et al., Nano Letters **4**, 2185 (2004).

[12] S. Morita, R. Wiesendanger, and E. Meyer, *Noncontact atomic force microscopy* (Springer, Berlin ; New York, 2002).

[13] A. Aviram and M. A. Ratner, Chemical Physics Letters **29**, 277 (1974).

[14] C. Joachim, J. K. Gimzewski, and A. Aviram, Nature **408**, 541 (2000).

[15] Y. Wada, M. Tsukada, M. Fujihira, K. Matsushige, T. Ogawa, M. Haga, et al., Japanese Journal of Applied Physics Part 1-Regular Papers Short Notes & Review Papers **39**, 3835 (2000).

[16] X. D. Cui, A. Primak, X. Zarate, J. Tomfohr, O. F. Sankey, A. L. Moore, et al., Science **294**, 571 (2001).

[17] H. Park, J. Park, A. K. L. Lim, E. H. Anderson, A. P. Alivisatos, and P. L. McEuen, Nature **407**, 57 (2000).

[18] R. L. McCreery, Chemistry of Materials **16**, 4477 (2004).

[19] B. Larade, J. Taylor, H. Mehrez, and H. Guo, Physical Review B **64**, 075420 (2001).

[20] J. J. Palacios, A. J. Perez-Jimenez, E. Louis, and J. A. Verges, Physical Review B **64**, 115411 (2001).

[21] M. Guggisberg, M. Bammerlin, C. Loppacher, O. Pfeiffer, A. Abdurixit, V. Barwich, et al., Physical Review B **61**, 11151 (2000).

[22] J. Daintith and Facts on File Inc., *The Facts on File dictionary of chemistry* (Facts On File Publications, New York, N.Y., 1988).

[23] G. Binnig, H. Rohrer, C. Gerber, and E. Weibel, Physical Review Letters **50**, 120 (1983).

[24] J. M. Mativetsky, S. A. Burke, R. Hoffmann, Y. Sun, and P. Grutter, Nanotechnology **15**, S40 (2004).

[25] J. Tamayo, Journal of Applied Physics **97**, 044903 (2005).

[26] D. Rugar, C. S. Yannoni, and J. A. Sidles, Nature **360**, 563 (1992).

[27] Y. Hasegawa, T. Eguchi, T. An, M. Ono, K. Akiyama, and T. Sakurai, Japanese Journal of Applied Physics Part 2-Letters **43**, L303 (2004).

[28] M. A. Lantz, H. J. Hug, R. Hoffmann, P. J. A. van Schendel, P. Kappenberger, S. Martin, et al., Science **291**, 2580 (2001).

[29] R. Hoffmann, L. N. Kantorovich, A. Baratoff, H. J. Hug, and H. J. Guntherodt, Physical Review Letters **92**, 146103 (2004).

[30] J. W. Rohlf, *Modern Physics from A to Z* (John Wiley, New York, 1994).

[31] Raytek, (Emissivity of most common materials, http://www.raytek-northamerica.com/cat.html?cat_id=9.5, 2006).

[32] Chino pyrometer instruction manual.

[33] Private communication with Georg Woltersdorf.

[34] D. P. Woodruff and T. A. Delchar, *Modern techniques of surface science* (Cambridge University Press, Cambridge ; New York, 1994).

[35] R. Hoffmann, M. A. Lantz, H. J. Hug, P. J. A. van Schendel, P. Kappenberger, S. Martin, et al., Applied Surface Science **188**, 238 (2002).

[36] R. Hoffmann, *Magnetic and Interatomic Forces Measured by Low Temperature Scanning Force Microscopy* (PhD Thesis, University of Basel, 2001).

[37] G. A. Bassett, Philosophical Magazine **3**, 1042 (1958).

[38] M. Szymonski, J. Kolodziej, B. Such, P. Piatkowski, P. Struski, P. Czuba, et al., Progress in Surface Science **67**, 123 (2001).

[39] N. H. Tolk, M. M. Traum, J. C. Tully, and T. E. Madey, *Desorption Induced by Electronic Transitions I* (Springer, Berlin, 1983).

[40] M. Goryl, B. Such, F. Krok, K. Meisel, J. J. Kolodziej, and M. Szymonski, Surface Science **593**, 147 (2005).

[41] H. Hoche, J. P. Toennies, and R. Vollmer, Physical Review B **50**, 679 (1994).

[42] F. Krok, J. J. Kolodziej, B. Such, P. Czuba, P. Piatkowski, P. Struski, et al., Nuclear Instruments & Methods in Physics Research Section B-Beam Interactions with Materials and Atoms **226**, 601 (2004).

[43] V. Puchin, A. Shluger, Y. Nakai, and N. Itoh, Physical Review B **49**, 11364 (1994).

[44] B. Such, P. Czuba, P. Piatkowski, and M. Szymonski, Surface Science **451**, 203 (2000).

[45] M. Szymonski, J. Kolodziej, P. Czuba, P. Piatkowski, A. Poradzisz, N. H. Tolk, et al., Physical Review Letters **67**, 1906 (1991).

[46] A. L. Shluger and K. Tanimura, Physical Review B **61**, 5392 (2000).

[47] J. J. Kolodziej, B. Such, P. Czuba, F. Krok, P. Piatkowski, P. Struski, et al., Surface Science **482**, 903 (2001).

[48] R. M. Wilson and R. T. Williams, Nuclear Instruments & Methods in Physics Research Section B-Beam Interactions with Materials and Atoms **101**, 122 (1995).

[49] H. Bethge, Physica Status Solidi **2**, 775 (1962).

[50] R. O. Jenkins and W. G. Trodden, *Electron and ion emission from solids by R.O. Jenkins and W.G. Trodden* (Routledge & K. Paul, London, 1965).

[51] T. J. M. Boyd and J. J. Sanderson, *Plasma dynamics* (Nelson, London, 1969).

[52] I. H. Hutchinson, *Principles of plasma diagnostics* (Cambridge University Press, Cambridge ; New York, 2002).

[53] CRC, *CRC Handbook of Chemistry and Physics* (CRC Press LLC, Boca Raton, FL, 2005).

[54] I. S. Grigoriev and E. Z. Meilikhov, *Handbook of physical quantities* (CRC Press, Boca Raton, 1997).

[55] L. R. Bedell and H. E. Farnsworth, Surface Science **41**, 165 (1973).

[56] J. G. Amar and F. Family, Thin Solid Films **272**, 208 (1996).

[57] H. Brune, Surface Science Reports **31**, 121 (1998).

[58] M. Szymonski, T. Tyliszczak, P. Aebi, and A. P. Hitchcock, Surface Science **271**, 287 (1992).

[59] J. Venables, *Introduction to surface and thin film processes* (Cambridge University Press, Cambridge, UK ; New York, 2000).

[60] S. Ogawa and S. Ino, Journal of Crystal Growth **13**, 48 (1971).

[61] H. Brune, C. Romainczyk, H. Roder, and K. Kern, Nature **369**, 469 (1994).

[62] Y. Chen, D. A. A. Ohlberg, G. Medeiros-Ribeiro, Y. A. Chang, and R. S. Williams, Applied Physics a-Materials Science & Processing **75**, 353 (2002).

[63] H. Brune, M. Giovannini, K. Bromann, and K. Kern, Nature **394**, 451 (1998).

[64] T. Michely and J. Krug, *Islands, mounds, and atoms : patterns and processes in crystal growth far from equilibrium* (Springer, Berlin ; New York, 2004).

[65] J. V. Barth, Surface Science Reports **40**, 75 (2000).

[66] J. A. Venables, Surface Science **300**, 798 (1994).

[67] J. A. Venables, G. D. T. Spiller, and M. Hanbucken, Reports on Progress in Physics **47**, 399 (1984).

[68] J. H. Harding, A. M. Stoneham, and J. A. Venables, Physical Review B **57**, 6715 (1998).

[69] K. Hojrup-Hansen, S. Ferrero, and C. R. Henry, Applied Surface Science **226**, 167 (2004).

[70] G. Haas, A. Menck, H. Brune, J. V. Barth, J. A. Venables, and K. Kern, Physical Review B **61**, 11105 (2000).

[71] C. Barth and C. R. Henry, Nanotechnology **15**, 1264 (2004).

[72] P. Zahl, M. Bammerlin, G. Meyer, and R. R. Schlittler, Review of Scientific Instruments **76**, 023707 (2005).

[73] H. Bethge, in *Interfacial aspects of phase transformations : proceedings of the NATO Advanced Study Institute, held at Erice, Sicily, August 29-September 9, 1981*, edited by B. Mutaftschiev (D. Reidel Pub. Co., Dordrecht, Holland 1982), p. 669.

[74] K. Yamamoto, T. Iijima, T. Kunishi, K. Fuwa, and T. Osaka, Journal of Crystal Growth **94**, 629 (1989).

[75] S. Giorgio, C. Chapon, C. R. Henry, G. Nihoul, and J. M. Penisson, Philosophical Magazine a-Physics of Condensed Matter Structure Defects and Mechanical Properties **64**, 87 (1991).

[76] A. Panov, H. Haefke, and M. Krohn, Journal of Crystal Growth **58**, 452 (1982).

[77] H. Sato and Shinozak.S, Surface Science **22**, 229 (1970).

[78] S. Ogawa and S. Ino, Journal of Crystal Growth **13**, 48 (1972).

[79] K. Kimoto and I. Nishida, Journal of the Physical Society of Japan **22**, 940 (1967).

[80] V. N. Robinson and J. L. Robins, Thin Solid Films **20**, 155 (1974).

[81] E. M. Chan, M. J. Buckingham, and J. L. Robins, Surface Science **67**, 285 (1977).

[82] A. Puskeppel and M. Harsdorff, Thin Solid Films **35**, 99 (1976).

[83] R. Conrad and M. Harsdorff, Thin Solid Films **192**, 163 (1990).

[84] W. D. Westwood, N. Waterhouse, and P. S. Wilcox, *Tantalum thin films* (Academic Press, London ; New York, 1975).

[85] J. A. Mejias, Physical Review B **53**, 10281 (1996).

[86] J. D. Lee, *Concise inorganic chemistry* (Chapman & Hall, London ; New York, 1996).

[87] I. Barin, *Thermochemical data of pure substances* (VCH, Weinheim, Federal Republic of Germany ; New York, 1993).

[88] B. F. Usher and J. L. Robins, Thin Solid Films **149**, 351 (1987).

[89] C. Schalansky and Z. A. Munir, Journal of Crystal Growth **97**, 310 (1989).

[90] A. Javey, J. Guo, Q. Wang, M. Lundstrom, and H. J. Dai, Nature **424**, 654 (2003).

[91] C. R. Henry, Surface Science Reports **31**, 235 (1998).

[92] C. D. Dimitrakopoulos and P. R. L. Malenfant, Advanced Materials **14**, 99 (2002).

[93] G. Horowitz, Advanced Materials **10**, 365 (1998).

[94] G. Witte and C. Woll, Journal of Materials Research **19**, 1889 (2004).

[95] N. Karl, Synthetic Metals **133**, 649 (2003).

[96] T. W. Kelley and C. D. Frisbie, Journal of Physical Chemistry B **105**, 4538 (2001).

[97] D. E. Hooks, T. Fritz, and M. D. Ward, Advanced Materials **13**, 227 (2001).

[98] T. Sakurai, X. D. Wang, Q. K. Xue, Y. Hasegawa, T. Hashizume, and H. Shinohara, Progress in Surface Science **51**, 263 (1996).

[99] T. Ogawa, K. Kuwamoto, S. Isoda, T. Kobayashi, and N. Karl, Acta Crystallographica Section B-Structural Science **55**, 123 (1999).

[100] M. Stohr, M. Gabriel, and R. Moller, Surface Science **507**, 330 (2002).

[101] I. Chizhov, A. Kahn, and G. Scoles, Journal of Crystal Growth **208**, 449 (2000).

[102] F. Rosei, M. Schunack, Y. Naitoh, P. Jiang, A. Gourdon, E. Laegsgaard, et al., Progress in Surface Science **71**, 95 (2003).

[103] M. Grobis, X. Lu, and M. F. Crommie, Physical Review B **66**, 161408 (2002).

[104] W. W. Pai, C. L. Hsu, M. C. Lin, K. C. Lin, and T. B. Tang, Physical Review B **69**, 125405 (2004).

[105] E. I. Altman and R. J. Colton, Surface Science **295**, 13 (1993).

[106] R. D. Johnson, C. S. Yannoni, H. C. Dorn, J. R. Salem, and D. S. Bethune, Science **255**, 1235 (1992).

[107] M. S. Dresselhaus, G. Dresselhaus, and P. C. Eklund, *Science of fullerenes and carbon nanotubes* (Academic Press, San Diego, 1996).

[108] D. Braun, A. Schirmeisen, and H. Fuchs, Surface Science **575**, 3 (2005).

[109] L. Kilian, E. Umbach, and M. Sokolowski, Surface Science **573**, 359 (2004).

[110] J. V. Barth, G. Costantini, and K. Kern, Nature **437**, 671 (2005).

[111] T. Kunstmann, A. Schlarb, M. Fendrich, T. Wagner, R. Moller, and R. Hoffmann, Physical Review B **71**, 121403 (2005).

[112] S. A. Burke, J. M. Mativetsky, R. Hoffmann, and P. Grutter, Physical Review Letters **94**, 096102 (2005).

[113] T. Fukuma, K. Kobayashi, K. Noda, K. Ishida, T. Horiuchi, H. Yamada, et al., Surface Science **516**, 103 (2002).

[114] L. Nony, R. Bennewitz, O. Pfeiffer, E. Gnecco, A. Baratoff, E. Meyer, et al., Nanotechnology **15**, S91 (2004).

[115] M. Mobus, N. Karl, and T. Kobayashi, Journal of Crystal Growth **116**, 495 (1992).

[116] S. Sadewasser and M. C. Lux-Steiner, Physical Review Letters **91**, 266101 (2003).

[117] D. B. Sirdeshmukh, L. Sirdeshmukh, and K. G. Subhadra, *Alkali halides : a handbook of physical properties* (Springer, Berlin ; New York, 2001).

[118] D. Schlettwein, A. Back, B. Schilling, T. Fritz, and N. R. Armstrong, Chemistry of Materials **10**, 601 (1998).

[119] G. Binnig, H. Fuchs, and E. Stoll, Surface Science **169**, L295 (1986).

[120] M. Bohringer, W. D. Schneider, R. Berndt, K. Glockler, M. Sokolowski, and E. Umbach, Physical Review B **57**, 4081 (1998).

[121] V. P. Zhdanov, Surface Science Reports **12**, 183 (1991).

[122] S. Berner, M. Brunner, L. Ramoino, H. Suzuki, H. J. Guntherodt, and T. A. Jung, Chemical Physics Letters **348**, 175 (2001).

[123] A. S. Foster, C. Barth, A. L. Shluger, and M. Reichling, Physical Review Letters **86**, 2373 (2001).

[124] J. E. Sader and S. P. Jarvis, Applied Physics Letters **84**, 1801 (2004).

[125] W. I. F. David and R. M. Ibberson, Journal of Physics-Condensed Matter **5**, 7923 (1993).

[126] R. Moret, Acta Crystallographica Section A **61**, 62 (2005).

[127] F. Gugenberger, R. Heid, C. Meingast, P. Adelmann, M. Braun, H. Wuhl, et al., Physical Review Letters **69**, 3774 (1992).

[128] W. I. F. David, R. M. Ibberson, and T. Matsuo, Proceedings of the Royal Society of London Series a-Mathematical Physical and Engineering Sciences **442**, 129 (1993).

[129] B. Sundqvist, Physica B **265**, 208 (1999).

[130] E. W. Weisstein, (MathWorld - A Wolfram Web Resource, http://mathworld.wolfram.com/TruncatedIcosahedron.html, 2006).

[131] Z. Y. Rong and L. Rokhinson, Physical Review B **49**, 7749 (1994).

[132] Y. Chen, G. Y. Jung, D. A. A. Ohlberg, X. M. Li, D. R. Stewart, J. O. Jeppesen, et al., Nanotechnology **14**, 462 (2003).

[133] C. P. Collier, G. Mattersteig, E. W. Wong, Y. Luo, K. Beverly, J. Sampaio, et al., Science **289**, 1172 (2000).

[134] L. L. Wang and H. P. Cheng, Physical Review B **69**, 165417 (2004).

[135] K. W. Hipps, Science **294**, 536 (2001).

[136] M. E. Pumarol, Y. Miyahara, R. Gagnon, and P. Grutter, Nanotechnology **16**, 1083 (2005).